A Multi-Scale Framework for Nanocomposites including Interphase and Agglomeration Effects

Von der Fakultät für Bauingenieurwesen und Geodäsie der Gottfried Wilhelm Leibniz Universität Hannover zur Erlangung des Grades

Doktor der Ingenieurwissenschaften

(Dr.-Ing.)

genehmigte Dissertation von

Dipl.-Ing. Johannes Andreas Fankhänel

2020

Referent:

Prof. Dr.-Ing. habil. Raimund Rolfes,

Gottfried Wilhelm Leibniz Universität Hannover, Deutschland

Korreferent:

Prof. Dr. Silvestre Pinho

Imperial College London, Großbritannien

Tag der Promotion: 14.07.2020

Abstract

Nano-scaled matrix additives, such as nanoparticles and nanotubes, can considerably improve the mechanical properties of polymers. However, the exact mechanisms leading to the increased properties have not been completely understood. Two effects, which play a minor role in the prediction of the elastic properties of nanocomposites so far, are the formation of a particle-matrix interphase and agglomeration of nanoparticles. Based on the literature, both can be assumed to considerably affect the molecular structure and the mechanical properties and should thus be included in the material design process.

In this thesis, a hierarchical multi-scale framework for the prediction of the elastic nanocomposite properties is developed. It incorporates the previously mentioned effects and contributes to a more realistic numerical modeling and simulation of nanocomposites. Starting on the atomistic level, the elastic properties of the constituents of the nanocomposite, namely the nanoparticle, the bulk polymer and the nanoparticle-polymer interphase, are characterized. Besides classical virtual material tests, two new simulation approaches are developed. Simulating atomic force microscopy allows for a direct comparison to nano-scaled experiments and can thus contribute to a better understanding of the acting principles. To overcome associated restrictions, a new approach for the direct calculation of the mechanical interphase properties based on molecular dynamics simulations is introduced.

The findings and the homogenized elastic properties from the atomistic scale are sequentially transferred to the microscale, on which models with three levels of detail are investigated. Representative volume elements containing a homogeneous primary particle distribution are used for calibrating the finite element simulations and for studying the influence of the interphase on the elastic nanocomposite properties. By introducing agglomerate unit cells and representative agglomerate volume elements, the influence of agglomeration and the agglomerate size distribution can be incorporated step by step. To additionally study the effect of resin-free areas inside the agglomerates, coupled simulations are developed, which combine the fundamental ideas of the finite and discrete element method.

The whole multi-scale framework is demonstrated for a boehmite/epoxy nanocomposite. Because of the small scale, a consistent and direct validation is not feasible with existing experimental methods and results. With the current assumptions, the elastic nanocomposite properties can be predicted with a lower bound, which provides a good approximation of the macroscopic experiments, and an upper bound, which shows the potential of the nanocomposite. Due to the modular implementation of the model generation, the framework can easily be enhanced by possible new findings.

Keywords: Nanocomposite, Molecular Dynamics, Interphase, Agglomeration, Elastic Properties

Kurzfassung

Nanoskalige Matrixadditive, wie Nanopartikel und Kohlenstoffnanoröhren, tragen zu einer erheblichen Verbesserung der mechanischen Eigenschaften von Polymeren bei. Die genauen Mechanismen, die zur Steigerung der Eigenschaften führen, sind dabei jedoch nicht vollständig erforscht. Zwei Phänomene, die in der Vorhersage der elastischen Eigenschaften von Nanokompositen bisher eine untergeordnete Rolle spielen, sind die Ausbildung einer Partikel-Matrix-Interphase und die Agglomeration von Nanopartikeln. Die Literatur zeigt, dass beide Effekte die molekulare Struktur und die mechanischen Eigenschaften beeinflussen können und daher bei der Entwicklung neuer Materialien berücksichtigt werden sollten.

In der vorliegenden Arbeit wird ein sequentieller Multiskalen-Ansatz zur Vorhersage der elastischen Eigenschaften von Nanokompositen entwickelt. Der Ansatz berücksichtigt die oben genannten Effekte und trägt somit zu einer realistischeren numerischen Abbildung von Nanokompositen bei. Auf der atomistischen Ebene werden zunächst die elastischen Materialeigenschaften der einzelnen Bestandteile des Nanokomposites (Nanopartikel, Polymer, Nanopartikel-Polymer-Interphase) bestimmt. Neben klassischen virtuellen Materialtests werden dafür zwei neuartige Simulationsansätze entwickelt. Die Simulation der Rasterkraftmikroskopie erlaubt einen direkten Vergleich zu nanoskaligen Experimenten und trägt somit zu einem besseren Verständnis der Wirkmechanismen bei. Um damit verbundene Restriktionen zu überwinden, wird ein neuartiger Ansatz zur direkten Berechnung der mechanischen Interphaseneigenschaften basierend auf Moleküldynamiksimulationen vorgestellt.

Die Erkenntnisse und die homogenisierten elastischen Eigenschaften der atomistischen Skala werden schließlich sequentiell auf die Mikroskala übertragen, auf der Modelle mit drei verschiedenen Detaillierungsgraden untersucht werden. Repräsentative Volumenelemente mit einer homogenen Primärpartikelverteilung dienen der Kalibrierung der Finite-Elemente-Simulationen und der Untersuchung des Einflusses der Interphase auf die elastischen Eigenschaften des Nanokomposites. In Form von Agglomerat-Einheitszellen und repräsentativen Agglomerat-Volumenelementen lässt sich schrittweise der Einfluss der Agglomeration und der Agglomeratgrößenverteilung hinzufügen. Um zusätzlich den Einfluss von harzfreien Zonen innerhalb der Agglomerate berücksichtigen zu können, wurden gekoppelte Simulationen entwickelt, die die grundsätzlichen Ideen der Finite Elemente Methode und der Diskrete Elemente Methode vereinen.

Der komplette Multiskalen-Ansatz wird anhand eines Böhmit/Epoxy-Nanokomposits veranschaulicht. Aufgrund der kleinen Skala ist eine durchgängige, direkte Validierung mit existierenden Methoden und Ergebnissen nicht möglich. Die getroffenen Annahmen ermöglichen die Vorhersage der elastischen Eigenschaften der Nanokomposite in Form einer unteren Grenze, die gleichzeitig eine gute Annäherung an die makroskopischen experimentellen Ergebnisse liefert, und einer oberen Grenze, die das Potential des Nanokomposits aufzeigt. Durch den modularen Aufbau kann die Modellgenerierung problemlos um eventuelle neue Erkenntnisse erweitert werden.

Schlagwörter: Nanokomposit, Moleküldynamik, Interphase, Agglomerat, Elastische Eigenschaften

Vorwort

Die vorliegende Arbeit entstand in den Jahren 2014 bis 2019 während meiner Tätigkeit als wissenschaftlicher Mitarbeiter am Institut für Statik und Dynamik (ISD) an der Leibniz Universität Hannover.

Mein besonderer Dank gilt meinem Doktorvater und Leiter des ISD, Professor Dr.-Ing. habil. Raimund Rolfes, für seine Motivation, wenn Motivation nötig war, für seine Nachsicht, wenn Nachsicht nötig war sowie für seine fachlichen Anregungen und die jederzeit gute Betreuung. Mein Dank gebührt weiterhin Prof. Dr. Silvestre Pinho, Direktor des Mechanics of composites lab am Imperial College London, für die Übernahme des Korreferats und seine wertvollen fachlichen Hinweise zur vorliegenden Arbeit.

Für ihre Hilfsbereitschaft, das angenehme Arbeitsklima und die tolle Gemeinschaft danke ich allen Kollegen des ISD. Besonderer Dank gilt Dr. Behrouz Arash, Dipl.-Ing. Dr. Benedikt Daum und Dr. ir. Eelco Jansen für die fachlichen Diskussionen, Robin Unger für seine Unterstützung, Aufmunterung und Toleranz, sowie Christian Claußen und Andreas Ehrmann für die gemeinsam verbrachte Zeit.

Während meiner Zeit am Institut für Statik und Dynamik erfuhr ich besonders intensiven fachlichen Austausch mit den Kollegen der Forschergruppe 2021 ("Wirkprinzipien nanoskaliger Matrixadditive für den Faserverbundleichtbau", Förderung durch die Deutsche Forschungsgemeinschaft). Ich möchte mich bei allen Kollegen für die angenehme und fruchtbare Zusammenarbeit bedanken, insbesondere bei Prof. Dr. Michael Sinapius für die hervorragende Leitung der Forschergruppe sowie bei Dr. Dorothee Silbernagl und Maximilian Jux für die intensive fachliche Zusammenarbeit.

Nicht zuletzt danke ich in besonderer Weise meinen Freunden, Eltern, Großeltern und meiner Schwester, die mich jederzeit nach Kräften unterstützt haben. Ohne ihren Rückhalt wäre diese Arbeit nie vollendet worden.

Hannover, Juli 2020

Johannes Fankhänel

Contents

List of Figures

List of Tables

List of Acronyms and of Symbols

Acronyms

ADFS	Amplitude dependent force spectroscopy
AFM	Atomic force microscopy
BAM	Bundesanstalt für Materialforschung und -prüfung
BC	Boundary condition
BNP	Boehmite nanoparticle
CMNC	Ceramic matrix nanocomposite
CNT	Carbon nano tube
DBC	Displacement boundary condition
DEM	Discrete element method
DLR	German Aerospace Center
FDC	Force displacement curve
FEM	Finite element method
FRP	Fiber reinforced plastic
HW	Hot wet condition
ImAFM	Intermodulation atomic force microscopy
MD	Molecular dynamics
MDFEM	Molecular dynamic finite element method
MMNC	Metal matrix nanocomposite

NC	Nanocomposite
NP	Nanoparticle
P	Polymer
PBC	Periodic boundary condition
PMNC	Polymer matrix nanocomposite
RFA	Resin free area
RT	Room temperature
RVE	Representative volume element
UC	Unit cell
VE	Volume element
XRD	X-ray diffraction

Symbols

$\boldsymbol{\alpha}$	Normalized direction vector of the image cell
$\boldsymbol{\epsilon}$	Strain tensor
$\boldsymbol{\sigma}$	Stress tensor
$\boldsymbol{f}^n$	Interatomic force vector of atom n
$\boldsymbol{f}^{nm}$	Interatomic force vector acting between atom n and atom m
$\boldsymbol{h}$	Matrix of the VE box vectors
$\boldsymbol{L}$	Vector of the VE sizes
$\boldsymbol{r}^n$	Position vector of atom n
$\boldsymbol{r}^{nm}$	Vector pointing from atom n to atom m
$\boldsymbol{X}, \boldsymbol{Y}$	Auxiliary varibales for the calculation of the atomic strain
δ_{ij}	Kronecker delta

λ, μ	Lamé constants
$\mathbb{C}$	Stiffness tensor
Σ	Macroscopic uniaxial traction
a, b, c	VE or RVE dimensions
D	Sample deformation
d	displacement, distance
d_{eq}	equilibrium distance
d_{pp}, d_{agg}	primary particle diameter, agglomerate diameter
F	Indentation force
l	Characteristic size of any structural feature in the VE
m	Mass
n_{pp}	number of primary particles per agglomerate
R	AFM tip radius
R_c	Cutoff for the nonbonding interactions
r_{inter}	Interaction radius for the calculation of the atomic strain
U	Potential energy, Macroscopic uniaxial displacement
V	Volume
F_{ij}	jth component of the reaction force vector on the boundary normal to i
u_{ij}	jth component of the displacement vector on the boundary normal to i
u_{xy}	y component of the displacement vector on the boundary normal to x

Indices

agg	Agglomerate

i, j, k, l	Tensor components
l, h	low, high
$long$	longitudinal, in loading direction
n, m	Atom indices
pp	Primary particle
R	Subsection index
ref, def	reference and deformed configuration
tip	AFM tip
tot	total, effective
tr	transverse, perpendicular to the loading direction
x, y, z	Spacial directions

Other

$\langle\cdot\rangle$	Volume average

1 Introduction

1.1 Motivation and Aim

Aerospace, automotive or energy industry - the development of new technical products is dominated by contrary desires for more performance, power or functionality on the one hand and ecological and economic restrictions on the other hand. To meet these demands, one of the main challenges in today's engineering is weight reduction. Besides structural optimization, research is focused on the development of new materials with increased mechanical properties at low weight.

One of these comparatively new classes of materials are fiber-reinforced composites. They combine the outstanding mechanical properties of the reinforcement material (e.g. glass fiber or carbon fiber) with the good processability and low density of mostly polymer matrices. Additionally, these so-called fiber-reinforced plastics (FRPs) offer manifold possibilities for tailoring the material for specific applications. These positive attributes lead to a widely spread use of FRPs in technical applications, which can nowadays be found in highly complex structures in aerospace industries as well as in many areas of our daily lives.

However, in specific cases, the potential of FRPs is limited by the performance of the matrix material. For instance, the load-bearing capacity of FRPs under compression load strongly depends on the support of the fibers given by the surrounding matrix material, which is strongly related to the Young's modulus and the strength of the polymer. Other examples of the so-called matrix dominated properties are the shear modulus, the fracture toughness or the interlaminar shear strength.

One possibility to further improve the matrix dominated properties of FRPs is the application of nano-scaled matrix additives, such as nanoparticles (NPs) or carbon nanotubes (CNTs). Both have been shown to be able to improve a broad range of material properties of polymer materials and FRPs [1–6]. To demonstrate that, selected results of the investigation of boehmite nanoparticle (BNP) and carbon fiber reinforced epoxy, which provided the starting point for the DFG research unit FOR2021, and thus for this thesis, are depicted in Fig. 1.1 [1]. The diagram shows, that BNPs can improve the selected matrix dominated properties by 10 to 25%. According to [1], aluminum oxide based reinforcement materials are promising to increase not only mechanical properties but also thermal properties and processability. The ultimate choice of BNPs is based on the good commercial availability

and the diverse possibilities for surface modification[1] due to the surface hydroxyl groups. In the specific case shown, the BNPs were surface modified with taurine molecules.

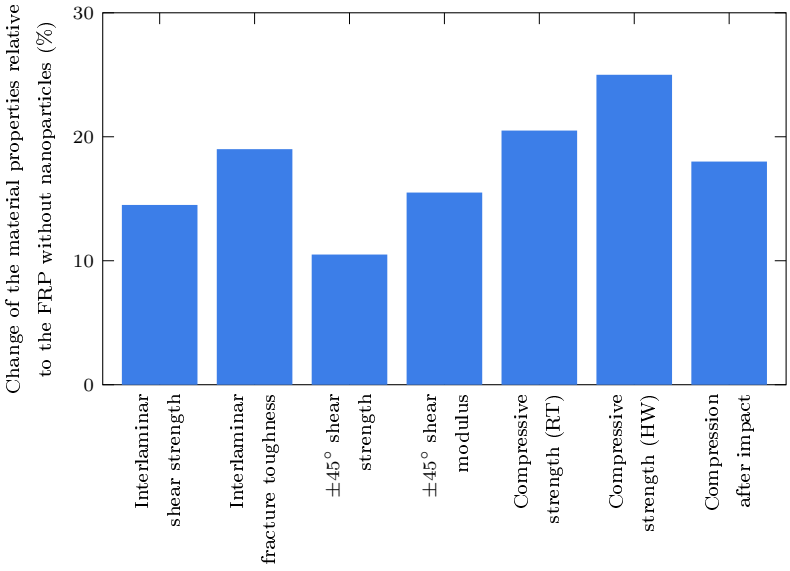

Figure 1.1: Matrix dominated material properties of a carbon fiber composite with a weight fraction of 15% taurine modified boehmite relating to the reference properties without particles [1] (RT: room temperature, HW: hot wet condition).

Shahid et al. [2] similarly investigated BNPs embedded in an epoxy matrix, but modified the particles with lysine and parahydroxybenzoate. They reported mostly inferior matrix dominated properties compared to the unfilled matrix, especially for high weight fractions. This comparison leads to the conclusion that the NP modification plays an important role in the development of high-performance nanocomposites (NCs). The surface modification alters the chemical interaction between filler and matrix, and thus very probably also the morphology of the polymer itself in the vicinity of the fillers, introducing a so-called interphase region.

Another aspect of NCs, that has not drawn much attention to itself in the literature,

[1] To ease the processing of the NPs or increase the chemical affinity between the NPs and the polymer, often organic molecules are applied to the NP surface. This process is referred to as surface modification.

especially the numerically focused literature, is agglomeration. Depending on the chemical composition, NPs typically show a tendency to form agglomerates, which can easily be 100 times larger than the primary particles. Agglomeration is usually reduced and controlled during manufacturing, but is often not completely avoidable. The size and the inner structure of the agglomerates, however, can play a key role in the mechanical behavior of the NCs. In particular, one question seems to stand out: Are the agglomerates filled with polymer or not? In case yes, the polymer inside of the agglomerates can have a significantly different network morphology than bulk polymer or even the interphase of a primary particle. In case no, the inward surface of the primary particles forming the agglomerate is detached from the polymer and the primary particles interact through physical bonds only. It is imaginable that this case results in lower elastic properties compared to agglomerates, which are stabilized by covalently bonded polymer on the inside.

Generally, the exact mechanisms leading to a change of the NCs properties compared to the unfilled material are often still unknown. To enable a purposeful virtual development of NCs, the effects related to the presence of interphases and agglomerates need to be understood and incorporated into the material design process. This thesis proposes a hierarchical multi-scale framework, bridging the atomistic level, on which the material is modeled as a discrete system of atomic resolution, to the microscale, on which the effective properties of the NP reinforced polymer are calculated. The main focus lies on an adequate incorporation of interphase and agglomeration related effects on the inner structure and eventually on the mechanical properties of the NC. Besides the framework itself, the key feature of the thesis is the extraction of the elastic material properties of each constituent of the NCs, especially the interphase properties, on the atomistic scale. To do so, new simulations that mimic the testing conditions of the atomic force microscopy (AFM) are presented and a new approach for extracting local mechanical properties from molecular dynamics (MD) simulations is developed. Throughout this thesis, the whole framework is presented and discussed by reference to BNP/epoxy NCs with varying interfacial interactions.

1.2 Outline

This thesis is divided into seven chapters.

Following this section, the remaining chapter gives a detailed review of the state of the art with a strong focus on numerical studies. Besides presenting a general introduction into the field of NCs, the literature is discussed along with the four main topics of the thesis, which are the BNPs, the epoxy, the BNP/epoxy interphase and the agglomeration of NPs.

Chapter 2 is dedicated to the topic of multi-scale analysis. The concept of the developed multi-scale framework is presented and the fundamentals of the homogenization both from the atomistic to the microscale and from the microscale to the macroscale are introduced. This includes the discussion of certain prerequisites of the simulation models, like the choice of the boundary conditions or a possible mesh size dependency, and the introduction of the mathematical framework for the calculation of the effective elastic properties. Furthermore, as one of the major contributions of this thesis, a new method for the calculation of local elastic properties from MD simulations is introduced.

In chapters 3 to 5, the model generation and the simulations on the atomistic scale are presented. In addition, the effective elastic properties of each constituent of the NC are reported. Chapter 3 describes the investigation of the mechanical behavior of the boehmite. Therefore, the new approach of simulating AFM is introduced. Furthermore, the determination of the interparticulate force-displacement curves is described, which are needed for the simulation of the unfilled agglomerates on the continuum level, presented in chapter 6. Chapter 4 deals with the determination of the elastic properties of the epoxy matrix. Two approaches for the generation of the cross-linked network structure of the polymer are introduced and a parametric study of different effects, such as the strain rate or the choice of selected force field parameters on the elastic properties is conducted. In chapter 5, the extraction of the elastic interphase properties is shown. Two different approaches, an AFM simulation-based one and the previously mentioned new approach for the direct calculation of local elastic properties from MD simulations, are presented and compared.

Chapter 6 is dedicated to the simulations and the homogenization on the microscale. The findings from the previous chapters are assembled to finite element method (FEM) based NC models. In particular, a new modeling approach for the simulation of the unfilled agglomerates is introduced, which can be understood as a coupling of the FEM and the discrete element method (DEM). Furthermore, the influence of different factors, like the choice of the boundary conditions or a possible mesh size dependency, is discussed and, ultimately, the effective elastic properties of representative volume elements (RVEs) containing homogeneously distributed primary particles or agglomerated BNPs are reported.

Chapter 7 concludes this thesis by summarizing the major findings and conclusions. Additionally, open questions are identified to stimulate further research in these areas.

1.3 State of the Art and Scientific Contribution

In this section, an introduction into the general topic of NCs is provided and the constituents and peculiarities of this class of materials are discussed. In particular,

a review of existing and mostly simulation-based approaches for the characterization of NCs and the underlying constituents and effects is presented. Most of the subsections refer to a specific chapter of this thesis, and can thus be regarded as the state of the art for the work presented there. Existing experimental results from the FOR2021 research unit are in large parts excluded from this section, but, whenever helpful, explained and compared to the numerical results of this thesis in the respective chapter.

1.3.1 Introduction to Nanocomposites

NCs are a comparatively new class of materials, which started to attract increasing scientific attention in the 90s of the last century. Like every type of composite material, this subclass is a multiphase solid material with at least one of its constituents having a spatial extent in the nanometer (i.e. 10^{-9} m) range [7]. There is no absolute definition, but an upper limit, which one may come across in the literature, is a size of 100 nm.

NCs are typically classified according to their matrix material. The three common types are ceramic matrix NCs (CMNC), metal matrix NCs (MMNC) and polymer matrix NCs (PMNC). Not only because they are relevant for the present thesis, PMNCs are focused here and CMNCs and MMNCs will not be further discussed. Polymer materials can nowadays be found in many industrial branches, as they are lightweight, easy to process and commonly cheap. Another advantage of polymers is that they can easily be modified, e.g. by adding nano-scaled fillers, while maintaining their low density and mostly ductile material behavior. As a downside, some of the properties of the pure polymers, especially mechanical properties, such as the Young's modulus or tensile strength, are poor compared to metals or ceramics. These weaknesses have already been partly addressed by the development of FRPs, that typically possess significantly higher specific tensile moduli or strengths than metals or ceramics. Still, some of the FRPs' mechanical properties, which are commonly summarized under the term matrix dominated properties, are considerably worse. Examples are the behavior under in-plane compression load or the impact resistance. Nano-scaled fillers can help to overcome these weaknesses and further improve the FRPs properties.

A large number of both experimental and numerical studies on different properties of NCs has been conducted, for instance on the mechanical properties [4–6, 8–10], the electrical properties [11, 12] or the thermal properties [13–15]. Here, we focus on the mechanical properties and especially on how they are influenced by the interfacial filler-matrix interactions. It is often shown that the incorporation of NPs can lead to the increase of a variety of mechanical properties of FRPs, such as the compressive strength, the fracture toughness or the impact resistance. For instance, in [1] it was shown that a boehmite weight fraction of 15% leads to an increase of

the named properties up to 25% for a carbon fiber/epoxy composite. Other studies substantiate these results. Uddin and Sun [16] investigated silica particle reinforced glass/epoxy composites and found a significant increase in compressive strength and transverse tensile strength. Subramaniyan and Sun [17] obtained similar results for nanoclay/glass/epoxy composites.

The exact cause of the improved mechanical properties is thereby often unknown. Similar to other composite materials, the goal of NCs is to combine at least two phases of different matter to obtain a material with superior properties. The main difference compared to composites with additives of larger size, such as FRPs, is the exceptionally high specific surface area, as shown in Fig. 1.2. Hence, it can be hypothesized that the improved NC properties are related to the interfacial interactions between the nano-scaled fillers and the polymer. This is substantiated by the comparison of studies with the same NPs and polymer, but different surface modifications, such as [1] and [2]. In both cases, the particle surface is loaded with different molecules to modify the interaction between particle and polymer. An increase of 10 to 25% of the tensile, compressive and shear properties as well as the impact resistance of taurine modified boehmite/epoxy NCs was reported in [1]. In contrast, Shahid et al. [2] found inferior tensile and flexural properties compared to the unfilled matrix for lysine and parahydroxybenzoate modifications, especially for high filler contents. This comparison illustrates that the surface modification plays an important role in the development of high-performance NCs. The changed chemical composition of the NP surface alters the chemical interaction between the filler and the polymer, and thus very probably not only the interfacial bonding but also the polymer network structure in the vicinity of the particles. The characterization of the network structure of the NP-polymer interphase is discussed in more detail in section 1.3.4.

Another important phenomenon in NCs is the agglomeration of the nano-scaled fillers before or during the processing of NCs. This effect has also been widely studied experimentally. For instance, many studies deal with the assessment of the dispersion quality, e.g. [18, 19]. Other studies discuss the effect of the dispersion quality on processability parameters, such as the viscosity, or on catalytic effects in polymers (see e.g. [20]). However, the influence of the dispersion quality and the resulting agglomerate size distribution on the mechanical properties has not been satisfactorily discussed in the literature so far. A small number of articles tried to address this issue, e.g. [21, 22], but share one major flaw. In these studies, the agglomerate size distributions are dependent on the weight fraction of the filler, and thus the measured mechanical properties are dependent on two parameters, the agglomerate size distribution and the weight fraction. The dependence of the mechanical properties on the agglomerate size for a constant weight fraction was not investigated in the named studies. Another article was written by West and Malhotra [23], who varied the dispersion quality by processing the probe with different ultrasonic treatments and reported a significant influence on the mechanical

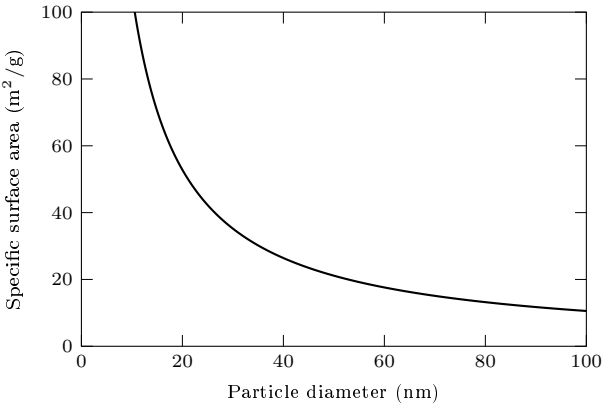

Figure 1.2: Specific surface area per unit mass of a spherical NP in dependence on the NP diameter.

properties. However, as stated in the same article, the ultrasonic treatment also shows a considerable influence on the network morphology of the neat polymer. Thus, this study, again, discusses two overlaid effects. Within the scope of the FOR2021 project, an attempt to fill this gap was made by investigating BNP/epoxy NCs with different agglomerate size distributions and a constant weight fraction of 10%. More details about these measurements are discussed and compared in section 6.1. Similarly, the literature about the numerical determination of the influence of the agglomerate size on the mechanical properties of NCs is rather sparse. Most of the studies, like [24, 25], collectively report a positive influence of the dispersion quality on the mechanical properties. More detailed information on these studies is presented in section 1.3.5.

Under this light, the previously explained comparison between the results of the taurine modified boehmite/epoxy NC from [1] and the lysine and parahydroxybenzoate modified case from [2] can be interpreted differently. Among others, Gao et al. [26] showed that surface modification can help to obtain a better dispersion quality by producing more stable NP solutions and preventing re-agglomeration effects. Though it cannot be reconstructed in detail, it is imaginable that the taurine modification from [1] led to a finer agglomerate size distribution than the two modifications investigated in [2]. Thus, the deteriorated properties reported by Shahid et al. [2] could also be the result of a lower dispersion quality.

Concluding from the previous paragraphs, the effects related to both the interphase and agglomeration can be regarded to have a major impact on the mechanical properties of NCs. A more detailed discussion of both effects with the focus on the

numerical characterization can be found in the following in sections 1.3.4 and 1.3.5. This section was intended to provide an introduction into the topic of PMNC to motivate a thorough numerical investigation of the interphase and agglomeration related effects. For a recommendable and much more comprehensive review of the general field of NCs, than it is possible in this thesis, the reader is referred to the article of Camargo et al. [7].

1.3.2 Boehmite

The material for the nano-scaled reinforcement phase used throughout this thesis is boehmite. Boehmite is a mineral named after the Czech-German chemist Johann Böhm (1895 - 1952), who first studied the species employing X-ray diffraction (XRD) measurements [27]. Since then, its structural properties have been widely studied, e.g. experimentally through XRD by Bokhimi et al. [28] or by means of Raman spectroscopy by Kiss et al. [29] and numerically through quantum mechanics by Tunega et al. [30] and Noel et al. [31]. Boehmite is classified as an oxyhydroxide (γ-AlO(OH)) with a base-centered orthorhombic unit cell with the lattice parameters a = 3.693 Å, b = 12.221 Å and c = 2.865 Å. Its crystalline structure consists of double layers of oxygen octahedrons bonded to central aluminum atoms. The hydroxyl groups of each layer are bonded via hydrogen bonds to the hydroxyl groups of the obverse layer.

As boehmite is a component of bauxite, its main focus in technical applications is the production of aluminum. Only recently, boehmite was discovered as a particulate filler material for NCs [32]. Thus, and also because boehmite is rarely well crystallized and stable at the macroscale [33], the mechanical properties of monocrystalline boehmite can hardly be found in the literature. From nanoindentation experiments, a Young's modulus of 120 GPa was reported for boehmite using a sample of APYRAL AOH20 (Nabaltec AG) [34]. However, this study has two major weak points. Firstly, though of quite similar structure, APYRAL AOH20 is not boehmite, but gibbsite ($Al(OH)_3$) [35] and secondly, the used samples were not mono-crystalline. Generally speaking, the applicability of nanoindentation for the determination of the mechanical properties of boehmite is questionable. The thickness of the used boehmite sample should be at least in the higher µm range since the maximum indentation depth in nanoindentation should not exceed 10% of the sample height to obtain undisturbed results [33]. To the knowledge of the author, mono-crystalline boehmite does not exist in this order of magnitude.

Tunega et al. [30] studied the elastic properties of boehmite from a numerical point of view, using the density-functional theory and the density-functional based tight-binding method. They reported bulk moduli of 93 GPa and 82 GPa, respectively. Assuming, for simplicity, isotropic behavior and a Poisson's ratio of 0.22, the Young's modulus can be estimated to fall within a range of 138 to 156 GPa.

To provide further insight into the mechanical behavior of boehmite, within the scope of the FOR2021 project experimental studies on the mechanical properties of boehmite were conducted by the Bundesanstalt für Materialforschung und -prüfung (BAM). The results from AFM measurements on commercially available spray-dried boehmite NPs (Disperal HP14, Sasol) [36] embedded in an epoxy matrix (for further details see section 3.1) indicated a conspicuously lower stiffness than expected from the literature. Thus, a comprehensive experimental and numerical study on the mechanical behavior of boehmite was conducted as a collaboration of the ISD and the author of the thesis on the one hand and the BAM on the other hand, as published in [33]. In section 3.1, the respective results of the numerical investigations are presented and discussed.

Besides the material behavior and the mechanical properties of boehmite, the interaction between the NPs is needed for the multi-scale framework presented in this thesis. In DEM simulations, that deal for instance with the formation of agglomerates (see e.g. [37]), the interparticulate forces are modeled using the so-called Hamaker function [38]

$$F_H = -\frac{A}{6r^2}\frac{R_1 R_2}{R_1 + R_2}, \tag{1.1}$$

which describes the interaction forces F_H depending on the radii R_1 and R_2 and the distance r between the two interacting particles. In the above equation, A is the Hamaker constant, which depends on the contacting materials. This constant has been calibrated for many materials, but it can also be determined experimentally, e.g. by performing AFM-like experiments as shown in [39], or numerically, as e.g. shown by Hongo and Maezono [40]. In the scope of this thesis, the Hamaker function itself is not used, but the idea for the numerical determination of the interparticulate forces is adopted. Therefore, a statistically representative number of randomly generated and orientated particle-particle models is subjected to tensile, compression and shear load, while the interaction forces are recorded. More detailed information on this approach is presented in section 3.3.

1.3.3 Epoxy

Polymers, and specifically epoxy, are a widespread and well-known material, which is why only the modeling and characterization using MD approaches will be discussed in this section. Besides that, a summary of the experimental results of the specific epoxy used in the FOR2021 project is given in section 4.2.

The foundation for the numerical prediction of the material behavior of polymers using MD simulations is the generation of realistic and well-equilibrated models of the polymer network structure. Most of the proposed approaches rely on geometric considerations, where bonds are formed whenever the distance between two reactive sites becomes smaller than a specified reaction cutoff. Examples of this approach,

that has become the standard method for generating cross-linked polymer models, can be found in [41–43]. Most of the developments in this field are extensions of this general approach. For instance, Lin and Khare [44] proposed a framework in which pairs of reactive sites are identified, that minimize the sum of the bond lengths of all created bonds. Other developments can e.g. be found in the area of charge updating during the cross-linking simulations (see e.g. [45]). In this thesis, no advances in this field are made, but the general geometric approach explained above is used, as described in detail in section 4.3.

Because of the limited resolution of experimental methods, a direct validation of the chemical structures generated with the above approaches remains challenging and an indirect validation is still inevitable. Progress in this field was e.g. made by Hädicke and Stutz [46] and Cheng and Chiu [47] with the estimation of the gel point and by Rigby and Roe [48] and Mansfield and Theodorou [49] with the calculation of the glass transition temperature from MD simulations. As both of the named properties highly depend on the chemical composition of the system, they can be considered to be an indicator of the quality of the generated network structure.

Most relevant for this thesis is the mechanical characterization of epoxy using MD simulations, especially regarding the elastic properties. In the literature, two general approaches exist [50], which mainly differ in how the load is applied. Firstly, the elastic properties can be calculated from a constant strain or stress state. In this case, a small strain or stress is applied to the model followed by an energy minimization. The elastic properties can then be calculated in two ways. As proposed by Theodorou and Suter [51], the stiffness constants are obtained by calculating the second derivative of the potential energy with respect to the strain. Alternatively, the stress or strain fluctuations can be used to determine the elastic constants employing statistical mechanics, as proposed by Parrinello and Rahman [52]. The major disadvantage of this general approach is the long simulation time, that is typically needed to obtain the equilibrated system after loading. In the second general approach, a time-dependent strain or stress is applied similar to real experimental testing, as e.g. shown by Brown and Clarke [53]. An advantage of this approach is that the complete stress-strain relation can be simulated, and thus other properties, like the yield stress, can be obtained. Additionally, strain-rate dependent effects can be investigated with this method. Mainly because it promises more efficient simulations, the latter approach is adopted in this thesis.

Numerous numerical studies have been published about the elastic constants of polymers and the influence of many parameters, such as the degree of curing, temperature, strain rate, etc. It has for instance been found that the elastic properties strongly depend on the degree of curing of the polymer, as e.g. shown by Li and Strachan [54]. In particular, Shenogina et al. [55] reported that this influence is more pronounced for polymer systems comprising short monomers or curing agents. Other studies report an influence of the force field or selected force field parameters

on the elastic properties of polymers [56]. Especially, the choice of the nonbonding potential can play an important role, as Li and Strachan [45] observed that the use of the Buckingham potential instead of the Lennard-Jones potential can lead to a better prediction of the polymer properties with respect to experimental data. Despite the large differences of the strain rates used in the experiments (typically $\approx 10^{-4}1/s$) and the simulations (typically in the range of 10^8 to $10^{10}1/s$), most of the available numerical studies in the literature show a good agreement with experimental values or report that there is no influence of the strain rate on the elastic properties. Examples can be found in [54, 57]. However, other studies, like [58], observe an influence of the strain rate, in this case on the shear modulus. Yet other numerical studies report significantly higher Young's moduli than experimental measurements (see e.g. [59]), which could indicate a strain rate dependency. From this short overview, it can be concluded that many factors can influence the prediction of the elastic properties using MD. In the available literature, it is not always clear how the results were obtained and how the named effects were considered. A more detailed interpretation and the authors' view on the state of the art under the light of the parametric studies performed in this thesis are presented in the concluding section of chapter 4.

The literature situation concerning the numerical modeling and characterization of polymers is quite extensive. In this thesis, the mechanical characterization of the pure polymer is rather an application of existing approaches than the development of new methods, which is why only the fundamentals were presented in this section. A much more comprehensive overview can be found in [50].

1.3.4 Nanoparticle-Polymer Interphase

For the characterization of most materials or material constituents, well established experimental approaches exist. However, similar to the characterization of boehmite, the small size of the involved phases in NCs adds considerable difficulties and limits the possibilities of experimental testing. Thus, many studies in the literature focus on indirect methods for the characterization of the elastic interphase properties. The elastic properties of the filler, the matrix and the NC are typically known from macroscopic mechanical tests. Combining these results with analytical models, such as the Hashin-Shtrikman model [60] or the Mori-Tanaka model [61, 62], the effective interphase properties can be calculated, as e.g. shown in [63–66]. Similarly, instead of analytical models, FE models can be used, as e.g. presented by Bondioli et al. [67] and Qiao and Brinson [68]. Such indirect approaches have several downsides. Since analytical models completely ignore the underlying effects that lead to the existence of the interphase, they are often inaccurate. For instance, as the network morphology of the polymer in the vicinity of the NPs is unknown, the thickness of the interphase region is unknown as well. Thus, assumptions for the thickness

are made in the inverse calculation, resulting in elastic properties that are strongly dependent on this assumption. As another disadvantage, only effective interphase properties are available but no stiffness gradients throughout the interphase.

Recent developments in the mechanical testing on the nano-scale aim at a direct experimental measurement of the mechanical properties of NP/polymer interphases, but so far a well-performing approach has not been reported [69]. A promising method is the intermodulation AFM (ImAFM) [70], which has a high enough resolution to be able to separate the interphase from the other phases. However, so far no mathematical framework to describe the dependence of the elastic properties on the cantilever amplitude and frequency has been derived. Classical force-displacement curves (FDCs) measured by AFM suffer from several restrictions. Typically, available AFM tips diameters are in the range of $d \approx 30$ nm. Since, in contrast to the imAFM, a real indentation is performed, the deformed volume is too large to separate the interphase and the other phases. Furthermore, close to a phase boundary, the measurement of mixed moduli of both phases is inevitable.

To overcome the difficulties with the experimental characterization of the elastic interphase properties, numerical approaches, such as MD, can be convenient. These approaches are well suited for capturing small time and size scales and allow much easier access to the molecular structure and its modification. In MD simulations, the interphase is not explicitly modeled, as in the case of FEM simulations. Instead, it is automatically comprised in the atomistic structure whenever two phases of different matter border on each other. More details about the interpretation of the interphase and its modeling in the context of PMNCs can be found in chapter 5. The most common approach are inverse algorithms, which compare the results of MD simulations to analytical or FE calculations, as schematically illustrated in Fig. 1.3. Firstly, virtual tensile tests are simulated in MD. These simulations do not require any information about the elastic properties of the components but only the atomistic structure, which automatically contains the NP/epoxy interphase. Then, FEM simulations with known Young's moduli of the bulk epoxy and NP (e.g. from tensile tests) and with varying interphase Young's moduli are preformed, until the MD and FEM results converge. Many examples can be found in the literature. For instance, Cho et al. [71] used effective interface FE models for the prediction of the mechanical properties of nanoparticulate composites. In this study, silica filled polyimide was investigated regarding its effective interphase properties without considering a covalent bonding between filler and matrix and with varying particle sizes. In a similar approach, Shin et al. [25] reported effective interphase properties for silicon carbide/polypropylene NCs including agglomeration effects. Many other studies showed similar approaches, e.g. [59, 72, 73]. A different procedure was proposed by Arash et al. [3]. In this study, the interphase properties of CNT/polymer composites were calculated as the second derivative of the interaction energies between CNT and polymer with respect to the applied strain. All the mentioned studies share two major drawbacks. Firstly, the filler phase and the polymer are mostly

assumed to be chemically unbonded. Though this may be a realistic assumption for unmodified CNTs, common NP surface modifications aim at establishing chemical connections between the filler and the polymer to improve the mechanical properties of the NC. By not considering or varying the interfacial bonding in the above studies, the influence of the chemical interaction on the elastic interphase properties remains unclear. Secondly, these approaches do not allow for the calculation of stiffness gradients throughout the interphase but only deliver effective interphase properties.

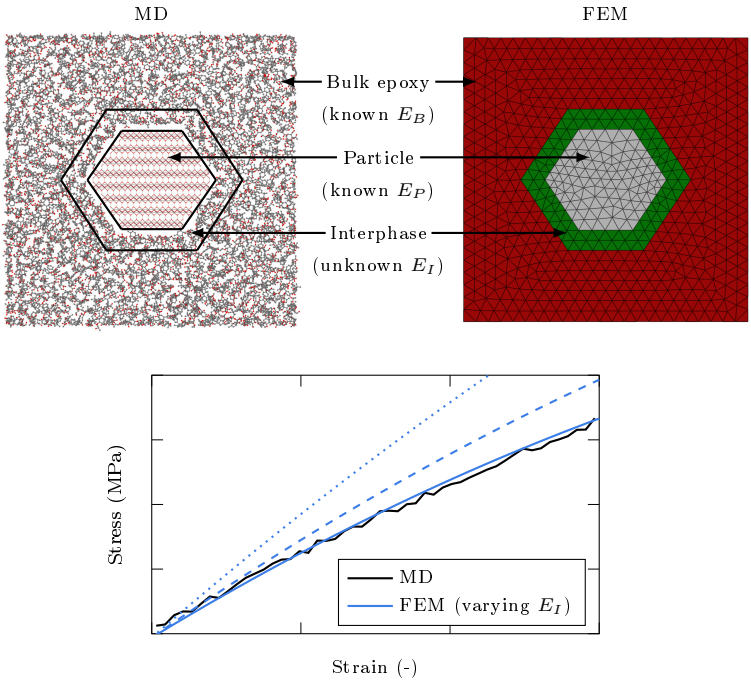

Figure 1.3: Schematic illustration of the concept of inverse algorithms for determining the effective interphase properties.

Other numerical studies focus on the interfacial bonding between filler and matrix. In a variety of articles, reactive MD simulations were performed to investigate the formation of polymer networks under the influence of another phase. For instance, Farah et al. [74] simulated the interphase formation of polystyrene in the presence of an artificial surface. Other studies, e.g. the article written by Arash et al. [5], investigated the influence of surface modifications, and hence varied interfacial bonding,

on the mechanical behavior of CNT/polymer composites. These studies report a considerable influence of the interfacial bonding on the mechanical properties of the NC. However, the interphase properties themselves are not investigated.

The existing literature still lacks a coherent numerical investigation of the connection between the interfacial bonding of the filler and polymer phases and the mechanical interphase properties. In this thesis, two different methodological frameworks for the characterization of the mechanical interphase properties from MD simulations are proposed. In the authors' early scientific work, AFM simulations were developed and conducted on the BNP/epoxy interphase for varying interfacial bonding, as presented in section 5.1. In contrast to real AFM, the AFM tip diameter can be significantly reduced, allowing for spatial separation of the interphase, boehmite and epoxy regions and the determination of the stiffness gradient in the interphase. This approach, however, shares the major drawback of measuring mixed moduli close to the phase boundaries. Thus, a different approach was developed. The fundamental idea of this approach is to divide the simulation models into subsections (e.g. slices of the simulation model, further details can be found section 2.2.1 and section 5.2), for which the stress and strain tensors are formulated based on the virial stress (see e.g. [75]) and the atomic strain proposed by Falk and Langer [76]. The stress and strain tensors can then be used for the homogenization of the mechanical properties of each subsection. Similar to the AFM simulations, the advantage of this approach over methods from the literature is that, depending on the choice of the subsections, the stiffness gradient throughout the interphase can be calculated in addition to the effective interphase properties. The approach is derived in section 2.2.1 and applied to the investigation of the interphase properties of BNP/epoxy NCs with varying interfacial bonding in section 5.2. To get rid of particle size-related effects, the idea of layered structures existing in the literature (see e.g. [77–79]) is adopted.

1.3.5 Agglomeration of Nanoparticles

As already stated in section 1.3.1, experimental studies in the field of agglomeration mostly deal with the determination of the dispersion quality or its influence on processing parameters, like the viscosity. An investigation of the correlation between the agglomerate size distribution and the mechanical properties or the impact of agglomeration on the polymer network formation cannot be found in the experimental literature. There are only a few numerical studies, that tried to fill this gap. Most of them focus on topics similar to the experimental literature, for instance the formation of agglomerates by means of MD [80] or Monte Carlo simulations [81, 82]. Numerical studies concerning the influence of agglomeration on the mechanical properties of the agglomerates or the NC are rare. The most common approach, that can be found in the literature, are micro-mechanical models, such as the model presented by Shi et al. [83]. In this article, the Mori-Tanaka model [61, 62] was

extended to account for spherical inclusions that represent clustered NPs or CNTs and the surrounding polymer. An application of this approach within a hierarchical multi-scale approach spanning from the nano to the macroscale is e.g. shown in [84]. Ultimately, the probability distribution of the macroscopic Young's modulus is reported and compared to experiments. Other articles, like [85, 86], present similar micro-mechanical approaches, but are by far not as comprehensive as the previous one. Though these studies show a good agreement with experimental results, from the authors' point of view the main weakness of these micro-mechanical approaches is that they ignore the underlying molecular structure. For instance, effects like the interfacial interaction between the filler and the polymer are neglected and a perfect bonding is assumed. Another important aspect, that is not considered, is the question whether the agglomerates are filled with polymer of not. The consequence of such effects is only expressed through parameters, with which the model can be calibrated.

One of the key mechanisms in agglomerates is the overlap of the interphases or, in other words, the reduction of the overall interphase volume caused by the closely located primary particles. Shin et al. [25] addressed this issue by simulating two NPs with varying distance embedded in a polymer matrix employing MD. The outcome of this study is the homogenized NC Young's modulus in dependence on the interparticulate gap. It was shown that the Young's modulus decreases with decreasing distance between the NPs. Though this study can generally be regarded as a valuable contribution, it has some considerable flaws. The major disadvantage is that the interfacial bonding between the fillers and the polymer and the expected alteration of the network structure have not been systematically studied. In fact, the interfacial bonding and the characteristics of the cross-linked polymer have not been mentioned at all. Another drawback is the expected dependence of the results on the particle size. The study ultimately transfers the findings from the MD simulations to an FE model, but it remains unclear how larger agglomerates can be simulated.

A first real approach for the simulation of agglomerate UCs in the FEM framework was presented by Pontefisso et al. [87]. The article focuses on an algorithm for the generation of agglomerate UCs with a high filler weight or volume fraction and also discusses the application of this algorithm to an artificial NC material. The dependence of the Young's modulus on the number of primary particles per agglomerate, the agglomerate volume fraction and the properties of the artificial interphase is discussed. A quite low influence of the agglomerate size on the Young's modulus was observed. The article is intended to introduce a modeling approach for agglomerate UCs, that can be fed with data from other sources, rather than providing a comprehensive study of the phenomenon of agglomeration inside of NCs. Still, as it is, it completely ignores the underlying molecular structure and neglects several effects, e.g. related to resin-free areas inside of the agglomerates or the agglomerate size distribution.

Concluding, the literature concerning the numerical investigation of the influence of agglomeration on the mechanical properties of NCs is incomplete. The ultimate goal of the present thesis is to introduce a hierarchical multi-scale framework, with which the open questions can be addressed and the mechanical properties of RVEs containing agglomerated NPs can be predicted. Therefore, the necessary material input of each constituent of the NC (i.e. boehmite, epoxy, the BNP-epoxy interphase and the BNP interactions) is calculated on the atomistic scale using MD simulations. The resulting elastic properties are homogenized and transferred to the microscale, on which at first agglomerate UCs are modeled and simulated using the FEM. To account for possible resin-free areas, the idea of the DEM is adopted, where the particles are treated as point masses and the interaction between the particles is modeled by spring elements (for further details see section 6.3.1). Ultimately, in a second homogenization step, the findings from the agglomerate UCs are passed to the agglomerate RVEs, which include the influence of the agglomerate size distribution. The idea of the whole multi-scale approach is introduced in detail in the following chapter. Details about the model generation and the simulation results on the microscale can be found in chapter 6.

2 Multi-Scale Analysis

The main purpose of this chapter is to present the idea of the proposed multi-scale framework in detail. Additionally, an introduction to the theory of multi-scale analysis and homogenization is given, in which the mathematical and modeling framework for the calculation of the effective elastic properties is discussed with respect to the present problem.

2.1 Idea of the Proposed Multi-Scale Framework

The term multi-scale analysis denotes the investigation of a problem that covers several time or length scales. In the context of this thesis, as in the field of mechanics in general, it is understood as a framework to incorporate lower-level effects (e.g. caused by a heterogeneous microstructure or by a time-dependent material behavior) into the simulation of macroscopic structures or materials. Here, especially the spatial transition from the atomistic level to the microscale and from the microscale to the macroscale is focused.

Three main types of multi-scale analyses exist: the concurrent, the semi-concurrent and the hierarchical multi-scale analysis. In the concurrent multi-scale analysis, the simulations on the different scales are coupled and carried out simultaneously. For instance, in the FE framework, all integration points of the higher scale can be coupled to an underlying RVE on the lower scale, which describes the effective behavior at this material point. The main advantage of this approach is that no material model is needed to describe the macroscopic material behavior. This, in turn, implies that the transfer of the material behavior from the micro to the macroscale can be free of any assumptions (e.g. rheological models), which are typically necessary for the development and characterization of material models. However, the efficiency of this approach is usually low, since both the macro and the micro model are analyzed at every time increment. To confine the run times, it is crucial to choose the RVE as small as possible and to create meshes as coarse as possible, especially on the fine scale. Furthermore, the definition of correct boundary conditions (BCs) to transfer the respective stress or strain states both from the higher to the lower and from the lower to the higher scale can be challenging.

The semi-concurrent multi-scale analysis can be understood as a special case of the concurrent approach. The simulations on the two scales are still carried out

simultaneously and information is transferred both from the coarse to the fine scale and vice versa. Hence, both approaches can be assumed to have a comparable efficiency. The main difference of the semi-concurrent multi-scale analysis is that the compatibility and the momentum balance are only satisfied approximately. A common example is the FE^2 method [88, 89]. Generally, semi-concurrent multi-scale approaches are more flexible and allow for a coupling of different software packages, such as MD and FE software [90, 91].

In the hierarchical multi-scale analysis, simulations on the different scales are performed independently and sequentially. Typically, starting with the simulation on the lowest scale, the desired properties are homogenized and passed as an input to the next higher scale. For instance, in the FE framework, a microscale RVE, e.g. containing voids, can be simulated and used for the homogenization of the mechanical properties. Based on the results, a material model that describes the macroscopic material behavior can be calibrated. The main advantage of this approach is a much higher efficiency since the simulations on the lower scale have to be carried out only once, no matter how many calculations are performed on the macroscale. Thus, RVEs can be much more refined, which might lead to more accurate results. Additionally, a direct coupling and the transfer of the stresses and strains between the two scales is no longer required. The main challenge is the development and calibration of appropriate material models on the higher scale.

The framework proposed in this thesis involves two homogenization steps, as illustrated in Fig. 2.1. In the first step, the elastic properties of the bulk epoxy, the interphase and the boehmite are homogenized on the atomistic scale and inserted into the microscale FE models. In the second homogenization step, these microscale FE models are homogenized again, to obtain the macroscopic elastic properties, which could be used to simulate macroscopic particle reinforced structures or to continue the homogenization process for particle- and fiber-reinforced composites. The simulations on the mesoscale and macroscale are, however, not part of this thesis. To perform the homogenization from the atomistic scale to the microscale, in a concurrent or semi-concurrent multi-scale scheme a coupling between MD and FEM would be required for each integration point of the microscale model. Though the molecular dynamic finite element method (MDFEM, [92–94]) generally provides a suitable framework to realize this coupling, MD methods are not efficient enough to calculate coupled MD/FEM-RVEs within a reasonable run time, especially not for parametric studies. Furthermore, in a concurrent coupling of atomistic and continuum simulations, it is unclear how to enforce the compatibility between the two scales. Due to these limitations, in the scope of this thesis, a hierarchical multi-scale approach is developed.

A detailed schematic illustration of the proposed framework is shown in Fig. 2.2. Please note that in the scope of this thesis the term microscale is not used for the fiber matrix level, which it is often associated with for FRPs, but for the scale, on

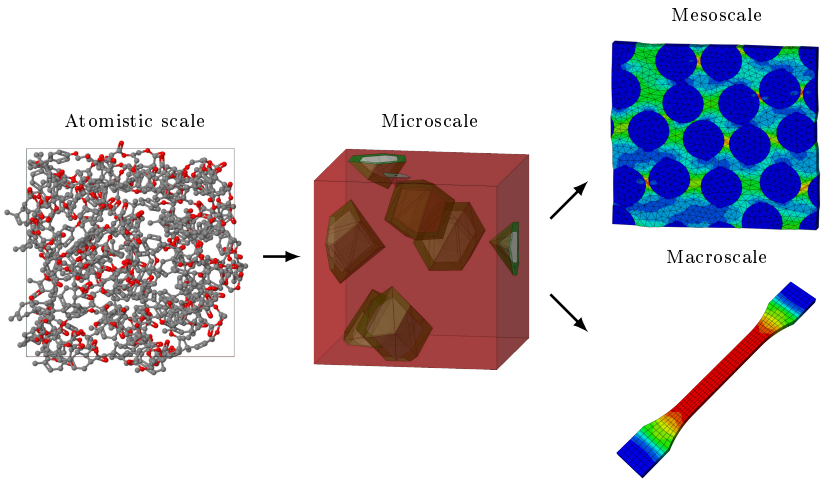

Figure 2.1: Homogenization steps from the atomistic scale to the microscale and from the microscale to the meso / macroscale.

which the particle-matrix interactions are investigated. To explain the proposed framework, let's first consider the higher scale, the microscale, on which ultimately two cases are simulated. Firstly, RVEs of homogeneously distributed BNPs in an epoxy matrix are considered. These models are used to calibrate the microscale simulations by e.g. comparing different types of BCs (periodic BCs (PBCs) and displacement BCs (DBCs)) and investigating a possible mesh size dependency. More details can be found in section 2.2.2 and section 6.2.2. Additionally, the influence of the interphase on the elastic properties can be investigated separated from effects related to agglomeration. The second type are agglomerate RVEs. These models contain agglomerates in a statistically homogeneous way according to the experimental agglomerate size distribution. Therefore, in an intermediate step, the mechanical properties of agglomerate UCs embedded in the epoxy matrix are calculated and the effective UC properties are transferred to the agglomerate RVEs. The reason for this two-step approach are numerical restrictions, which prevent the model generation and simulation of RVEs containing multiple large agglomerates. Average agglomerate sizes in the present material system are reported to be 105 nm [95]. Assuming, for simplicity, spherical particles and a dense sphere packing, the number of primary particles in one average agglomerate can be estimated to be around 300. The numerical cost of such an agglomerate UC is too high to possibly realize RVEs without an intermediate step.

In reality, it is unknown to which extent agglomerates are filled with polymer. It

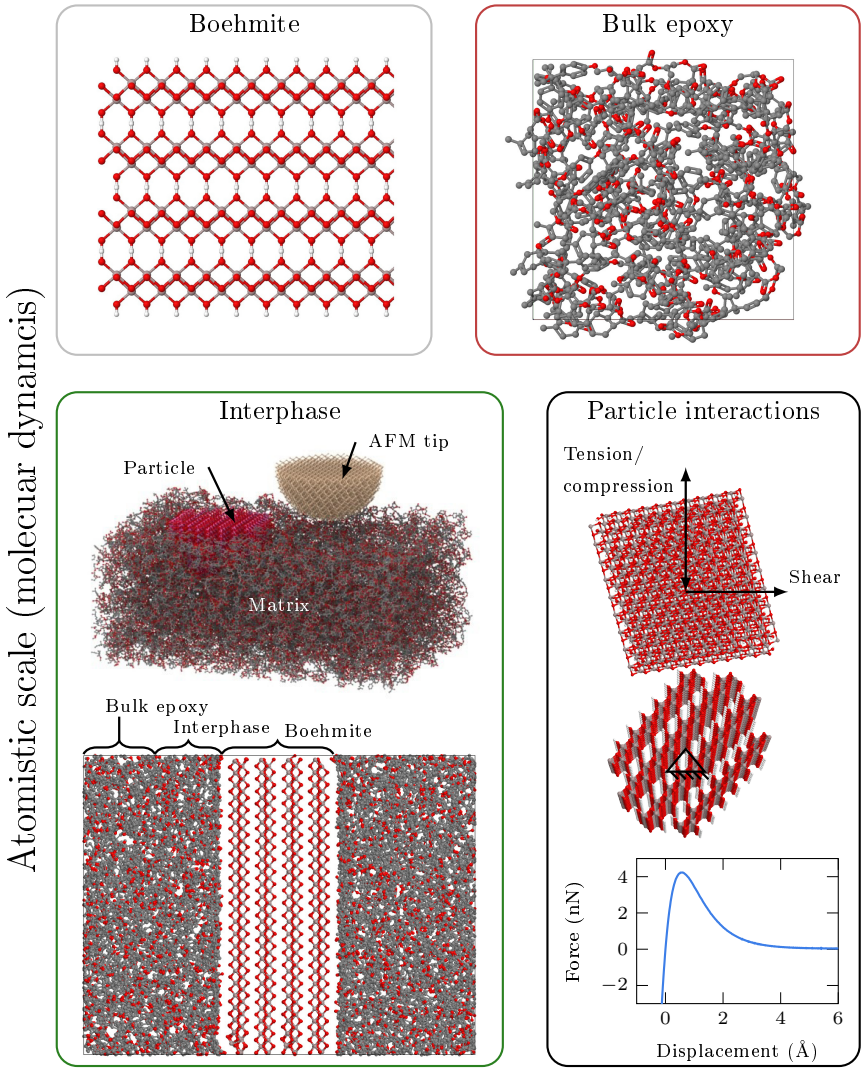
Atomistic scale (molecuar dynamcis)
Boehmite
Bulk epoxy
Interphase
AFM tip
Particle
Matrix
Bulk epoxy
Interphase
Boehmite
Particle interactions
Tension/
compression
Shear
Force (nN)
4
2
0
−2
0
2
4
6
Displacement (Å)

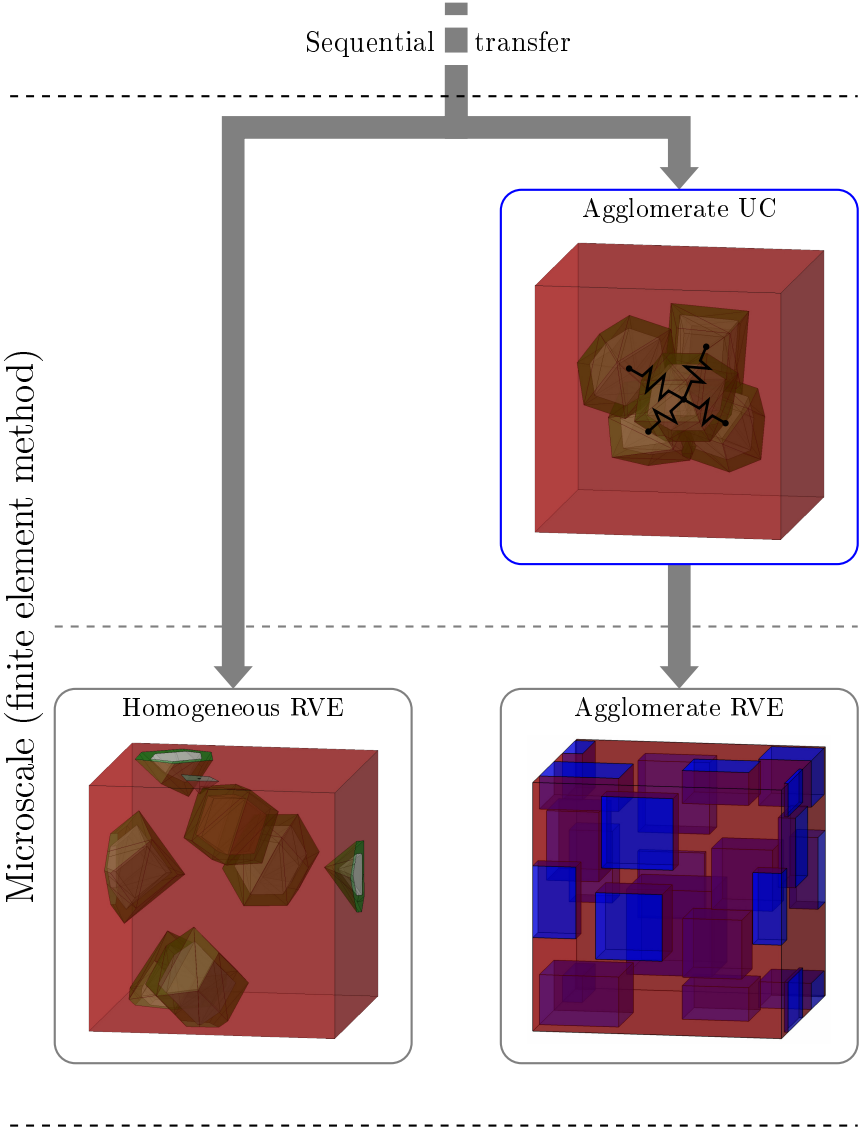

Figure 2.2: Schematic illustration of the proposed hierarchical multi-scale scheme.

is imaginable that this question can have a tremendous influence on the overall behavior of the NC. If the agglomerates are filled (see Fig. 2.3 (a)), the polymer can possibly bond to the primary particles and thus stabilize the agglomerate and improve the stress transfer between the primary particles. At the same time, a chemical bonding between the BNPs and the epoxy can result in a network morphology that significantly deviates from the bulk polymer. In case of unfilled agglomerates (see Fig. 2.3 (b)), the stress transfer between the primary particles is solely realized through the nonbonding interactions between the particles (indicated by the springs in Fig. 2.3 (b)), which could result in a considerable reduction of the stiffness of the unfilled agglomerate compared to the filled one. To account for this question, the two different cases are implemented as follows. In the first case, in which the agglomerates are filled with polymer, the models are a special case of the previously mentioned homogeneously distributed RVEs with clustered NPs, but solely based on continuum mechanics. The interesting effect in these models is the overlap of the interphases caused by the closely located BNPs, which causes an overall reduction of the interphase volume. In the second case, in which the agglomerates are unfilled, the polymer region inside the agglomerates is removed. The interparticulate interactions are described by a DEM-like approach as non-linear spring elements. More details about the modeling of all described cases can be found in chapter 6.

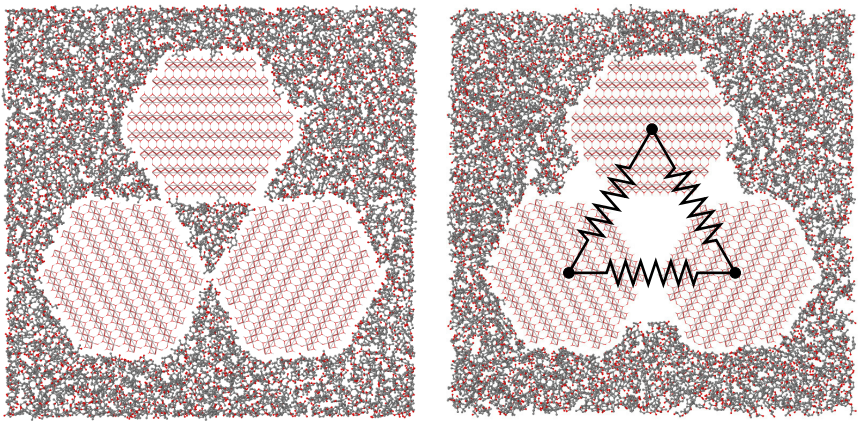

(a) (b)

Figure 2.3: Schematic illustration of (a) an agglomerate filled with polymer and (b) an unfilled agglomerate. The springs visualize the interparticulate interactions.

To generate and simulate the microscale models, input from the lower atomistic scale, such as the elastic constants or the thickness of the interphase region, is

needed. The starting point are MD simulations for the determination of the elastic properties of the pure constituents, namely the boehmite and the epoxy. Typically, this is done by virtual tensile tests, which are nowadays standard MD applications. However, the characterization of both materials turned out to entail certain difficulties, that needed further attention. On the one hand, virtual tensile tests of boehmite showed large deviations from the results of AFM experiments. By simulating AFM on BNP/epoxy samples, the cause of these differences could in large parts be clarified, as discussed in chapter 3. On the other hand, as explained in the introduction, the modeling, as well as the resulting properties of epoxy, depend on many parameters and factors, such as the strain rate or the degree of cross-linking. Hence, a proper calibration of the models can be challenging. A detailed discussion can be found in chapter 4.

As pointed out in the introduction, the interphase between the BNPs and the epoxy can considerably influence the NCs properties. However, a direct characterization of the mechanical properties of the interphase with respect to the interfacial bonding was not achieved so far in the literature, neither by experiments nor by numerical simulations. Within the proposed multi-scale framework, two different approaches are developed and compared. Firstly, the previously mentioned AFM simulations are conducted on the BNP/epoxy interphase with varying distance from the BNP surface, resulting in stiffness gradients throughout the interphase. Alternatively, a new approach for the direct calculation of local elastic properties from MD simulations is derived, which is also capable of capturing the stiffness gradient but can also directly deliver the effective interphase properties.

The missing ingredient for the simulation of the coupled FEM-DEM models representing the unfilled agglomerates are the interparticulate interactions between the primary particles. Therefore, a statistically representative number of models consisting of two randomly orientated primary particles is simulated under tensile, compression and shear load. The resulting force-displacement curves are used in non-linear spring elements on the microscale.

To the best knowledge of the author, the proposed framework represents the first attempt of collectively and comprehensively incorporating all the important aspects of NCs, such as the interphase, agglomeration and the agglomerate size distribution, into one multi-scale scheme.

2.2 Homogenization Procedure

Homogenization describes the process of simplifying a discrete or heterogeneous system to a homogeneous one. As mentioned before, in this thesis, a homogenization on the atomistic scale and a second homogenization on the microscale are performed. The mathematical framework for both is presented in the following.

2.2.1 Homogenization on the Atomistic Scale

Representative Volume Elements

To be representative of the material, the simulated volume elements (VEs) should fulfill the condition

$$l << a. \tag{2.1}$$

It states that the characteristic size l of any structural feature of the system should be considerably smaller than the size of the VE a. For a NC RVE, the characteristic size l can be interpreted as the primary particle or agglomerate size. However, since only the constituents of the NC but not the NC itself are simulated on the atomistic scale, here the characteristic length has a different meaning. An interpretation of l for the epoxy system could be the length of the monomer chains and the diameter of the curing agent molecule. In case of boehmite, this condition does not impose any restrictions, since the (ideal) boehmite crystal is periodic by nature.

A second condition for the choice of the VE size is the minimum-image convention. It states that each atom contained in the simulation only interacts with the closest image of the remaining atoms in the VE. This leads to the condition

$$a \geq 2R_c, \tag{2.2}$$

with R_c being the cutoff for the nonbonding interactions.

Boundary Conditions

With a few exceptions, which are marked as such in the following chapters, all atomistic simulations are performed using PBCs. The principle idea is that a small material excerpt is assumed to be embedded in periodic images of itself, forming an infinite and thus boundary-free sample (see Figure 2.4). The main advantage of this type of BCs is that due to the more realistic embedding the macroscopic properties can typically be calculated from fewer atoms compared to other types of BC, such as vacuum BCs.

The primary cell is virtually replicated in all spacial directions, that are present in the simulation, leading to 26 image cells in the 3D case. The image cells are exact copies of the primary cell, sharing its size, shape, the number of atoms, the position of each atom relative to the cell center of mass and the total momentum. To ensure this, atoms that are leaving the primary cell are reentering on the opposing box boundary. The periodicity is ultimately achieved by allowing the atoms of the

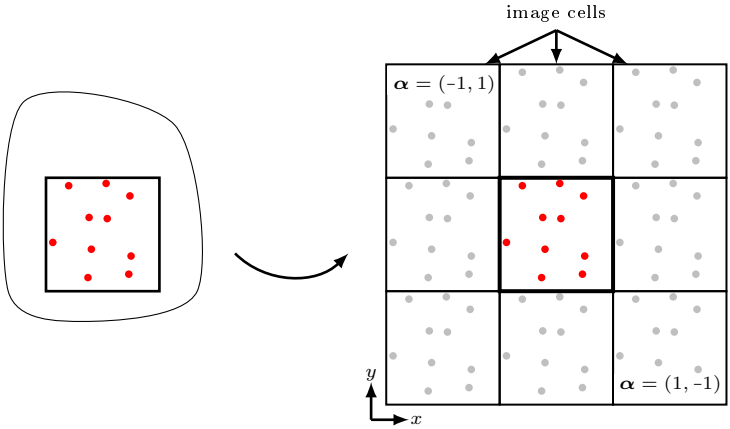

Figure 2.4: 2D schematic illustration of the idea of PBCs in MD simulations. $\boldsymbol{\alpha}$ is the normalized direction vector of the image cell.

primary cell to interact with the image atoms of the neighboring cells, by formulating the interatomic force between atom n and $\tilde{m}$

$$\boldsymbol{f}^{n\tilde{m}} = -\frac{\partial U(\boldsymbol{r}^{n\tilde{m}})}{\partial \boldsymbol{r}^{n\tilde{m}}}, \tag{2.3}$$

with

$$\boldsymbol{r}^{n\tilde{m}} = \boldsymbol{r}^{nm} - \boldsymbol{\alpha}\boldsymbol{L}. \tag{2.4}$$

Thereby, $\tilde{m}$ is the index of all neighboring image atoms of atom n within the non-bonding cutoff R_c, m is the index of the corresponding primary cell atom and $\boldsymbol{L}$ denotes the vector of the box sizes. The vector

$$\boldsymbol{\alpha} = \begin{bmatrix} \boldsymbol{\alpha}_1 \\ \boldsymbol{\alpha}_2 \\ \boldsymbol{\alpha}_3 \end{bmatrix}, \text{ with } \boldsymbol{\alpha}_1, \boldsymbol{\alpha}_2, \boldsymbol{\alpha}_3 \in [-1, 0, 1], \tag{2.5}$$

describes the normalized direction vector of the image cell the neighbor atom $\tilde{m}$ is located in (see also Fig. 2.4). Each atom n can experience forces induced by each atom m from the primary cell and each atom $\tilde{m}$ from all image cells. To avoid a double count of interactions or interactions of the atom n with an image of itself, the cutoff for the physical interactions under PBCs is truncated to $R_c \leq 1/2 \min(\boldsymbol{L})$ (compare Eq. 2.2), which is the already introduced minimum image convention.

Calculation of the Effective Elastic Properties

The main challenge in the homogenization process from the atomistic to the microscale is an appropriate definition of the stress and the strain on the lower scale, since both are continuum measures and thus per se not defined in discrete systems. However, by applying the previously described PBCs, the strains can easily be calculated from the deformation of the simulation box according to

$$\langle \epsilon_{ij} \rangle_V = \frac{u_{ij}}{h_{ii}} \tag{2.6}$$

Thereby, $\langle \cdot \rangle_V$ denotes the volume average and u_{ij} is the j-th component of the displacement vector of the box boundary perpendicular to i (see Fig. 2.5). The matrix $\boldsymbol{h}$ is defined as

$$\boldsymbol{h} = \begin{bmatrix} a & 0 & 0 \\ 0 & b & 0 \\ 0 & 0 & c \end{bmatrix}, \tag{2.7}$$

where a, b and c are the VE dimensions.

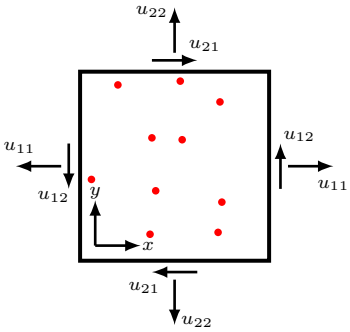

Figure 2.5: 2D schematic illustration of the displacement vectors on the VE boundaries.

The choice of a stress measure is not as straight forward. Two approaches are controversially discussed in the literature, which mainly differ by the question whether a kinetic contribution should be considered or not. In the article of Zhou [96], it is shown that the commonly accepted form of the virial stress including the kinetic term is wrong. However, later, other studies, like [97], claimed that the formulation derived by Zhou [96] is also incorrect. Since there is neither a proof nor an absolute consent in the literature, here, the well accepted virial stress is used. It was firstly proposed by Clausius [98] and has been empirically shown to provide an appropriate

equivalent to the Cauchy stress of a continuum. According to [75], the stress of the simulation box is defined as

$$\langle \boldsymbol{\sigma} \rangle_V = \frac{1}{V}(-\sum_n m^n (\boldsymbol{v}^n - \langle \boldsymbol{v} \rangle_V) \cdot (\boldsymbol{v}^n - \langle \boldsymbol{v} \rangle_V) + \frac{1}{2} \sum_{n,m \neq n} \boldsymbol{r}^{nm} \cdot \boldsymbol{f}^{nm}). \tag{2.8}$$

Thereby, V is the volume of the simulation box, m^n is the mass of atom n, $\boldsymbol{v}^n$ is the velocity vector of atom n, $\langle \boldsymbol{v} \rangle_V$ is the vector of the average velocity of all atoms in the VE, $\boldsymbol{r}^{nm}$ is the vector pointing from atom n to atom m and $\boldsymbol{f}^{nm}$ is the force vector between these two atoms. The first term in the parenthesis in Eq. (2.8) is related to the kinetic energy, which mainly arises from thermal movements of the atoms and deformations at high strain rate. The second contribution describes the potential energy stored in the interatomic interactions.

With known stresses and strains, the effective elastic properties can be obtained by solving Hooke's law

$$\langle \boldsymbol{\sigma} \rangle_V = \mathbb{C} : \langle \boldsymbol{\epsilon} \rangle_V . \tag{2.9}$$

Calculation of the Local Elastic Properties

The aforementioned procedure works well for calculating the elastic properties of the bulk epoxy and the boehmite crystal. However, in general, it can only be used to determine the elastic properties of the whole model but not of a phase or region contained in the model. This limitation arises from the fact that both the stress and strain formulation depend on the VE dimensions and volume (compare Eq. 2.6, Eq. 2.7 and Eq. 2.8). The interphase cannot be separated from the other phases and only exists in their presence. In other words, a VE containing only the interphase does not exist. It should furthermore be kept in mind that, in contrast to continuum mechanics, no element stress or strain definitions exist in MD, which could be used to calculate local elastic properties. Thus, a different approach to extract the elastic interphase properties is necessary. In the following, a new method for the calculation of the elastic properties of subsections of molecular models is described, as also published in [99]. Therefore, it is necessary to define stresses and strains in the subsections in such a way that they no longer depend on the VE dimension and volume. In this thesis, these subsections can be understood as slices of the simulation box, which can easily be generalized to arbitrarily shaped contiguous geometric regions. To ease the comprehensibility, Fig. 2.6 shows a schematic illustration of the approach and introduces some of the variables used.

Following the definition of the virial stress (see Eq. 2.8), the stress of region R is

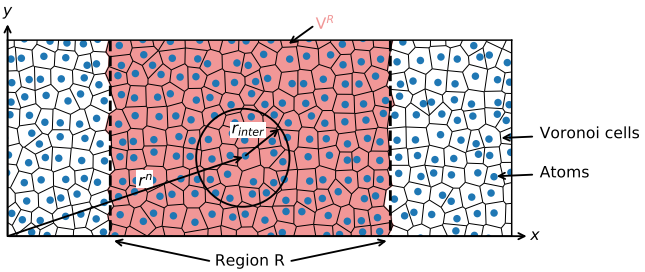

Figure 2.6: Schematic illustration of the approach for the calculation of the local elastic properties from MD simulations

defined as

$$\begin{aligned}\langle\sigma_{ij}\rangle_R &= \frac{1}{V^R}\sum_{n\in R} V^n\sigma_{ij}^n \\ &= \frac{1}{V^R}\sum_{n\in R}(-m^n(v_i^n - \langle v_i\rangle_R)\cdot(v_j^n - \langle v_j\rangle_R) + \frac{1}{2}\sum_{m,m\neq n} r_i^{nm}\cdot f_j^{nm}),\end{aligned} \tag{2.10}$$

where the first sum is performed over all atoms n associated with region R, instead of over all atoms contained in the simulation box. This is the main difference to the previously introduced virial stress. The volume of region R is chosen to be the sum of the Voronoi volumes of all atoms n in region R, which converges to the geometric volume of the region for a sufficiently large number of Voronoi cells. Furthermore, in the above equation, i and j represent the spatial directions. It should be noted that in MD, in contrast to continuum mechanics, always the the product $V^n\sigma_{ij}^n$ is calculated, not the stress σ_{ij}^n itself. This is a result of the atomic force fields used in MD, which replace the continuum material models. In the second line in Eq. 2.10, all variables following the first sum are calculated by the solver, which means that the product $V^n\sigma_{ij}^n$ in the first line is explicitly given. This implies that the controversial choice of an atomic volume V^n is not necessary to obtain $\langle\sigma_{ij}\rangle_R$.

To define a strain measure for subsection R, which is independent of the VE dimensions, an atomic strain measure needs to be defined. Following the approach of Falk and Langer [76], the strain associated with atom n is defined as

$$\epsilon_{ij}^n = \sum_k X_{ik}^n (Y_{jk}^n)^{-1} - \delta_{ij}, \tag{2.11}$$

with

$$X_{ij}^{n} = \sum_{m} (r_i^{m,ref} - r_i^{n,ref})(r_j^{m,def} - r_j^{n,def}) \tag{2.12}$$

and

$$Y_{ij}^{n} = \sum_{m} (r_i^{m,ref} - r_i^{n,ref})(r_j^{m,ref} - r_j^{n,ref}). \tag{2.13}$$

In the above equations, the variable $r_i^{n,ref}$ denotes the i-th component of the position of atom n in the reference configuration. Similarly, the index def refers to the deformed configuration. The atom positions are assumed to be time averaged for both configurations, so that all atomic movements related to thermal vibrations are averaged out. The index m in Eq. (2.12) and Eq. (2.13) loops over all neighbor atoms of atom n within a certain interaction radius r_{inter}, which has to be chosen according to the investigated problem (e.g. the investigated material). The choice of r_{inter} for the present problem is shown in section 4.4.6. The strains of subsection R are therewith defined as

$$\langle \epsilon_{ij} \rangle_R = \frac{1}{V^R} \sum_{n} V^n \epsilon_{ij}^n. \tag{2.14}$$

With known stress and strain, the elastic constants of region R can be obtained by solving Hooke's law (compare Eq. 2.9)

$$\langle \sigma_{ij} \rangle_R = C_{ijkl}^R \langle \epsilon_{ij} \rangle_R. \tag{2.15}$$

Both the atomic strain method and the presented stress formulation provide the full strain and stress tensors. Thus, this framework is generally applicable to an anisotropic material behavior. For simplicity, in this thesis, an isotropic material is assumed, which reduces C_{ijkl}^R to two unknowns, which are the Young's modulus E^R and the shear modulus G^R. It should be noted that the approach is generally not limited to the calculation of elastic properties. Full stress-strain curves including the inelastic behavior can be sampled by using more than one deformed configuration. This idea is shown for the case of pure epoxy in section 4.4.6.

2.2.2 Homogenization on the Microscale

Representative Volume Element and Unit Cell

Per definition, the term RVE describes an excerpt of the material, that contains all relevant components of the real material in a statistically representative distribution.

This can be expressed by the previously introduced Eq. 2.1, which states that the RVE size a should be considerably larger than the characteristic length l of all structural features. On the microscale, l can be interpreted as the particle or agglomerate diameter. However, in practical application, it is often unclear how to fulfill this criterion. Thus, parametric studies with increasing VE size are performed, until the target property converges, as exemplarily shown in Fig. 2.7 (a). Due to the random nature of the VEs, for each size, a statistically representative number of realizations is simulated, until the standard deviations of the target property converge, as shown in Fig. 2.7 (b).

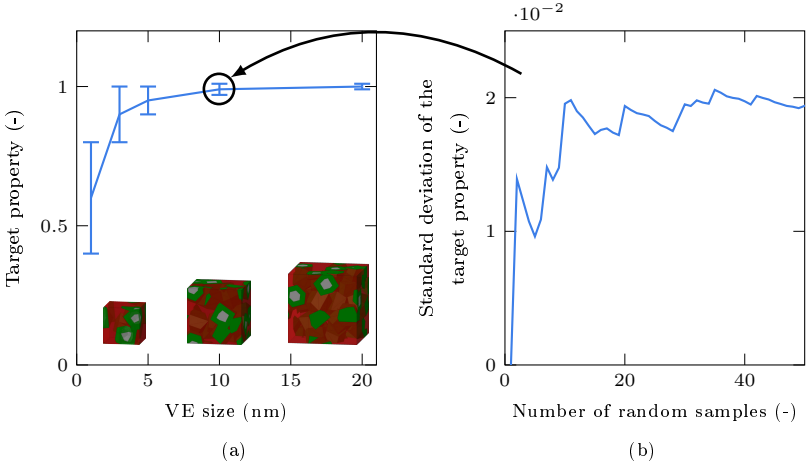

Figure 2.7: Illustration of the procedure for determining the microscale RVE size: (a) parametric studies with increasing VE size to ensure representativeness of the VE and (b) convergence study of the standard deviation of the target property for each VE size to account for the random nature of the VEs.

In this thesis, the above idea is applied to the homogeneous and the agglomerate RVEs. As discussed earlier, for the simulation of the agglomerate RVEs, the results of intermediate agglomerate UCs are necessary. These agglomerate UCs are simulated with a varying number of primary particles between 3 and 300. For each case, the number of random samples is increased, until the standard deviation converges. To understand this approach, three facts should be noted. Firstly, as a special case of the RVE, a UC features only one subcomponent (one agglomerate in the scope of this thesis) and thus represents a periodic heterogeneous microstructure. This is not the case for the present NC, which is why in a subsequent step the higher scale

agglomerate RVEs are considered. Secondly, the definition of the UC presented here is slightly different from the one the reader might be familiar with. Typical fiber or particle UCs do not contain any effects related to a random conformation, meaning that a repetition of the simulation of the UC will predict the same properties as the previous realization. If the subcomponent becomes an agglomerate, however, this does not hold anymore. The agglomerates themselves consist of multiple primary particles and thus have a random inner structure. The UCs are not unique anymore, which leads to the requirement of statistical investigations on the UC. Thirdly, the statistical investigations on the UCs should no be confused with the convergence study of the RVEs. Each UC represents one specific agglomerate size from the agglomerate size distribution. An increase in the number of primary particles and hence the UC size does not lead to more representative results.

Boundary Conditions

The main goal of a homogenization from microscale to macroscale is the transfer of the microscopic discontinuous stress and strain fields to the macroscopic stresses and strains. Thereby, the Hill condition [100]

$$\langle \boldsymbol{\sigma} : \boldsymbol{\epsilon} \rangle = \langle \boldsymbol{\sigma} \rangle : \langle \boldsymbol{\epsilon} \rangle \tag{2.16}$$

must be fulfilled, which states that the energy stored in the discontinuous micro fields $\boldsymbol{\sigma}$ and $\boldsymbol{\epsilon}$ must be equal to the energy stored in the macroscopic stresses $\langle \boldsymbol{\sigma} \rangle$ and strains $\langle \boldsymbol{\epsilon} \rangle$. The simplest assumptions, that fulfill this condition, are the average strain theorem proposed by Voigt [101] and the average stress theorem proposed by Reuss [102]. In a practical application, these approximations can be realized through DBCs and traction BCs, as shown in Figure 2.8. The DBCs prescribe a uniform displacement to each boundary, whereas the traction BCs do the same for the traction. It is comprehensible, that DBCs prevent any deformation of the boundaries and thus add artificial stiffness to the RVE. In contrast, traction BCs lack the support of the surrounding material and thus typically lead to an unrealistically soft behavior. Hence, the Voigt and Reuss approximations are known to provide upper and lower bounds to the elastic parameters.

Another approach, which is known to result in a more realistic prediction of the material constants, is the use of PBC, which can be regarded as a mixture of the Voigt and Reuss approximations. The fundamental idea is to enforce periodic displacements and anti-periodic traction on each pair of opposing boundaries. In a practical application, this is achieved by coupling the degrees of freedom of the nodes lying on the opposite boundaries, as shown in Figure 2.9.

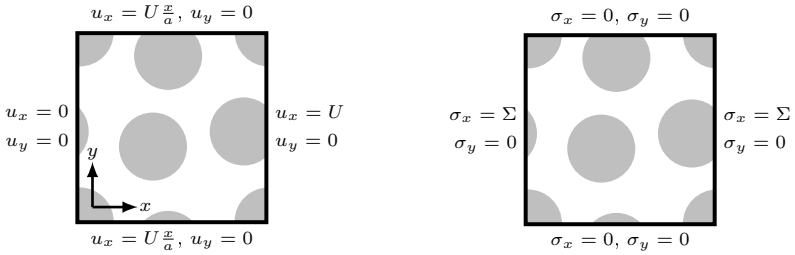

Figure 2.8: 2D schematic illustration of a tensile load in x-direction with (a) DBCs and (b) traction BCs.

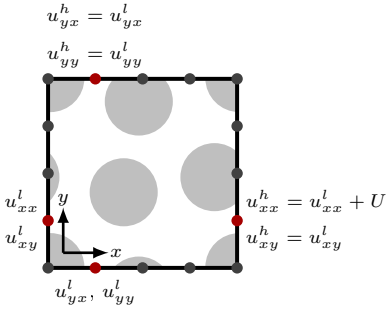

Figure 2.9: 2D schematic illustration of a tensile load in x-direction with PBCs.

The choice of the BCs is targeted in section 6.2.2. Since PBCs require a more complex modeling, it is investigated if PBCs are necessary or if DBCs are sufficient for the present problem.

Calculation of the Effective Elastic Properties

To calculate the effective elastic properties, firstly the stresses and strains have to be homogenized. This is achieved by a volume averaging according to

$$\langle \cdot \rangle_V = \frac{1}{|V|} \int_V \cdot dV. \tag{2.17}$$

Here, $\cdot$ is replaced by the stress and strain tensors $\boldsymbol{\sigma}$ and $\boldsymbol{\epsilon}$ and V is the deformed volume of the microscale model. The homogenized stresses and strains are then used to calculate the stiffness matrix by solving Hooke's law from Eq. 2.9. In the scope of this thesis, this procedure is applied to the RVEs containing homogeneously distributed primary particles and to the agglomerate RVEs. As stated before, the intermediate level agglomerate UCs can be regarded as a mixture between FEM and DEM. The usage of spring elements for the description of the interparticulate interactions inside of the agglomerates makes an evaluation of Eq. 2.17 impossible. However, the stresses can alternatively be calculated from the reaction forces acting on the boundary of the UC divided by the cross-section. Assuming a uniaxial and uniform strain, the stresses can be written as

$$\langle \sigma_{ij} \rangle_V = \frac{F_{ij}}{h_{jj} h_{kk}}, \tag{2.18}$$

where F_{ij} is the j-th component of the reaction force on the boundary with the normal direction i, see Figure 2.10. The matrix $\boldsymbol{h}$ was previously defined in Eq. 2.7 as the matrix of the RVE box vectors.

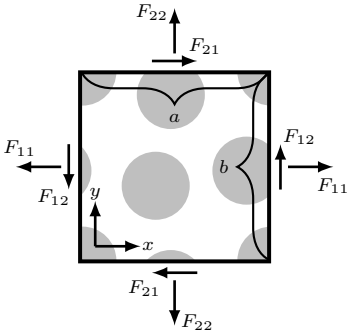

Figure 2.10: 2D schematic illustration of the reaction force vectors on the VE boundaries.

Alternatively to Eq. 2.17, the homogenized strains can be calculated from the relation

$$\langle \epsilon_{ij} \rangle_V = \frac{u_{ij}}{h_{ii}}, \tag{2.19}$$

where u_{ij} is the j-th component of the displacement on the boundary with the normal direction i. The equivalence of both approaches is shown for the homogeneous RVEs in section 6.2.2.

3 Atomistic Scale: Boehmite

The state of the art presented in section 1.3.2 shows that studies of the mechanical behavior of boehmite can rarely be found in the literature. This is mainly because boehmite crystals are not stable in a sufficient size to perform classical mechanical tests. In collaboration with the BAM, a comprehensive investigation of the material behavior of boehmite was conducted, as published in [33]. This article provides the basis for large parts of this chapter.

Due to the chronological development of this thesis, the work presented in this chapter was performed in a molecular static way using the molecular dynamic finite element method (MDFEM) [92], while some of the newer results presented in the following chapters were obtained with a full-featured MD approach using LAMMPS [103]. The MDFEM, in the way it is used, can be understood as an implementation of the MD into the finite element framework. This means that fundamental formulations, like the MD force fields, are implemented, but no thermostats and barostats are used. Thus, the simulations are carried out with a micro-canonical ensemble (NVE), in which the number of atoms, the volume and the total energy are controlled. However, a proper initialization of the temperature was not performed, so that these simulations are run at a low temperature in the range of 0 to 50 K. From experiments, it is known that crystalline materials show a minor dependence of the elastic properties on the temperature, especially at temperatures below the room temperature. This was shown by Wachtman et al. [104] and Spriggs et al. [105]. The reason for this is the ordered lattice structure of crystalline materials, which is, in contrast to other materials, such as polymers, not significantly altered by temperature. Hence, despite of the comprised inaccuracies, the applied approach can still provide realistic results. Another general disadvantage of the used implementation of the MDFEM is that no PBCs are available. Instead, a mixture of free boundaries and rigid BCs was used, as explained in detail later. The advantage of PBCs, which are the standard BCs in MD simulations, is that they mimic a realistic embedding of the sample as an excerpt of an infinitely large material. Since boundary effects decrease with increasing sample size, PBCs can help to reduce the required model size or result in a more realistic approximation of the desired property for a given model size. However, for the AFM simulations, which are discussed in the following, the benefit of PBCs is rather small. This is on the one hand because it is unfeasible to apply PBCs in the loading direction on the top surface, where the sample is indented by the AFM tip. On the other hand, the required sample size is largely

defined by the probe volume and hence by the AFM tip diameter. PBCs applied perpendicular to the loading direction can certainly reduce the sample sizes or allow for bigger AFM tips, but the benefit is judged to be rather small. To avoid an influence of the boundaries on the measured Young's modulus, parametric studies concerning the sample size are performed in the following. In summary, the results presented in this section should give a reasonable prediction of the material behavior of boehmite. Still, from the authors' today's point of view, it is recommendable to verify the following explications with a full-featured MD approach to exclude possible effects related to the above discussion.

3.1 Summary of the Experimental Characterization of Boehmite

The experimental results presented in this section are not the scientific product of the author. All credit goes to the esteemed colleagues of the BAM. Here, only the main results are discussed, while details, e.g. about the experimental setup or the sample preparation are omitted. Further details can be found in [33].

The starting point for the comprehensive experimental and numerical studies of boehmite was the experimental investigation of commercially available BNPs [36] embedded in a polymer matrix (Epoxy Araldite LY 3585 [106]). The samples were measured with amplitude-dependent force spectroscopy (ADFS), which cannot yet be used for the direct calculation of the Young's modulus. However, by identifying the curves that can be ascribed to the boehmite particles and comparing the results to materials with known elastic constants (epoxy with $E \approx 3.5$ GPa and glass with $E \approx 70$ GPa), the Young's modulus of boehmite was determined to fulfill the condition

$$3.5\ GPa < E_{boehmite} < 70\ GPa. \tag{3.1}$$

This value is suspiciously lower than expected from the literature (compare section 1.3.2) and preliminary numerical tensile tests, which were conducted for testing purposes.

To investigate the cause of the unexpected behavior, three possible explanations were identified and discussed, which are effects related to the crystal size, the slippage of the weakly linked boehmite layers and the presence of amorphous boehmite domains. To be able to distinguish these effects, besides the aforementioned BNP/epoxy samples, two additional samples were investigated experimentally. These complementary samples had a different morphology and featured substantial differences in crystallinity and sample size. Thus, they provide evidence of the impact of each of the possible explanations on the stiffness of boehmite. The first complementary sample was a boehmite crystal of a size of approximately 80 µm from a geological sample, which was prepared on a glass substrate. As a second complementary sample, boehmite was synthesized with a very low crystallinity to investigate the

possible explanation of the presence of amorphous boehmite. All samples were analyzed through X-ray diffraction and Raman spectroscopy and shown to be boehmite. Furthermore, it was proven that the second complementary sample indeed had a low crystallinity. The three samples were mechanically investigated with three different AFM modes: tapping mode (which provides the topography), FDC and ImAFM with the resulting ADFS curves. For more details about these methods, the reader is referred to [33]. The FDC measurements of the geological sample resulted in a Young's modulus of 11 GPa, which is in the same range as the stiffness determined on the BNP/epoxy sample using ADFS. Furthermore, no distinct permanent deformation was found and a Hertz fit was possible, which typically indicates a purely elastic behavior. The last sample, which featured a low crystallinity, was significantly softer and showed a much more distinct inelasticity than the two previous samples.

The cause of the unexpectedly low stiffness, which was initially observed for the BNP/epoxy sample, cannot conclusively be explained from the experimental measurements. The sample with the low crystallinity showed an even lower Young's modulus than the other two samples that the presence of amorphous boehmite domains was ruled out as the cause for the low Young's modulus. A possible conclusion is the combination of the remaining two hypotheses. Following the argumentation in [33], the soft behavior could mainly be caused by the slippage of boehmite layers. For the small boehmite particles embedded in the epoxy matrix, this slippage can happen without any disturbance, resulting in the low Young's modulus and the inelastic behavior. It can furthermore be hypothesized that the geological sample shows the same effect but can restore the original structure due to the larger extent of the boehmite sheets and the far-field lattice structure. In other words, if only a small part of a large crystal is distorted, e.g. by a local buckling of boehmite sheets, the deformations can be restored to the original ordered structure by the surrounding material. This may result in a soft behavior and appear as a purely elastic, reversible deformation.

3.2 Numerical Characterization of Boehmite using AFM Simulations

The argumentation based only on the experiments is vague. In the following, AFM is simulated to substantiate or refute the findings and to provide further insight into the effects that lead to the unexpected material behavior. The testing conditions in the AFM experiments considerably differ from classical mechanical tests, such as tensile tests. Besides applying a compression load, a nonuniform stress distribution caused by the hemispherical shape of the AFM tip is introduced. Thus, numerical tensile tests (or compression tests) are not explicated here. Instead, a new simulation approach that mimics the testing conditions of the experiments is introduced. In

this section, the idea of these AFM simulations, the generation of the simulation models (see Fig. 3.1) and the respective simulation results are presented.

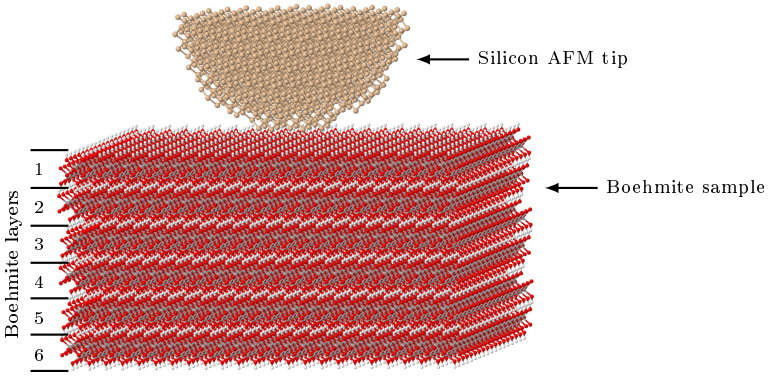

Figure 3.1: Exemplary boehmite AFM model.

3.2.1 Model Generation and Simulation Aspects

All molecular models used in this thesis are generated with an in-house software that integrates the open-source packages OpenBabel [107] and Packmol [108]. The credit for the implementation of the so-called "MolWizard" goes to my former colleague, Andreas Kempe. The realization and calibration of the specific materials investigated here as well as the generation of the AFM simulation models was realized by the author.

Based on XRD measurements carried out at the Institute for Particle Technology of the TU Braunschweig [109] and the article of Bokhimi et al. [28], the chemical unit cell of boehmite (Rhombic dipyramidal base-centered crystalline unit cell (cmcm), a = 2.87 Å, b = 12.23 Å and c = 3.69 Å) was constructed, as shown in Fig. 3.2 (a). Therewith, a larger boehmite structure is generated by duplicating the chemical unit cell to the desired extent, as shown in Fig. 3.2 (b). In order to validate the used boehmite structure, XRD simulations of the equilibrated crystalline structure were performed with the Mercury software [110] and compared to the XRD experiments from [109]. The result is shown in Fig. 3.3. The data contains two important characteristics, which are the intensity and the position (i.e. the reflex angle) of the detected peaks. The intensity strongly depends on the size and the shape of the investigated sample. For instance, the half width of the characteristic peaks can be used to calculate the size of the primary particles. Due to numerical restrictions,

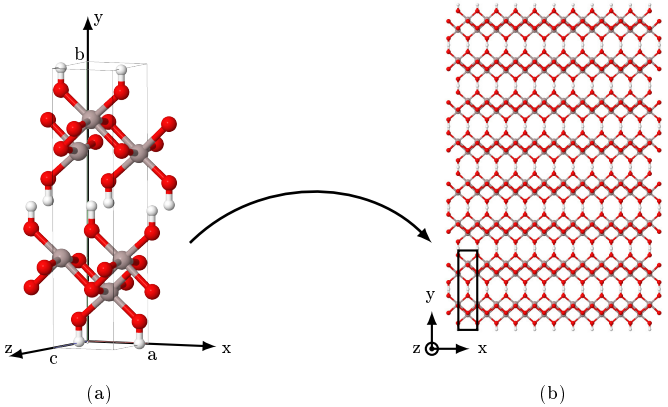

Figure 3.2: Chemical structures of (a) the unit cell of boehmite after [28] and (b) the boehmite model used in the XRD simulations consisting of $10 \times 4 \times 10$ unit cells.

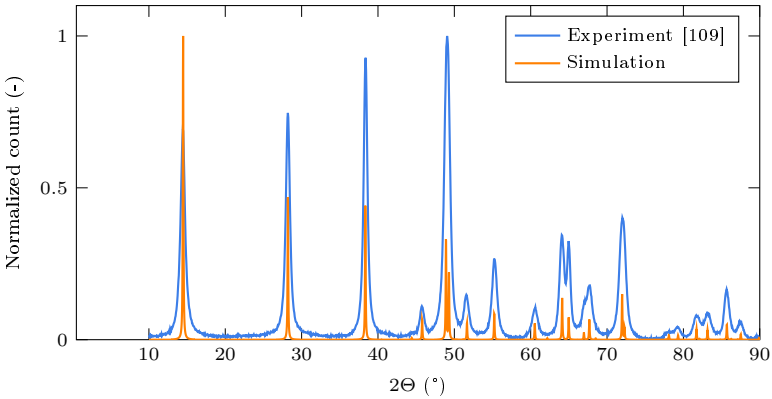

Figure 3.3: Comparison of the experimentally measured XRD pattern of boehmite from [109] and the simulated one.

the real primary particle size is too large to be processed in such a simulation. Instead, the model consists of 400 unit cells arranged in a rectangular prism and does not have the same size and shape as the real particles. Hence, the intensity cannot be compared and the position of the peaks is focused here. Fig. 3.3 shows that the reflex angles from the experiment and the simulation agree outstandingly,

which leads to the conclusion that the models sufficiently represent the crystalline structure of boehmite.

Fig. 3.4 shows a schematic illustration of the AFM models. The boehmite sample is generated similarly to the models used for the XRD simulations, as described above. Later in this section, primary particles embedded in the epoxy matrix are simulated. The shape of the primary particles is chosen based on information from the manufacturer [111] and experimentally confirmed by the Institute for Particle Technology from the TU Braunschweig [109]. Due to the numerical effort of the MDFEM, the primary particle size is reduced from 14 nm to 5 nm. To obtain the particle shape, the desired geometry is cut out after the duplication of the unit cell. The same procedure is applied to the AFM tip, which consists of silicone (Fd3m unit cell, unit cell size a = 3.5668 Å). An oxide coating, as it can be found in reality, is neglected here, since the resulting charges mainly influence the attraction and adhesion forces, but have a minor effect on the indentation itself. In case of the BNPs embedded in epoxy, the polymer only acts as an auxiliary material, that provides "natural" BCs for the particles and helps keeping the particles in place. The material behavior of the epoxy is not of interest in this chapter. Thus, the generation of the epoxy polymer is not explicated here but discussed in section 4.3.

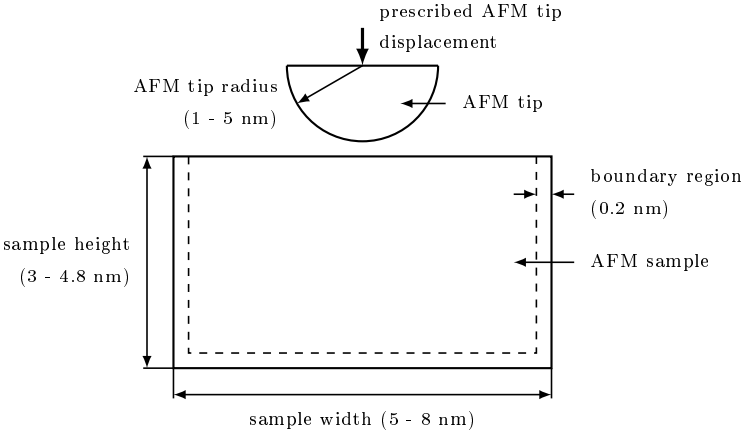

Figure 3.4: Schematic illustration of the AFM models.

All simulations presented in this section are performed using the MDFEM in combination with the Dreiding force field [112]. Even though it is possible to apply different cutoff radii for the nonbonding interactions within the sample and between sample and tip, a spherical cutoff of 15 Å has proven to be suitable for both cases by preliminary parametric studies. The AFM tip is modeled as an ideal hemisphere

and is considered to be rigid, meaning that all bonding and nonbonding interactions within the tip are eliminated by removing the associated elements and introducing a rigid coupling to a reference point. Preliminary simulations have shown, that this simplification has a negligible influence on the resulting elastic modulus given that the Hertz equation is modified accordingly. Usually, the Young's modulus of the sample is obtained by fitting the Hertz equation

$$D = \left(\frac{F}{\sqrt[2]{R} E_{tot}} \right)^{2/3} \tag{3.2}$$

to the simulated force-displacement data. In the above equation, D is the sample deformation, F is the indentation force, R denotes the AFM tip radius and E_{tot} is the reduced Young's modulus according to

$$\frac{1}{E_{tot}} = \frac{3}{4} \left(\frac{1 - \nu_{tip}^2}{E_{tip}} + \frac{1 - \nu^2}{E} \right). \tag{3.3}$$

Thereby, ν and E are the Poisson's ratio and the Young's modulus of the sample and ν_{tip} and E_{tip} are the Poisson's ratio and the Young's modulus of the AFM tip. If the AFM tip is rigid, E_{tip} becomes infinite and the first term in Eq. (3.3) approaches zero, reducing the Hertz equation to

$$D = \left(\frac{3F(1 - \nu^2)}{4\sqrt{R}E} \right)^{2/3}. \tag{3.4}$$

As a first step in the simulations, the equilibrium state of the system is obtained by relaxing the whole model including the AFM tip for a period of 50 to 100 ps, depending on the model size. The equilibrium position of the tip (in the sense of the AFM tip lying on the sample surface without any cantilever forces) adjusts itself automatically. Subsequently, the load is applied in terms of an AFM tip displacement of 0.5 to 1.5 nm, depending on the sample and tip size. To minimize the influence of strain rate effects, in preliminary simulations the loading time was increased until a convergence of the resulting Young's moduli was observed. A simulation time of 300 ps for the maximum displacement of 1.5 nm has proven to be suitable. The boundary conditions for both the equilibration and the loading are a mixture of rigid BCs and vacuum boundary conditions. The positions of all atoms in a border region of 0.2 nm are fixed, except for the top surface, where the AFM tip indents the material (see Fig. 3.4). To avoid an overestimation of the stiffness of the rigid boundaries, all angles and dihedrals, that contain at least two atoms in the boundary region, are removed from the model. The vacuum boundary conditions

on the top surface can be understood as free boundaries, at which no constraints are applied.

3.2.2 Results of Preliminary Simulations

As mentioned earlier, the numerical effort of MDFEM simulations (and MD simulations in general) prevents the simulation of real particle or AFM tip sizes in parametric studies. Thus, it is necessary to reduce the model size compared to the real material. The aim of the preliminary simulations discussed in this subsection is to analyze the influence of the AFM tip radius and the sample size on the calculated elastic modulus.

For all simulations presented here, the indentation direction is perpendicular to the boehmite layers (i.e. the [0,1,0]-direction). Firstly, the influence of the AFM tip radius on the elastic modulus of the boehmite is examined. Therefore, the tip radius is gradually increased from 1 nm to 5 nm in steps of 1 nm. The sample size, which is addressed afterward, is chosen to be four times the tip radius. It is shown to be large enough to not impose any boundary effects on the measured modulus later. The simulation results are shown in Fig. 3.5. With increasing tip radius, the resulting moduli converge against a Young's modulus of 136 GPa. Small tip radii lead to an underestimation of the moduli, but already for the 2 nm tip the deviation from the converged modulus is smaller than 4%. As a compromise between accuracy and efficiency, from here on the tip radius is chosen to be 2 nm for all following simulations. It is furthermore apparent, that the calculated values fall in between the values found in the literature and the experimental results presented above. The observed difference to the result of the quantum mechanics simulations reported by Tunega et al. [30] is quite small. However, to properly relate the simulation results to the literature values, the other spatial directions should be considered, as explained in section 3.2.3. The difference to the values from AFM experiments [33], in contrast, is large. The possible causes are investigated and explained later.

The influence of the sample size on the Young's modulus is addressed with a similar approach. Starting from a size of $8 \times 4.8 \times 8$ nm^3, the sample size is gradually reduced to a size of $5 \times 3 \times 5$ nm^3, keeping the aspect ratio constant. The tip size is fixed with 2 nm. Fig. 3.6 shows the resulting force-displacement curves. To avoid any confusions, it should be noted that for consistency reasons the deformation is plotted on the y-axis and the indentation force on the x-axis, as it is typically done AFM tests. The straight dashed lines indicate the onset of a deviation between the shown Hertz curve and the respective simulated curve, which is caused by boundary effects. At a certain indentation depth, the probe volume becomes influenced by the boundary conditions, indicating that the sample size is chosen too small. To avoid this, either the sample size has to be increased or the range in which the Hertz fit is calculated has to be truncated (here, the latter was already performed).

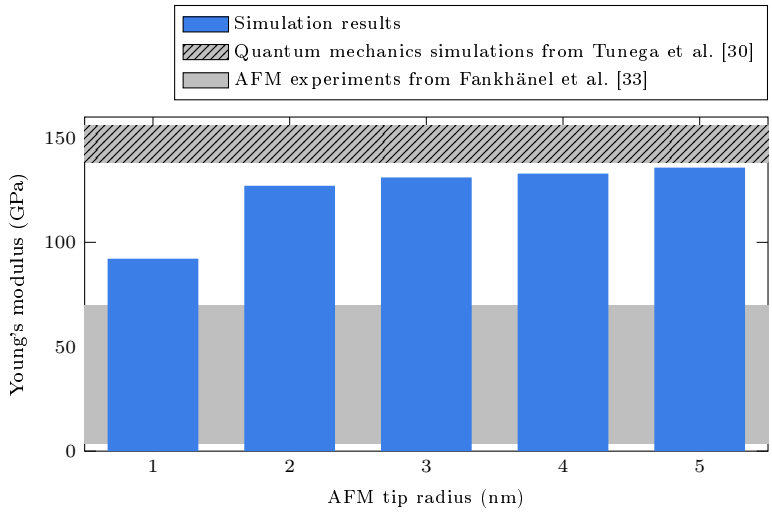

Figure 3.5: Influence of the AFM tip radius on the calculated Young's modulus of the perfect boehmite crystal. For comparison, results of quantum mechanics simulations from [30] and AFM experiments from [33] are shown.

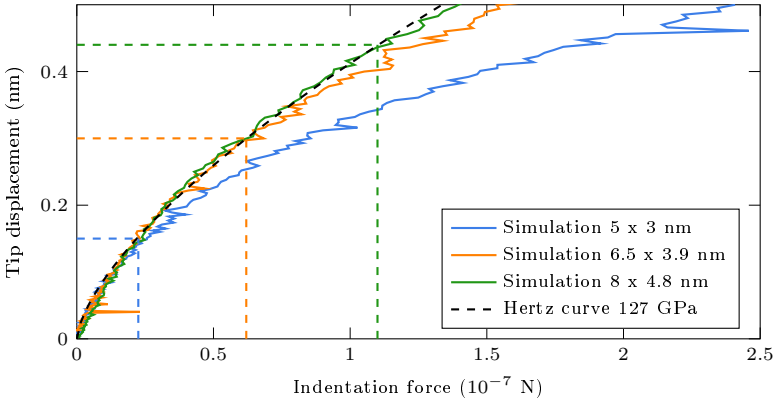

Figure 3.6: Influence of the sample size on the calculated FDC curves of the perfect boehmite crystal. Only data points left of the vertical dashed lines are considered in the fit.

As expected, Fig. 3.6 shows that the point at which the simulated curves start to deviate from the Hertz curve is shifted to lower deformations with decreasing sample size. Thereby, reducing the sample size from 8 to 6.5 nm and from 6.5 to 5 nm leads to an almost equal deformation shift of about 1.5 Å. To ensure reasonable results, a sufficiently large interval for the Hertz fit is required. Here, no real criterion for choosing the sample size is established but, as a conservative choice, the largest sample of $8 \times 4.8 \times 8$ nm^3 is used in the following.

3.2.3 Simulation Results

From the previous section, it can be concluded, that the Young's modulus of boehmite converges to a value of approximately 136 GPa and is calculated with a value of 127 GPa for a tip size of 2 nm, which is the reference model for all further investigations. Up to now, all simulations are performed in the [010]-direction perpendicular to the boehmite layers. This corresponds to the y-direction in Fig. 3.2. To account for the anisotropy of the boehmite crystal, additional simulations were performed in the [100]-direction (x-direction) and the [001]-direction (z-direction). These simulations result in Young's moduli of 232 GPa and 267 GPa, respectively. The in-plane moduli (x- and z-direction) are much higher than the out-of-plane modulus, while the modulus in the z-direction is slightly higher than in x-direction. The in-plane behavior is dominated by the crystalline lattice structure and hence by the chemical bonds between the atoms forming the layers. The out-of-plane behavior, in contrast, depends on the inter-layer nonbonding interactions, i.e. the hydrogen bonds connecting the boehmite sheets. Thus, the large difference between the in-plane and the out-of-plane behavior is expected. The comparison of the average Young's modulus of 212 GPa with the literature in the range of 138 - 156 GPa shows a reasonable agreement. It should be kept in mind, that quantum mechanics simulations use a very small excerpt (e.g. one unit cell) for the calculation of the mechanical properties. Furthermore, the estimation of an isotropic Young's modulus from the bulk modulus reported by Tunega et al. [30] and the averaging of the Young's modulus in the three spatial directions from the AFM simulations can lead to inaccuracies. Last but not least, the Morse potential, which was used for the nonbonding interactions, is not entirely symmetric, even for small deformations. The part, which describes the tensile behavior, is characterized by slightly lower forces than the compression part. Hence, the tensile modulus in the y-direction can be expected to be lower than the one under compression load.

So far, the Young's moduli obtained from the AFM simulations still exhibit large deviations from the experimental values presented in section 3.1, which amounted to approximately 11 GPa measured on the geological sample. To understand these results and to identify possible causes of the large differences, firstly, the influence of several imperfections is investigated. Since the [010]-direction resulted in the

softest behavior so far, the following simulations are only performed perpendicular to the boehmite layers. The first investigated imperfection is the intercalation of water molecules between the boehmite layers, as reported by Bokhimi et al. [28]. Therefore, 10% of the aluminum atoms on the inter-layer surfaces of the boehmite sample are assumed to be occupied by water molecules. The water molecules are connected through hydrogen bonds and replace the hydroxyl groups, which are normally bonded to the surface aluminum atoms. The intercalation of water leads to a slightly increased inter-layer spacing and thus to weaker nonbonding interactions between the layers. However, the reduction of the resulting Young's modulus is around 16%, leading to a value of approximately 113 GPa. Thus, the intercalation of water can clearly not explain the low stiffnesses measured in the experiments.

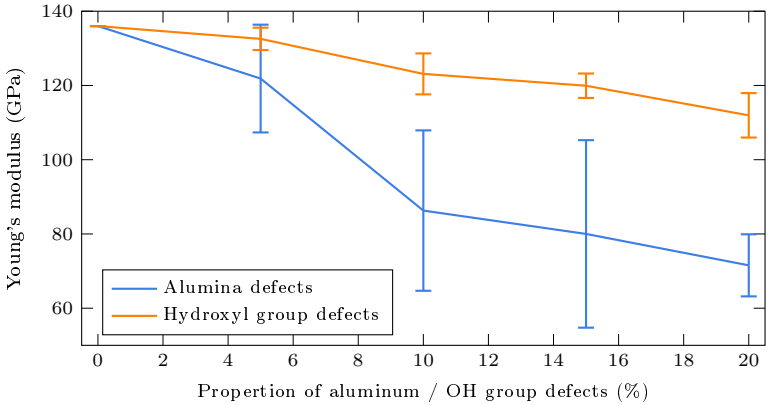

Figure 3.7: Influence of alumina/hydroxyl group defects on the calculated Young's modulus of boehmite.

As a second imperfection of the crystalline structure of boehmite, aluminum and hydroxyl group defects are examined. Therefore, random aluminum atoms or hydroxyl groups are deleted from the models. The amount of defects is varied from 0% to 20% in steps of 5%. For each case, three randomly generated models are simulated and the results are averaged. The results are shown in Fig. 3.7. Hydroxyl group defects lead to a rather small reduction of of the Young's modulus by a maximum of 18% for 20% deleted OH-groups. The softer behavior results mainly from the weaker interaction between the boehmite layers and from a reduced bending stiffness of the boehmite layers caused by the missing hydroxy bridges. In case of aluminum defects, the reduction is much more distinct. If 20% of the aluminum atoms are deleted, the Young's modulus amounts to 72 GPa, which is a reduction of 47%. The soft behavior is caused by voids in the octahedral crystalline structure, which result in a very disordered material, that reminds more of an amorphous, than a crystalline

structure. Both imperfection types still result in much higher Young's moduli than the experiments. In addition, significant amounts of defects, like the assumed 20%, are typically not observed in boehmite crystals in the literature. Hence, defects seem to be an unlikely explanation for the low stiffness measured in the experiments.

So far, the drastically lower Young's moduli from the experiments still cannot be explained. In section 3.1, the AFM measurements of the BNP/epoxy samples have been interpreted to feature major inelastic phenomena. These can include, in particular, a slippage of the crystal layers, but also cracking of layers and tilting of substructures. To further investigate the inelasticity from a numerical perspective, AFM simulations on boehmite particles embedded in an epoxy matrix are conducted. It should be noted that these simulations aim at improving the understanding of the effects leading to the soft experimental behavior rather than determining the elastic constants of boehmite. To do so, the particles are modeled with the real particle shape and a reduced primary particle size of 5 nm. To account for effects like layer slippage and tilting of the particle, different particle orientations are modeled, as shown in Fig. 3.9(a) - 3.9(c). Three different cases are considered. Firstly, the load is applied in [010]-direction perpendicular to the boehmite layers with a plane to plane support. This sample is used as a plausibility check and the resulting Young's modulus is expected to be equal to the one previously reported for the perfect boehmite structure. Secondly, the layers of the BNP are orientated diagonally, still with a plane to plane support of the particle at the bottom of the sample. In this case, the AFM tip can introduce a shear load to the particle and thus induce slippage of the layers. Thirdly, the layers are inclined as well, but the support is reduced to an edge to plane support, enabling an additional tilting of the particle. The matrix material embedding the BNP is intended to provide more natural boundary conditions to the particle and in this way enable inelastic deformations in the first place. The size of the sample perpendicular to the loading direction is chosen to be 15 nm based on preliminary simulations of the pure epoxy polymer (see section 5.1.3). The size in the loading direction depends on the particle orientation and is assigned in such a way, that the bottom boundary region is located directly below the BNP. This corresponds to a rigid surface supporting the particle, which can be regarded as an idealization of the sample holder from the experiment. It also ensures, that no polymer is located underneath the particle, which would lead to the measurement of a mixed modulus. For stability and performance reasons, the chemical bonds are modeled using harmonic potentials, which cannot reproduce the failure of bonds and hence a possible cracking of boehmite layers. However, due to the small extent of the boehmite sheets and the weak interlayer interactions, a cracking of layers is judged unlikely and this simplification should be acceptable.

The three cases have been exposed to a loading and a subsequent unloading, to check if the response is of elastic or inelastic nature. Fig. 3.8 shows the corresponding force-displacement curves and the respective Hertz curves. A huge difference between the configuration with loading perpendicular to the layers (blue) and the

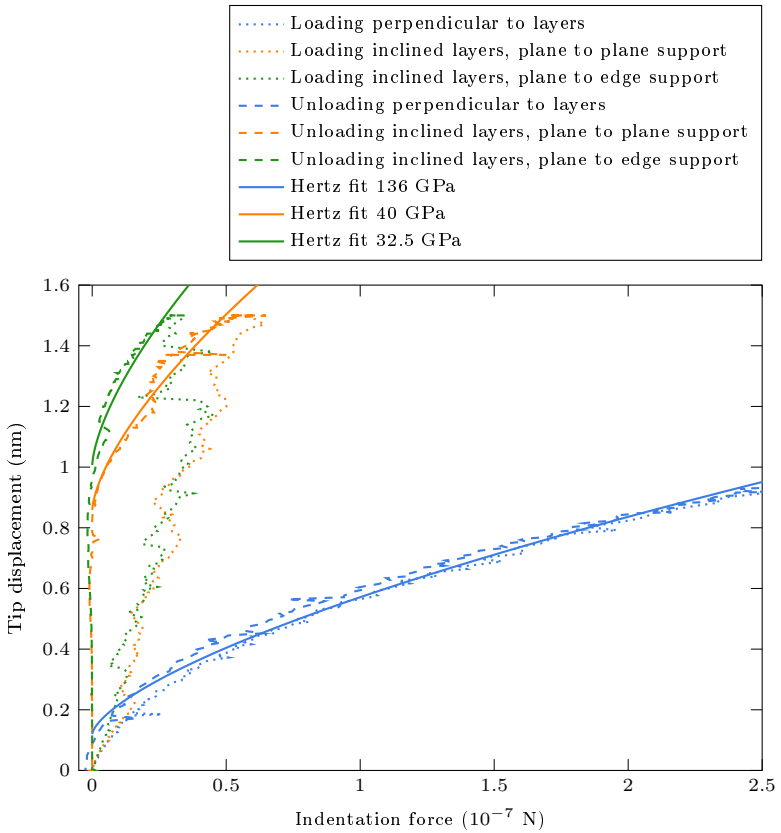

Figure 3.8: Loading-unloading curves and the corresponding Hertz fits of the investigated configurations from Fig. 3.9.

other two cases (orange and green) is apparent. The loading-unloading path for loading in [010]-direction are nearly identical with no considerable permanent deformation, indicating a purely elastic behavior with a resulting Young's modulus of 136 GPa. This is in good agreement with the results of the perfect crystalline structure from section 3.2.2. The other two cases show a drastic reduction of the slope of the loading curves. Furthermore, a significant permanent deformation is observed, as the unloading curves intersect with the y-axis at deformation values around 1 nm. This clearly indicates an inelastic behavior. The main mechanism leading to the reduced slope of the loading curves is a slippage of the crystal layers, that can be

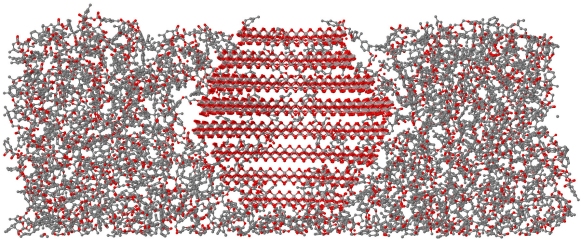

(a) Parallel layers with plane to plane support.

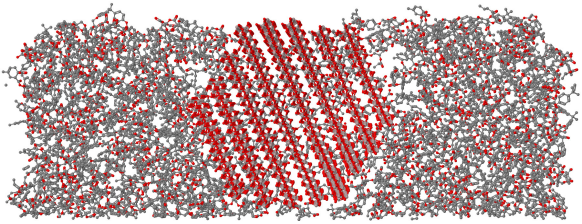

(b) Inclined layers with plane to plane support.

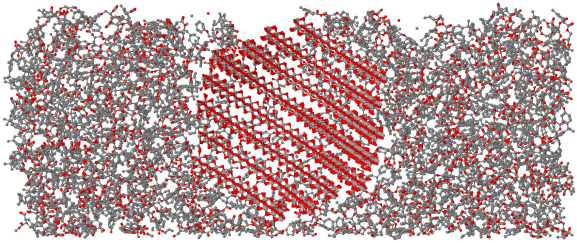

(c) Inclined layers with edge to plane support.

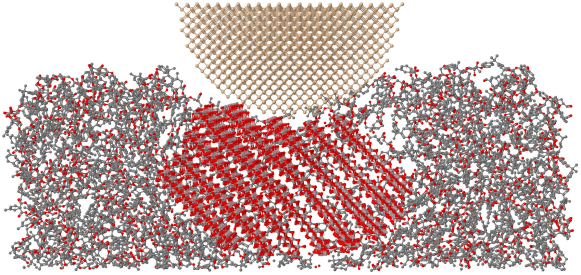

(d) Deformed configuration of inclined layers with plane to plane support at peak load

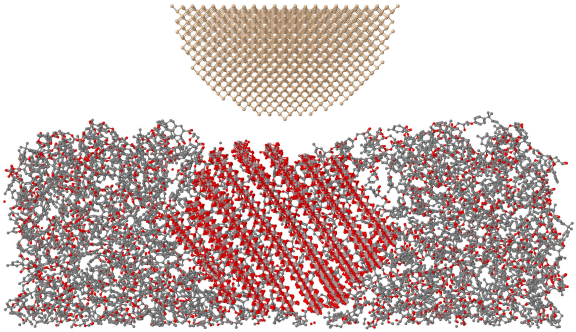

(e) Configuration after unloading of inclined layers with plane to plane support

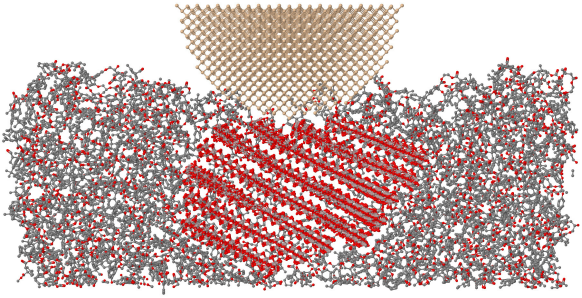

(f) Deformed configuration of inclined layers with edge to plane support at peak load

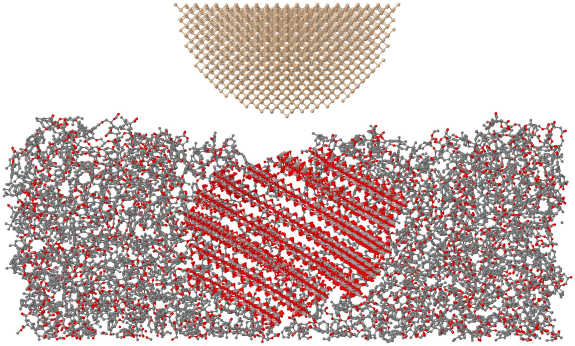

(g) Configuration after unloading of inclined layers with edge to plane support

Figure 3.9: Illustration of (a) - (c) the undeformed configuration of the investigated particle orientations, (d) - (e) the deformed configurations corresponding to the initially inclined layers with plane to plane support and (f) - (g) the deformed configurations corresponding to the initially inclined layers with edge to plane support.

seen in the deformed structure in Fig. 3.9 (d). The sudden onset of layer slippage is also expressed through the force jumps in the loading path in the force-displacement curves in Fig. 3.8. The visible roughness results from the snap from one equilibrium state of the inter-layer hydrogen bonds to the next one. Furthermore, even with the plane to plane support, a tilting of the boehmite layers is induced by the crystal layer slippage. The case with edge to plane support additionally allows for a tilting of the whole particle (see Fig. 3.8 (f)), resulting in an even lower slope of the loading curve.

To allow for a comparison with the experiments, the Young's moduli are determined by performing the Hertz fit on the unloading curves, as they are expected to reveal the elastic behavior. The resulting Young's moduli amount to 40 GPa for the plane to plane support and 32.5 GPa for the edge to plane support. These values show a significant reduction compared to the Young's moduli obtained from the perfect crystal structure and also a significant approach to the experimental values, leaving layer slippage as a probable explanation for the low stiffness. However, the deformed structure after unloading in Fig. 3.9 (e) reveals that the layer slippage is partly reversed during the unloading. This is caused by the restoring forces of the compressed matrix and by the adhesion between AFM tip and particle. Similar to the loading curve, the unloading path exhibits small jumps, which correspond to the reversed layer slippage. Hence, strictly speaking, performing the Hertz fit on the unloading curves is not permitted, as they are not purely elastic. Since here the goal is to explain the experimental behavior rather than predicting the elastic properties of boehmite, this fact is ignored. The simulated Young's moduli presented above are still around three times as stiff as the experiments conducted on the geological sample. These differences can be attributed to size effects in both the experiments and simulations and to limitations of the chosen simulation approach (e.g. concerning the chosen force field potentials). A detailed comparison of the experiments and simulations is presented in section 3.4.

3.3 Determination of the Interparticulate Force-Displacement Curves

In this section, the determination of the interparticulate interactions is discussed, which are the missing part for the simulation of the unfilled agglomerate unit cells in chapter 6. The basic idea is to simulate tensile, compression and shear tests of two randomly oriented particles. Thereby, the center of mass of one particle is fixed and the other one is displaced accordingly. A schematic illustration is shown in Fig. 3.10. It can be assumed that the resulting force-displacement curves strongly depend on the orientation of the two particles. To account for this, a statistically representative number of random cases is simulated. The resulting average force-

displacement curves can then be used in spring-like elements in the FE analysis on the microscale.

The so calibrated springs contain not only the interparticulate forces caused by the nonbonding interactions but also the deformation of the particles itself. It has previously been shown that the mechanical behavior of the primary particles is complex and strongly depends on the loading direction. This is on the one hand because the crystalline structure of boehmite and thus its mechanical behavior are orthotropic. On the other hand, it was found that the layered structure of boehmite adds additional inelastic deformation mechanisms. For example, under a compression load diagonal to the boehmite layers, layer slippage becomes the main deformation mechanism. A spring element, that represents such a material, demands for a direction-dependent behavior, or, more precisely, a spring behavior that takes into account the orientation of the particles it connects. However, here, another approach is pursued. As stated earlier, a statistically representative number of random orientations is simulated and the resulting force-displacement curves are averaged. The assumption, which will be used from here on and whose validity will be checked later, is that real agglomerates contain a large enough number of primary particles to allow for using the statistical mean of the force-displacement curves. In other words, the orientation of the primary particles in the microscale agglomerates will be neglected and all primary particles will interact with the mean force-displacement curve.

3.3.1 Model Generation and Simulation Aspects

The modeling and simulation procedure discussed in this section is based on the MDFEM [92], which is, again, due to the chronological development of the work presented in this thesis. It was previously discussed that the usage of an NVE ensemble with a temperature close to 0 K should still lead to a reasonable prediction of the elastic behavior of the crystalline material. Additionally, the disadvantage of the MDFEM of not offering PBCs in its current implementation is negligible here, since the determination of the interparticulate force-displacement curves does not rely on these BCs.

The generation of the boehmite particles is similar to the model generation from section 3.2.1. After the particles are created, the boehmite layers are made rigid by deleting all bonds, angles, dihedrals and nonbonding interactions within the layers and coupling the atoms to one reference point for each layer using a kinematic coupling. All physical interactions between the layers are retained in the model. This simplification should be valid, since, due to the high in-plane modulus, the deformation of the boehmite layers itself is negligible compared to the deformation between the layers, e.g. due to layer slippage. A reduced primary particle size of 3 nm is used from here on throughout the remaining thesis. Since these particles have an even number of boehmite layers, the boundary conditions are applied to the

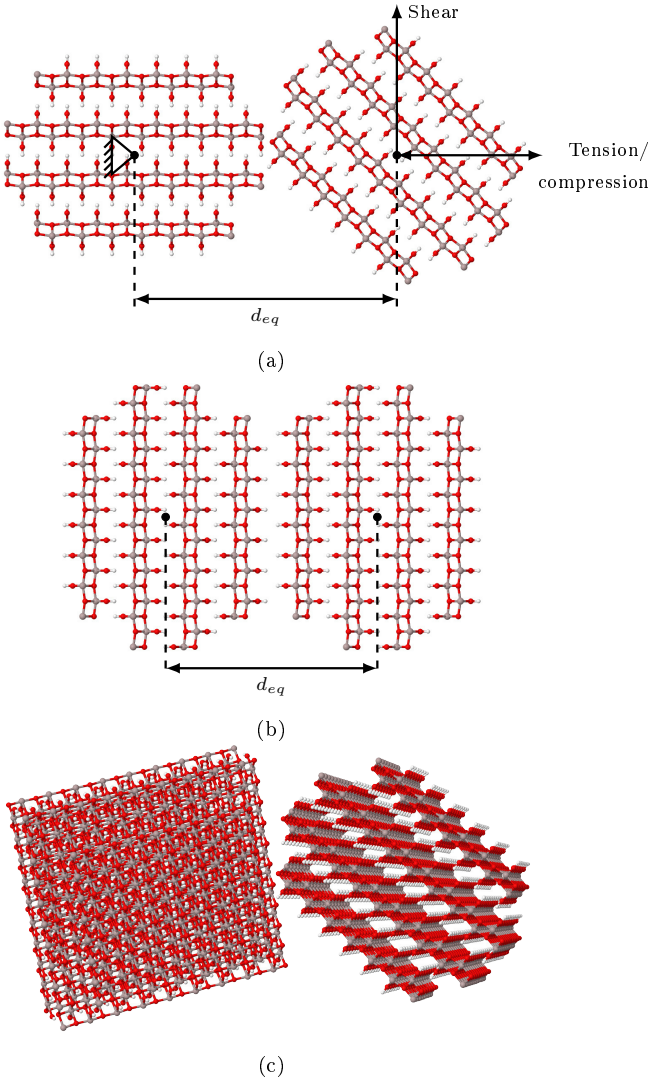

Figure 3.10: Illustration of (a) the principle idea of the determination of the interparticulate interactions for a model with relatively large equilibrium distance d_{eq} (schematic and 2D), (b) a 2D schematic model with the minimum d_{eq} and (c) an exemplary 3D model for the determination of the interparticulate interactions.

middle layer, which is closer to the center of mass of both particles. The first particle is added to the model with a random orientation. It is fixed in all translational and rotational degrees of freedom. Again, with a random orientation but with the same shape as the first one, the second particle is placed in such a way that both particles are close to their equilibrium distance. Its translational and rotational degrees of freedom are fixed as well, except for the loading direction.

All simulations are performed using the MDFEM in combination with the Dreiding force field [112]. The nonbonding interactions are modeled with the Morse potential with a cutoff of 15 Å, which is large enough to obtain the complete tension-compression and shear curves. After the model generation, the models are equilibrated for a period of 50 ps to find the equilibrium distance of the two particles. Subsequently, the load is applied with a constant velocity and a maximum displacement of 15 Å in a period of 500 ps for all loading cases. Previous parametric studies have shown that this loading velocity leads to converged results.

3.3.2 Simulation Results under Tensile and Compression Load

In this section, the results of the statistical simulations under tensile and compression load are presented. Fig. 3.11 (a) shows the corresponding force-displacement curves, which have been combined from the tension and compression simulations in the post-processing. The gray curves illustrate the results for 100 randomly generated samples and the blue curve is the mean force-displacement curve. These random models only differ by the relative angle between the two particles and their resulting equilibrium distance (compare Fig. 3.10 (a) and (b)). A significant scatter can be observed for the gray curves, e.g. concerning the maximum tensile forces, which range from close to 0 nN to around 18 nN. The cause for this scatter is the shape and the random orientation of the BNPs. It is comprehensible that the case, in which the particles touch corner to corner (compare Fig. 3.10 (a)), results in close to zero maximum tensile forces, whereas a plane to plane contact (compare Fig. 3.10 (b)) leads to the highest peaks visible in Fig. 3.11 (a). Even though the used approach generally includes the deformation of the primary particles, distinct deformations are not observed, which is because of the small forces arising from the interparticulate interactions.

As explained earlier, the mean force-displacement curve shown in blue in Fig. 3.11 (a) will be used in the FE analysis of the unfilled agglomerates. Hence, it is important to analyze the statistics of the simulated force-displacement curves. Strictly speaking, using the mean force-displacement curve is only valid for agglomerates consisting of more primary particles than the number of random cases, that is needed to obtain a converged solution from the statistical simulations presented above. To investigate this, the average maximum tensile force is chosen as a characteristic variable. Fig. 3.11 (b) shows its standard deviation in dependence on the number of

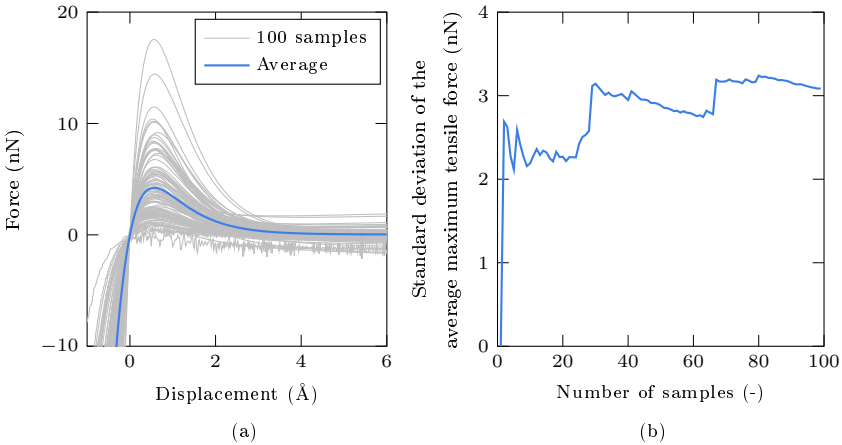

Figure 3.11: Numerical results of (a) the force-displacement curve under tension and compression load and (b) the influence of the number of samples on the average maximum tensile force.

random realizations. A sufficient convergence is reached for around 30 realizations. However, already for a small number of random samples, the error is reasonably small. With at least three randomly orientated particles, the maximum deviation from the converged average maximum tensile force is below 15%. In conclusion, the simulation of the average agglomerate size of 105 nm [95], which contains approximately 300 primary particles, using the mean force-displacement curve is feasible. Keeping the error in mind, in chapter 6, also smaller agglomerates with at least three particles are simulated.

3.3.3 Simulation Results under Shear Load

The resulting force-displacement curves of the statistical simulations under shear load are presented in Fig. 3.12. Thereby, the gray curves in Fig. 3.12 (a) show the result of the same 100 random realizations that were previously used and the blue curve is again the mean force-displacement curve. Fig. 3.12 (b) shows only the mean force-displacement curve with a different scaling of the y-axis scaling. It is noticeable that the force-displacement curves show large fluctuations. These fluctuations can be understood as a result of friction, precisely as oscillations resulting from the jumps of atoms from one equilibrium position to another. This idea is illustrated in Fig. 3.13, in which the extreme case of two parallel particle surfaces is presented. In the initial equilibrium position, the positions of the hydroxyl groups on the inner surface

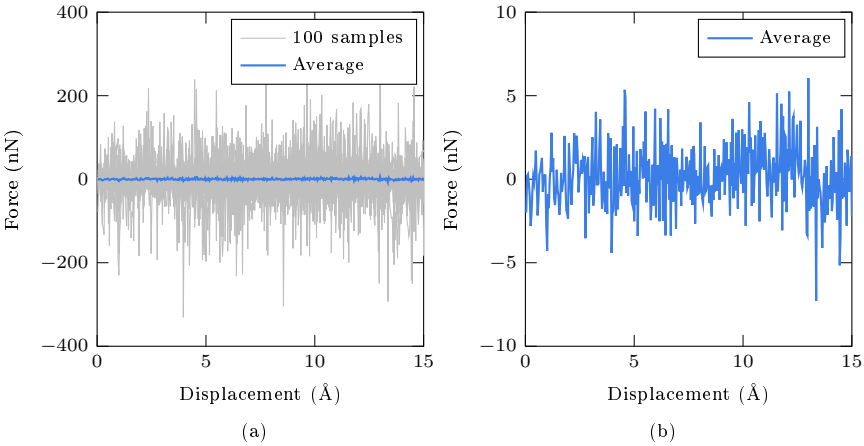

Figure 3.12: Force-displacement curve under shear load: (a) complete and (b) zoomed.

are offset and the layers are resting in an energy minimum. When a displacement d is applied to the top layer, the energy increases until the hydroxyl groups on the inner surface align. With further displacement the energy will reduce again, until the system reaches another equilibrium position, which is equivalent to the original one. This effect is responsible for the observed oscillations, though certainly more complex in case of the models containing randomly orientated particles. In these models, the probability of two parallel layers is small, but e.g. corner to plane contact situations are more likely, which can lead to complicated and seemingly random oscillations.

The fluctuations of the 100 random models are large with maximum amplitudes of almost 400 nN. However, the resulting average force-displacement curve shown in Fig. 3.12 (b) oscillates only with a maximum amplitude of around 5 nN. Moreover, the average curve fluctuates around a zero force. Thus, for the FE simulations in chapter 6, the force-displacement curves under shear load are neglected. In other words, a friction-free behavior is assumed and the spring elements only contain an axial behavior to represent the tensile and compression behavior.

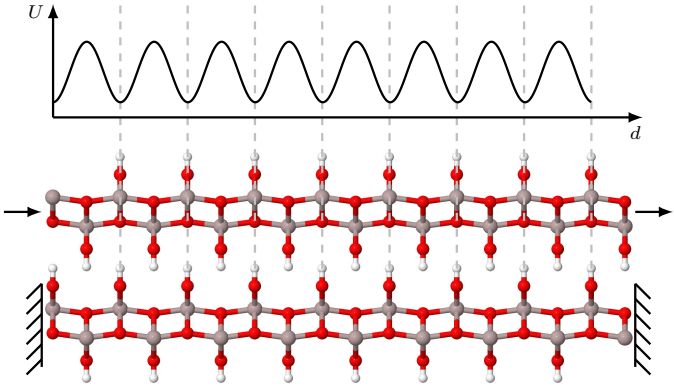

Figure 3.13: Schematic illustration of friction between two boehmite sheets.

3.3.4 Cumulative Distribution Function of the Equilibrium Distances

The inner structure or, in other words, the nearest-neighbor distribution of the real agglomerates has not been investigated experimentally. In fact, due to the small size of the primary particles, an experimental investigation, e.g. through transmission electron microscopy, is challenging. To allow for a more realistic modeling in chapter 6, the algorithm for generating the agglomerates needs to be calibrated. Therefore, the cumulative distribution function of the equilibrium distances

$$D_{eq}(d) = P(d_{eq} \leq d) \tag{3.5}$$

is used. In the above equation, d is the distance between two particles and d_{eq} are the equilibrium distances of the 100 random models, known from the equilibrium simulations (compare Fig. 3.10). The cumulative distribution function describes the probability of the equilibrium distance to be smaller than a certain value. Fig. 3.14 shows the results for the 100 random models investigated before. Due to the random orientation, the equilibrium distances show a quite large bandwidth with a minimum of 29.3 Å and a maximum of 42.4 Å. The goal for the model generation presented in chapter 6 is to reproduce the shown distribution as closely as possible.

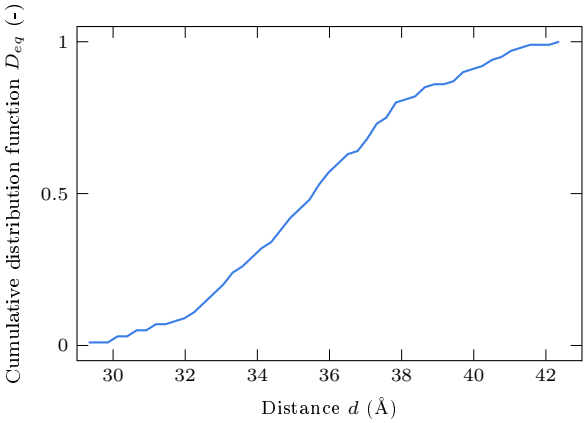

Figure 3.14: Cumulative distribution function of the equilibrium distances of the 100 random models.

3.4 Conclusions

The Young's modulus of boehmite, that can rarely be found in the literature, was suggested with values in the range of 120 to 160 GPa. MDFEM based AFM simulations on bulk boehmite yielded anisotropic Young's moduli of 232 GPa, 136 GPa and 267 GPa under load in [100]-, [010]- and [001]-direction, respectively. While these values are of similar magnitude compared to the literature values, experimental investigations indicated a far lower stiffness, as FDC measurements on a geological sample led to a Young's modulus of approximately 11 GPa. BNP/epoxy samples could only be measured by ADFS, which does not yet allow for an exact calculation of the Young's modulus. From the comparison to reference samples, the Young's modulus of the BNPs could be estimated to fall in between the stiffness of epoxy (3.3 GPa) and glass (70 GPa). In the following, the simulation results presented above are discussed in the context of the three hypotheses (sample size-related effects, inelastic layer slippage and the presence of amorphous boehmite) and united with the experimental findings.

The experimental measurements on the hydrothermally formed boehmite, which is known to feature a low crystallinity, resulted in a much lower stiffness than the other two samples. This leads to the conclusion, that the experiments on the geological sample and the BNP/epoxy sample are not critically affected by the presence of amorphous boehmite. This interpretation is supported by the simulation results

of imperfect crystalline structures, including aluminum atom and hydroxyl group defects and intercalated water molecules. In particular, the latter is observed in the real crystalline material. None of the considered defects could account for a sufficiently large drop in stiffness, to explain the low experimental values. However, it should not remain unmentioned that no real amorphous boehmite was simulated, since there is no sufficient description of its structure available in the literature. The numerical analysis of amorphous boehmite could lead to lower stiffnesses than the values presented above. Nevertheless, taking into account the experimental and numerical findings, the third hypothesis of a possible influence of the presence of amorphous boehmite is judged to be unlikely.

The second hypothesis, a possible layer slippage, is corroborated by simulations emulating the actual AFM test conditions of a particle embedded in epoxy resin. The simulations result in substantially lower Young's moduli compared to the perfect crystal, with values between 32.5 GPa and 40 GPa. The results fall within the range of 3.5 GPa to 70 GPa, provided by the experimental measurements on the BNP/epoxy samples. Thus it seems likely, that the stiffness mismatch in the experiments can be attributed to the slippage of crystalline layers under specific loading conditions. Furthermore, the simulations have shown that an imperfect contact of particle and sample holder further reduces the measured Young's moduli. It is indeed possible, that in the experiments the BNPs are partly pillowed by polymer instead of glass. Another similarity is that both the experiments and the simulations show the presence of a permanent deformation and thus indicate an inelastic behavior.

The measurements on the geological sample, in contrast, show no permanent deformation and an even lower Young's modulus. This substantiates the first hypothesis of size-related effects. It seems possible that in a macroscopic crystal the layer slippage is reversed by a conformation of the deformed areas to the far-field lattice structure after unloading. In the experiments as well as the simulations of the BNP/epoxy samples, the entire crystal is affected by the deformation and can, therefore, be both permanent or restored. Driving forces for restoring the original particle shape can e.g. be the adhesion between the AFM tip and the particle or the compressed epoxy underneath the particle. Concluding, the hypothesis of size-related effects is accepted as well.

Furthermore, the simulation models cannot be considered to be free of any size effects either. The presented AFM models are a downscaled version of the experiments on the BNP/epoxy samples and are substantially smaller than the experiments on the geological sample. Although the box size was chosen based on a preliminary study leading to converged results, it cannot be ruled out that for a significant enlargement of the simulation box additional phenomena like layer buckling become relevant. Other possible inaccuracies of the simulations may arise from the choice of the interatomic force field and the rigid representation of the AFM tip. These

effects can cause the remaining differences between the experiments on the geological sample and the simulations of the BNP/epoxy samples.

Besides providing a general insight into the material behavior of boehmite, this chapter aimed at calculating the elastic properties of boehmite as an input for the microscale simulations. Therefore, the orthotropic values obtained for the perfect boehmite crystal are used. This is justified as follows. The microscale simulations are carried out at small deformations using a purely elastic material model. Effects, like the detected layer slippage, are inelastic and hence require a much more complex treatment, which is from the authors' point of view not necessary. The layer slippage was observed when a shear load was directly applied to the BNP by the AFM tip. It can be assumed that in a NC sample under tensile or shear load in the elastic regime, the slippage of the boehmite sheets plays a minor role. This is because on the one hand, the load transfer to the BNPs is much weaker than in the AFM simulations and on the other hand because of the much smaller deformations. This assumption was verified in test simulations, in which NC UCs were strained up to 5% using the MDFEM. The comparison of the equilibrated and deformed state (see Fig. 3.15) reveals no considerable shear deformation of the NP. It can be concluded, that the inelastic effects of the BNPs do not considerably influence the elastic NC behavior, but only take effect in case of a more direct load transfer, under larger deformations or during failure.

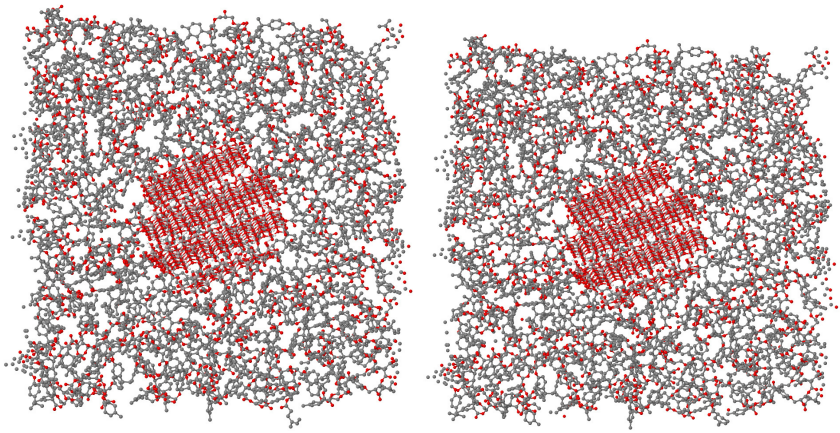

(a) (b)

Figure 3.15: Comparison of the (a) equilibrated and (b) deformed state ($\epsilon = 5\%$) of a NC UC consisting of a 3 nm BNP embedded in the epoxy matrix.

Furthermore, in this chapter, the characterization of the interparticulate interactions was presented. The force-displacement curves under tension, compression and shear load were analyzed and the statistics of these curves were discussed. It was shown that the force-displacement curves under tension and compression load converge for approximately 30 primary particles and that the error for agglomerates with less primary particles can be expected to be below 15%. The average force-displacement curve under shear load fluctuates around a zero force. Thus, for the FE simulations, the shear component is neglected and only an axial force-displacement behavior is modeled.

The results presented in this chapter were calculated with primary particle sizes between 3 and 5 nm. To enable an even more realistic modeling, in extension of the work presented here a coarse-graining of the BNPs could be established, which should allow for the simulation of the real primary particle size. Furthermore, the cumulative distribution function of the equilibrium distances of the primary particles used in this thesis is a provisional approach. To improve the modeling of the agglomerates presented in chapter 6, an experimental investigation of the nearest neighbor distribution should be established in future research.

4 Atomistic Scale: Epoxy

Polymers have been extensively studied in the literature, both from an experimental and numerical point of view. As stated in the introduction, the state of the art provides a solid foundation, but also some unanswered questions concerning the simulation of polymers using MD approaches. In this chapter, some of these issues are investigated through parametric studies and the authors' interpretation is given. To ultimately answer these questions is, however, not the purpose of this chapter, since it is a huge task that could fill a separate dissertation. The main focus here is to introduce modeling and simulation aspects of the epoxy polymer used throughout this thesis. These are the base for further studies, e.g. on the boehmite/epoxy interphase, as discussed in the following chapter. Of cause, also the elastic properties of epoxy are calculated as an input for the respective continuum material model for the microscale simulations in chapter 6. This is achieved by subjecting cubic epoxy simulation boxes (see Fig. 4.1) to a tensile load.

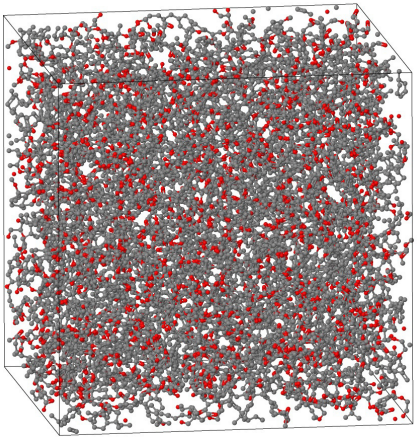

Figure 4.1: Exemplary epoxy simulation box.

4.1 Anhydride Cured Epoxy

The epoxy system used throughout this thesis is a bisphenol-A-diglycidylether with a degree of polymerization of 0.15 and a maximum chain length of $n = 1$ [106]. The polymer is cured with a 4-methyl-1,2-cyclohexanedicarboxylic anhydride agent and accelerated by a 1-methyl-imidazole accelerator. The chemical structures of all named molecules are shown in Fig. 4.2.

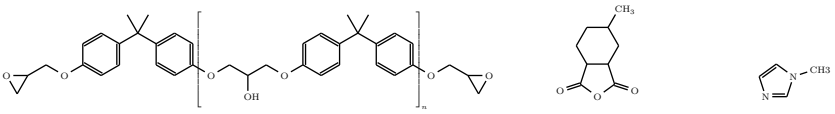

Figure 4.2: Molecular structures of (a) the bisphenol-A-diglycidylether monomer, (b) the 4-methyl-1,2-cyclohexanedicarboxylic anhydride curing agent and (c) the 1-methyl-imidazole accelerator.

The curing reactions of the present epoxy system are presented in Fig. 4.3. Primarily, an esterification occurs, which connects two epoxy monomers using an agent molecule, as shown in Fig. 4.3 (a) and Fig. 4.3 (b). To initiate the chemical reaction, the rings of the epoxy group and the agent molecule are opened, involving the accelerator. In the numerical modeling, this process is neglected and all rings are assumed to be initially open. Subsequently, the formed methyl group of the monomer connects to the resulting hydroxyl group of the agent molecule, as shown in Fig. 4.3 (a). The remaining reactive site of the epoxy group, which is a hydroxyl group, can

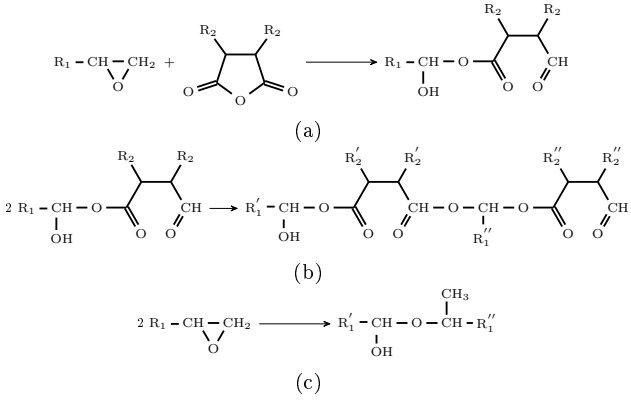

Figure 4.3: Curing reactions: esterification (a) and (b); etherification (c).

form a covalent bond to a methine group of a different agent molecule, as can be seen in Fig. 4.3 (b). Besides the esterification, a secondary reaction with a lower probability, the etherification, exists, as shown in Fig. 4.3 (c). It directly connects the hydroxyl group of a monomer to the methyl group of a different monomer.

4.2 Summary of the Experimental Characterization of Epoxy

Within the FOR2021 project, the epoxy was characterized by a variety of macroscopic testing, such as tensile tests, fracture toughness tests, dynamic mechanical analysis, thermogravimetric analysis and more. All of these tests were performed at the Institute of Adaptronics and Function Integration of the TU Braunschweig and the German Aerospace Center (DLR) in Braunschweig. For this thesis, only the isotropic elastic properties are of interest, which were reported by Jux et al. [95]. From tensile tests, the Young's modulus and the Poisson's ratio yielded values of 3.33 GPa and 0.39, respectively.

4.3 Model Generation and Simulation Aspects

It has been stated in the previous chapter that by switching from the molecular static MDFEM to a full-featured MD approach the methodology has undergone some non-negligible changes. In the same evolution step, the cross-linking approach implemented in the MolWizard was replaced by a more sophisticated dynamic one. In chapter 5, an AFM based approach for the investigation of the elastic interphase properties is presented, which is based on the MDFEM and the old cross-linking algorithm. Since it is an important contribution and thus included in this thesis, but not used in the multi-scale framework anymore, it has not been updated to the full-featured MD method and the new cross-linking approach. For the sake of completeness and clarity, both cross-linking approaches are introduced in the following.

The original approach, implemented in the MolWizard, can be understood as a purely geometrical algorithm and thus as a static realization of the cross-linking process. Firstly, the uncross-linked structure is generated. Therefore, random conformations of the epoxy monomers are randomly packed into the simulation box using Packmol [108]. The cross-linking is then performed similar to the work of Yarovsky and Evans [41] and Wu and Xu [42]. In two sequenced steps, the esters and ethers are created by randomly iterating over all hydroxyl groups and connecting them to the closest available methyl group within a specified cutoff radius. In case of the esters, this connection is established using a curing agent molecule, whereas the ethers directly connect hydroxyl groups and methyl groups of the monomers. The first step, the esterification, is thereby commonly performed using a smaller

cutoff radius than the etherification step. In the particular case presented here, the cutoff for the esterification and the etherification are chosen to be 10 Å and 12 Å based on parametric studies. As soon as all curing agent molecules are placed or no more reactive partners are found, the esterification is aborted and the etherification starts.

This approach has been replaced by a dynamic, simulative approach. Again, the first step is the generation of the uncross-linked structure. In addition to the monomers, also the curing agents are randomly packed into the simulation box. After a short equilibration, a cross-linking simulation is performed using LAMMPS [103], invoking in particular the implemented cross-linking method ("fix bond_create") in a slightly modified form. The general idea is similar to the static approach but as a dynamic realization. An MD simulation is performed, in which reactive sites coming closer than a specified maximum reaction distance are connected. The LAMMPS cross-linking method has been modified in such a way, that it prevents more than one connection between a molecule pair. This important to prevent the creation of unrealistic cross-links, like the one shown in Fig. 4.4. It shows two monomers, whose epoxy groups formed a double connection (green mark). In reality, only one connection is chemically feasible. Additionally, reactions between two reactive sites of the same molecule are excluded, to avoid for instance that the rings of the curing agent molecules are simply closed. Furthermore, a linear increase of the maximum reaction distance throughout the cross-linking simulation has been implemented, which leads to a smooth cross-linking over the cross-linking period and at the same time to high degrees of cross-linking.

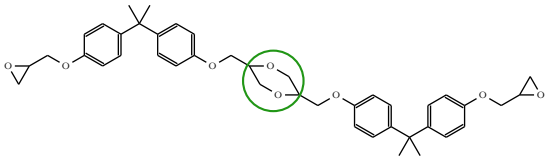

Figure 4.4: Example of an undesired connection between two epoxy monomers.

The cross-linking simulations are performed using the Dreiding force field [112] with a harmonic bond potential and a Lennard-Jones-(12,6) potential for the nonbonding interactions. The nonbonding cutoff is chosen to be 12 Å. A curing period of 1 ns with a time step of 1 fs and a relaxation period of 1 ps between the cross-linking steps is used. Standardly, an isothermal-isobaric ensemble (NPT) with a Nosé-Hoover barostat and thermostat [113] is applied. Since some of the interphase models in chapter 5 require a different thermostat, for comparison an isoenthalpic-isobaric ensemble (NPH) with an additional Langevin thermostat [114] is used. It should be noted, the latter on does not sample an exact physical ensemble, but produces comparable results to the Hoover NPT for large enough systems. To improve the

mixing of the molecules and to accelerate the curing process, the curing simulations are performed at a temperature of 500 K and a pressure of 1 atm. The reaction distances for the fully cured epoxy (i.e. a degree of curing[1] $> 90\%$) are chosen to linearly increase from 2.5 Å to 4.5 Å for the esterification and from 1.5 Å to 3.5 Å for the etherification. For lower degrees of curing, these distances are reduced, as explained in section 4.4.3.

The following simulation steps are performed with the same force field, potentials and ensembles as the curing simulations. After the cross-linking, the systems are cooled down and equilibrated for a period of 2.75 ns at a temperature of 300 K and a pressure of 1 atm. The loading simulations are performed at a temperature of 300 K with a standard strain rate of 10^7 1/s and a pressure of 1 atm in the transverse directions.

4.4 Numerical Characterization of Epoxy using Virtual Tensile Tests

4.4.1 Elastic Properties of the Reference Epoxy System

As a reference simulation throughout this thesis, an epoxy with a high degree of curing of approximately 92% is used. This is a typical assumption found in numerical studies in the literature [55, 56]. The exact consumption of all reactive groups as an average of three simulation boxes of 6 nm box size is shown in Tab. 4.1. The conversion of the reactive oxygen atoms of the monomers is slightly lower, which can be explained by a higher number of available hydroxyl groups, compared to the methyl groups. Even though the stoichiometric ratio is chosen in such a way that the system contains a similar amount of epoxy methyl groups and curing agents, with a value of 79%, the consumption of the curing agent molecules is lower than the conversion of the methyl groups. This is on the one hand caused by a small amount of etherifications in the system, which represent a share of approximately 7% of all cross-links. On the other hand, some curing agent molecules form only one bond, while the second reactive site is not connected.

For the calculation of the elastic properties, three randomly generated models are loaded in the three spatial directions. Hence, the elastic properties of nine simulations are averaged. Instead of solving Hooke's law from Eq. (2.9), by assuming an isotropic behavior, which is a valid assumption for the pure epoxy, the procedure can be simplified as follows. First, the Virial stresses and the box strains are calculated

[1] The term degree of curing describes the percent consumption of all methyl groups of the monomers (i.e. the reactive C atoms of the epoxy groups)

Table 4.1: Curing characteristics of the reference epoxy system (r_x: maximum reaction distance, Indices: $_{est}$: esterification, $_{eth}$: etherification).

r_{est} (Å)	2.5 - 4.5
r_{eth} (Å)	1.5 - 3.5
Consumption of curing agent C atoms (%)	78.87 ± 1.03
Consumption of curing agent O atoms (%)	78.57 ± 2.07
Consumption of epoxy C atoms (%)	91.78 ± 1.34
Consumption of epoxy O atoms (%)	85.66 ± 0.37
Absolute number of esters (-)	688.00 ± 13.49
Absolute number of ethers(-)	47.67 ± 3.40

according to Eq. (2.8) and Eq. (2.6). Therewith, the Young's modulus is calculated by fitting a straight (orange)

$$\sigma = E\epsilon + n \tag{4.1}$$

to the unfiltered stress-strain data (gray) in the loading direction, as shown in Fig. 4.5 (a). Afterwards, the resulting nine Young's moduli are averaged. The blue curve in Fig. 4.5 (a) is shown to ease the comprehensibility and represents a filtered stress-strain curve, where each point shows the average of the unfiltered data over a period of 50 fs. The Poisson's ratio is calculated using the relation

$$\nu = \frac{\epsilon_{tr,1} + \epsilon_{tr,2}}{2\epsilon_{long}}, \tag{4.2}$$

with ϵ_{long} being the strain in loading direction and $\epsilon_{tr,1}$ and $\epsilon_{tr,2}$ the strains in the two transverse directions.

The choice of the strain range for fitting the Young's modulus is thereby ambiguous. The typical values of 0.0005 - 0.0025 used in the experiments are too small or, in other words, the stress-strain data fluctuates too much to obtain reasonable Young's moduli. Hence, the range has to be increased. This should, however, be done with caution, since it can considerably influence the results, as can be seen from the comparison of Fig. 4.5 (a) and (b). The orange straight in Fig. 4.5 (a) was fitted in a strain range of 0.0001 - 0.001, whereas the interval for the fit of the green straight in Fig. 4.5 (b) was chosen to be 0.005 - 0.025. From these two cases, the elastic properties are calculated with values of $E = 6070 \pm 589$ MPa and $\nu = 0.324 \pm 0.047$ and $E = 5236 \pm 10$ MPa and $\nu = 0.326 \pm 0.007$, respectively. While the Poisson's ratios are in a good agreement, a considerable influence of the strain range on the

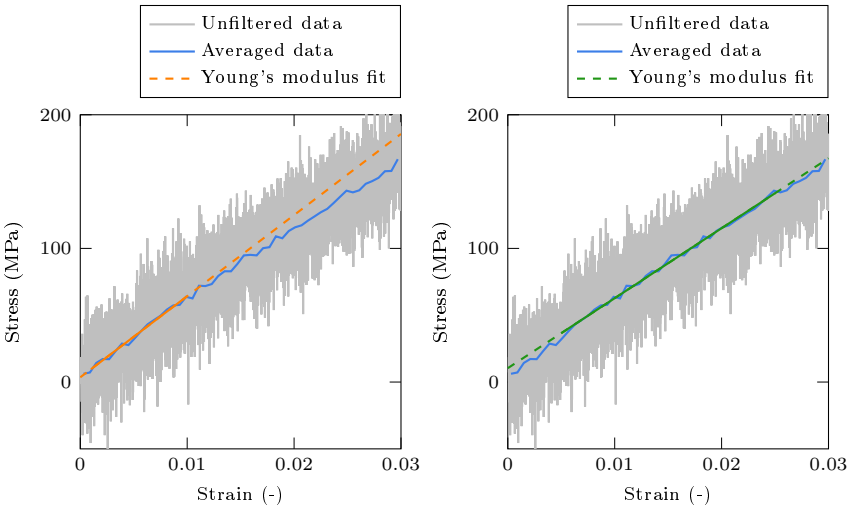

Figure 4.5: Stress-strain curve and linear fit of the reference epoxy system for a strain range of (a) 0.001 - 0.01 and (b) 0.005 - 0.025.

Young's modulus is observed. For the reference system, which is discussed here, the smaller strain range seems appropriate, since for larger strains a considerable nonlinearity is observed. However, for some of the cases investigated in the following, it can be seen that the smaller strain range leads to unreasonable results. These unrealistic values are caused by fluctuations of the stress-strain curves at small strains, which can result e.g. from a non-ideal equilibration of the systems. Hence, the results of both strain ranges are presented and compared in the following.

Generally, the calculated Young's moduli from both strain ranges overestimate the value measured in the experiment, which was reported to be 3370 MPa. In the following sections, possible causes for this deviation are addressed.

4.4.2 Influence of the Strain Rate on the Elastic Properties

The strain rate used in the simulations presented above was $\dot{\epsilon} = 10^7 1/s$, which is in the range of typically used values from the literature [56, 115]. This strain rate is significantly higher than the ones applied in quasi-static experiments. According to the test standard DIN EN 527-4, a loading velocity of 1 mm/min is used, which results in a strain rate of 1.67 10^{-4} 1/s for a test specimen with 100 mm free

length. Hence, a gap of 11 orders of magnitude between the experiments and the simulations is present, which cannot be closed, neither from the experimental nor from the numerical side.

In the literature, there is a disagreement about the existence of a strain rate effect on the elastic properties. Many numerical studies, like [54, 56, 115–117], ignore the large gap in strain rate between the experiments and simulations, and report a good agreement between both. However, it is often unclear, how these results were obtained. For instance, in some studies, the fit of the elastic properties is performed in a large strain range up to 3% or more, which has been shown to influence the resulting properties above. There are other studies, which do observe strain rate dependent elastic properties, like [58, 118]. These articles, similar to the present thesis, report significantly deviating elastic properties from MD simulations and experiments, which means considerably higher Young's moduli and lower Poisson's ratios. Other studies, like [55, 119], do not simulate varying strain rates but also report elastic properties that differ from experimental values, which could indicate strain rate effects. The same disagreement exists concerning the experimental characterization of the elastic properties of polymers, as e.g. [120–122] observe a strain rate dependency, but [123] does not. It can be concluded that the existence of an influence of the strain rate on the elastic behavior of polymers has not been completely understood in the literature.

Thus, a possible influence of the strain rate on the Young's modulus for the present epoxy system is discussed in the following. Three additional strain rates in the range of $\dot{\epsilon} = 10^6 - 10^9$ 1/s are simulated. Fig. 4.6 shows both the time averaged stress-strain curves and the resulting Young's moduli. Clearly, a strain rate dependent Young's modulus is observed for the evaluation in both strain ranges, as the values for the minimum strain rate of $\dot{\epsilon} = 10^6 1/s$ and the maximum one of $\dot{\epsilon} = 10^9 1/s$ differ by approximately 800 - 900 MPa. An explanation for this behavior could be that at lower strain rates the polymer network has more time to react to the deformation and to relax the resulting stress. As even the existence of a strain rate dependent Young's modulus of polymers is controversially discussed in the literature, there is no model available to describe a potential dependency. However, as illustrated by the logarithmic fit shown in Fig. 4.6 (b), it is imaginable that the gap between the experimentally and numerically obtained Young's moduli could be explained by the strain rate. Of course, an extrapolation over such a large range is prone to errors, and too little data is available from both the experiments and the simulations, to further elaborate on this relation in the scope of this thesis. Still, it can be concluded that the strain rate used in the MD simulations is one possible cause for the deviations between experiments and simulations.

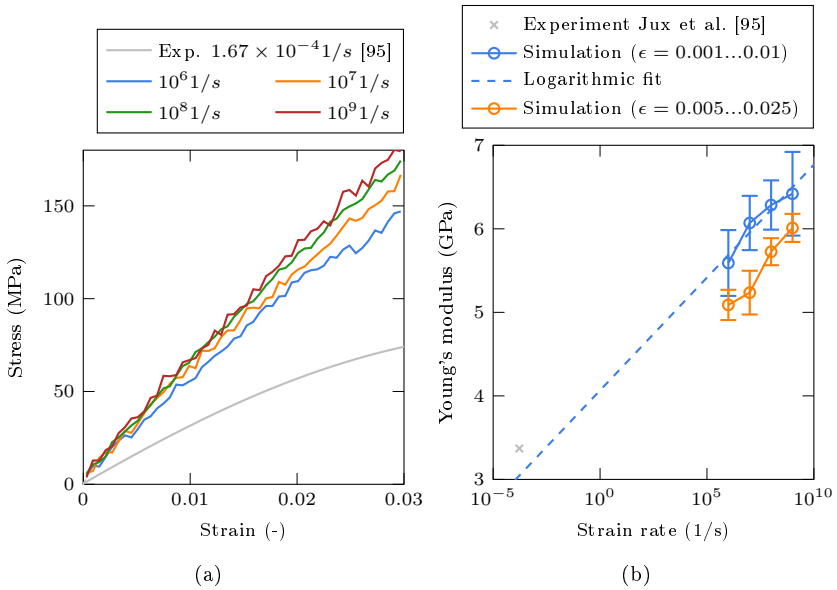

Figure 4.6: Numerical results of (a) the time averaged stress-strain curves of the reference epoxy system for different strain rates and (b) the dependence of the Young's modulus on the strain rate.

4.4.3 Influence of the Network Structure on the Elastic Properties

Another, by far more complex influence arises from the network structure of the epoxy. So far, a high degree of curing above 90% was assumed. However, there is no information about the absolute experimental degree of curing available. Thus, in the following, two reduced degrees of curing are generated and simulated, which will be denoted as "medium cross-linking" and "low cross-linking". To obtain these models, the maximum reaction distances in the curing simulations are reduced to the values shown in Tab. 4.2. Additionally, a reaction between two curing agent molecules according to the reaction schemes shown in Fig. 4.7 could be possible [124]. Thereby, the reaction shown in Fig. 4.7 (a) connects the methyl group of an epoxy monomer to the hydroxyl group of a curing agent, similar to the first esterification step from Fig. 4.3 (a). In Fig. 4.7 (b), however, the free methine group of the curing agent can bond to the hydroxyl group of another curing agent. This could theoretically lead to endlessly long hardener chains. In the curing simulations, the formation of hardener chains is assumed to have the same maximum reaction

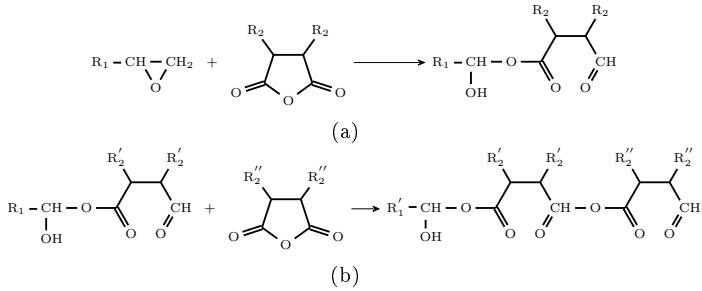

Figure 4.7: Reaction scheme for the formation of curing agent chains during the epoxy cross-linking.

distance as the epoxy esterification, which means that both reactions have an equal reactivity. The used maximum reaction distances for all alternative cases are shown in Tab. 4.2.

Tab. 4.2 additionally shows the curing characteristics of the three alternatively cross-linked systems. The two cases with reduced cross-linking essentially show a decrease in the conversion of all reactive sites as well as a decrease in the total number of cross-links created. The medium cross-linking results in a degree of curing of 87% and the low cross-linking in a degree of curing of 72%. The third case, which allows for the formation of curing agent chains is denoted as "hardener chains" from here on. In this case, the cross-linking of the epoxy monomers is significantly reduced, which can be read from the lower conversion of the reactive sites of the epoxy as well as the lower number of esters compared to the reference case from Tab. 4.1. The conversion of agent molecules, however, is significantly increased.

Table 4.2: Curing characteristics of the alternative epoxy systems (r_x: maximum reaction distance, Indices: $_{est}$: esterification, $_{eth}$: etherification).

	Medium cross-linking	Low cross-linking	Hardener chains
r_{est} (Å)	2.0 - 4.0	2.0 - 3.5	2.5 - 4.5
r_{eth} (Å)	1.0 - 3.0	1.0 - 2.5	1.5 - 2.5
Agent C atoms (%)	76.89 ± 0.49	68.57 ± 2.25	94.13 ± 0.66
Agent O atoms (%)	76.13 ± 0.43	70.40 ± 2.24	95.96 ± 0.88
Epoxy C atoms (%)	86.70 ± 1.06	72.22 ± 2.30	64.63 ± 1.88
Epoxy O atoms (%)	81.37 ± 0.37	65.43 ± 2.15	58.37 ± 2.37
Esters (-)	668.67 ± 1.70	607.33 ± 19.60	686.67 ± 8.73
Ethers(-)	36.67 ± 2.62	0.00 ± 0.00	0.00 ± 0.00

For the specific epoxy system investigated here, each epoxy group can be in three different states, as illustrated in Fig. 4.8. Firstly, it can have one connection, which is always a connection to the monomer the epoxy group belongs to. This can be interpreted as a dead end (see the blue mark in Fig. 4.8). Secondly, it can have two connections, of which one is always a connection to the monomer it belongs to and the other one is a connection to a curing agent molecule (ester) or another monomer (ether). This case can be understood as the formation of polymer chains, but is not a cross-link between two polymer chains (red mark in Fig. 4.8). Thirdly, the epoxy group can have three connections, one to its monomer and two esters or ethers. Only this case represents a cross-link between polymer chains (green mark in Fig. 4.8).

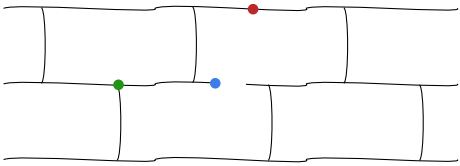

Figure 4.8: Schematic illustration of the different states an epoxy group can be in (blue mark: one bonded, red mark: two bonded and green mark: three bonded epoxy group).

Fig. 4.8 implies that not all epoxy groups contribute to the actual cross-linking. In other words, the chains between each cross-linking point can consist of more than one monomer or curing agent. Thereby, the length and composition of the chains between the cross-linking points are characteristic for the polymer network, even more than the degree of cross-linking. To illustrate that the polymer network structure is considerably affected in chosen alternative cross-linking cases, Fig. 4.9 shows the probability distribution of the number of monomers and curing agents between two cross-linking points.

The x-axis of each subplot in Fig. 4.9 reflects the number of curing agents between two cross-linking points and the y-axis the number of monomers between two cross-linking points. Thus, in the bottom left corner, the shortest chains can be found while moving towards the top right corner the chains get longer. A chain of zero monomers and zero curing agents if of course not possible, which is why it is always blank. The color of each marker indicates the count of the respective combination on a logarithmic scale. For all four cases, the majority of the chains consist of only one monomer or one curing agent, which are the shortest possible chains. However, the lower the degree of cross-linking is, the longer the chains get and the more the probabilities are extended diagonally towards the top right corner. For the lowest degree of curing (Fig. 4.9 (c)), around 30% of the chains have more than one hardener or monomer. In contrast, the highest degree of curing (Fig.

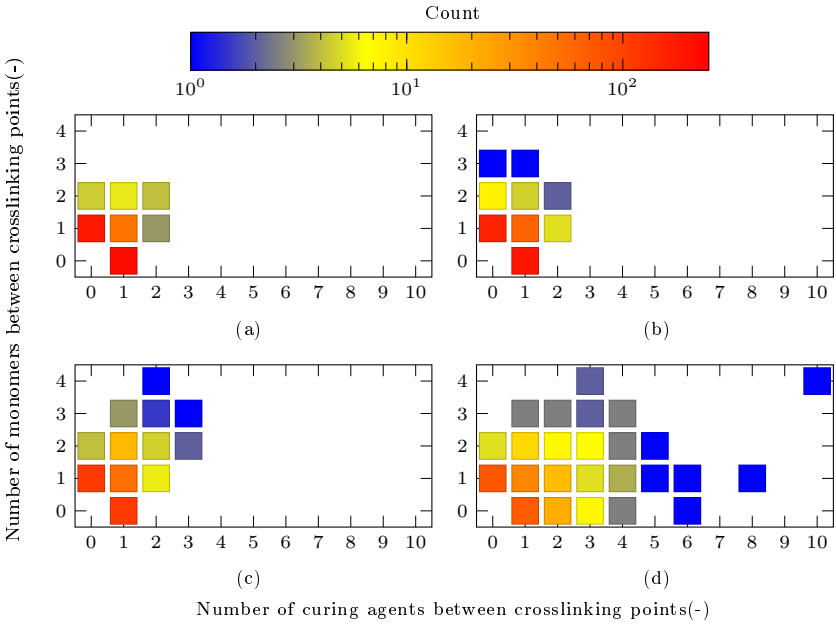

Figure 4.9: Probability of the number of monomers and curing agent molecules between each cross-linking point: (a) high cross-linking (reference), (b) medium cross-linking, (c) low cross-linking and (d) hardener chains.

4.9 (a)) has only 14% chains with more than one monomer or agent. It can be assumed that longer chains between the cross-linking points reduce the stiffness of the polymer network, which is indeed observed in the next paragraph. The option, which allows for the reaction of two curing agents (Fig. 4.9 (d)), shows even more distinct deviations. The probabilities are shifted more to the right than to the top, which is caused by the less strict rules for the formation of chains. If a reaction of two curing agents is possible, a chain could e.g. consist of m-a-a-m-a-a-m instead of m-a-m-a-m, assuming that m stands for monomers and a for curing agent. In total, around 50% of the chains between the cross-linking points have more than one monomer or one curing agent. One chain even extends up to ten agents and four monomers. Again, this should cause a reduction in the stiffness of the polymer network.

The influence of the network structure on the stress-strain curves and the Young's modulus is shown in Fig. 4.10. It compares the simulated Young's moduli of the four numerical cross-linking cases, as explained before, to the experiments with unknown

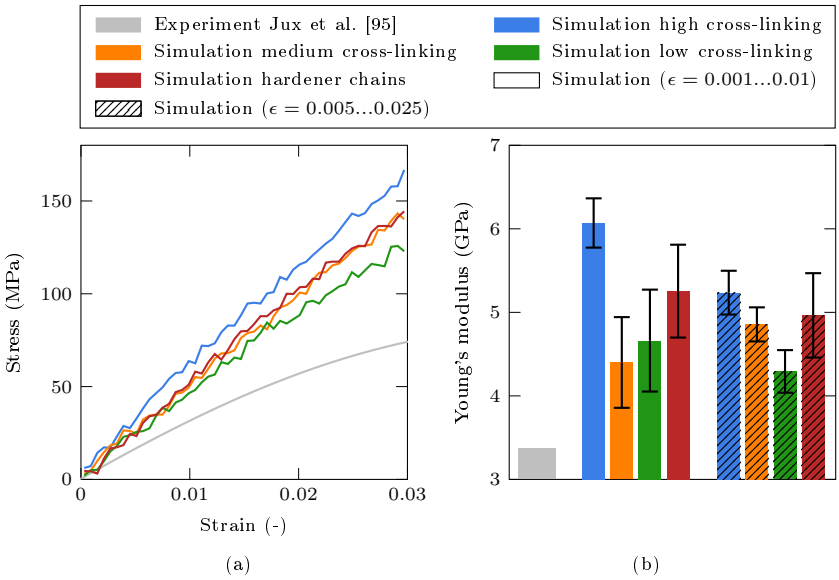

Figure 4.10: Numerical results of (a) the time averaged stress-strain curves of the differently cross-linked epoxy systems and (b) the corresponding Young's moduli.

degree of cross-linking. This example illustrates, that fitting the Young's modulus in a strain range of 0.001 - 0.01 can lead to a misinterpretation of the results, caused by the fluctuations of the curves at low strains. The fit in the higher strain range shows that a reduction of the degree of curing, as expected, leads to a gradual reduction of the Young's modulus. This trend is also visible looking at the stress-strain curves from Fig. 4.10 (a), but not for the fit in the low strain range from Fig. 4.10 (b). An overall reduction of around 1 GPa is observed comparing the reference case (high cross-linking) and the low cross-linking option. The case with enabled hardener chains results in a Young's modulus comparable to the medium cross-linking case. This is interesting because the hardener chain option has a much lower degree of curing (i.e. the conversion of the methyl groups). Thus, concluding from the degree of curing on the elastic properties, as it is typically done in the literature, is not always meaningful. In other words, the lowest degree of curing does not necessarily lead to the lowest elastic properties. It is important to additionally consider other parameters, like the conversion of curing agents or the total amount of created esters. Tab. 4.2 shows that the hardener chains case has the highest conversion of curing agents of all cases. Additionally, it's total amount of created esters is comparable to

the reference case with high cross-linking. These two parameters neutralize the low degree of cross-linking and cause the equivalent elastic properties of the hardener chains and medium cross-linking cases.

Concluding, the network morphology can significantly influence the elastic properties of the polymer. The Young's moduli calculated from the chosen example systems show a maximum deviation of approximately 1 GPa. Thus, the network structure can also contribute to the gap between the experimentally measured Young's moduli and the ones presented earlier in this chapter.

4.4.4 Influence of the Force Field on the Elastic Properties

The last influencing factor discussed here is the choice of selected force field parameters. Specifically, two alternative options are investigated. Firstly, some studies in the literature report that the usage of the Dreiding-X6 potential (Buckingham potential) instead of the Lennard-Jones potential for the nonbonding interactions can result in more realistic mechanical properties [56]. Secondly, in the Dreiding force field [112] it is not explicitly stated if the nonbonding interactions between the

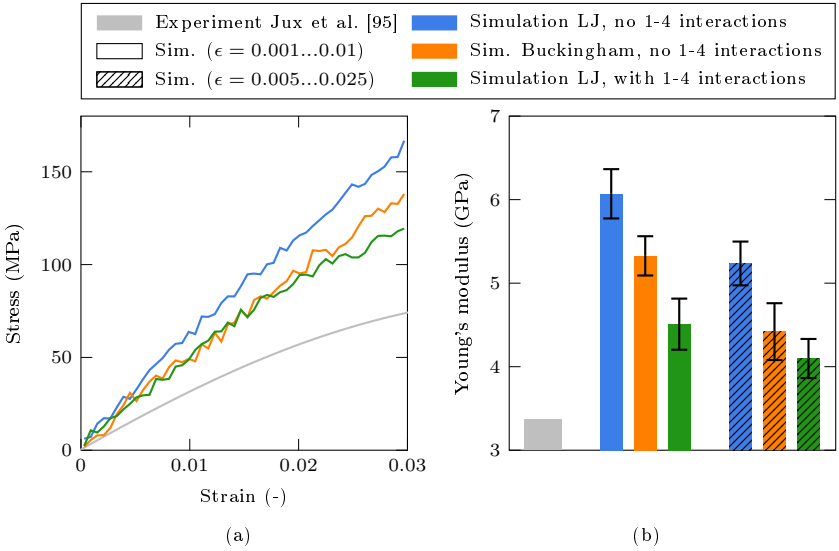

Figure 4.11: Numerical results of (a) the time averaged stress-strain curves obtained with the different force field options and (b) the corresponding Young's moduli.

first and fourth atom of a dihedral should be included or not. In all simulations presented until here, these interactions were excluded. Thus, to investigate their influence, in the following, they are enabled in LAMMPS. The results are shown in Fig. 4.11. With values of 5.33 GPa and 4.51 GPa calculated from the smaller strain range (0.0001 - 0.001), both cases lead to lower Young's moduli compared to the reference case. Hence, also the choice of the force field parameters can considerably influence the calculated elastic properties and thus the gap between the experimental and simulation results. In fact, the deviation between the reference case and the case with enabled 1-4-interactions is approximately 1.6 GPa, which is more than the maximum deviation of the different cross-linking cases.

4.4.5 Influence of the Thermostat on the Elastic Properties

As mentioned before, using the NPT ensemble with a Nosé-Hoover barostat and thermostat [113] for models consisting of different materials can lead to an unphysical behavior and wrong temperature profiles. An example is shown in section 5.2.1. To avoid this, an NPH ensemble with an additional Langevin thermostat [114] is used instead. Generally, if an NPH ensemble is combined with a thermostat, an

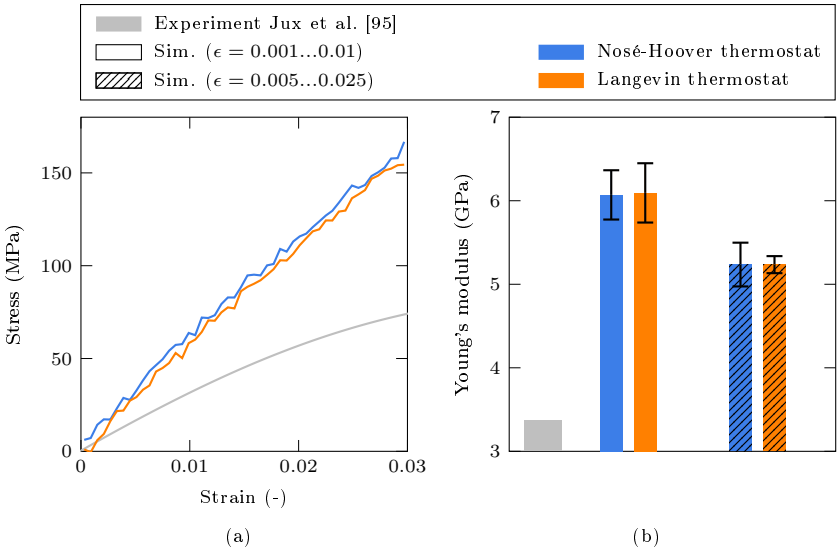

Figure 4.12: Numerical results of (a) the time averaged stress-strain curves obtained with different thermostats and (b) the corresponding Young's moduli.

NPT ensemble is obtained. Hence, the two cases only differ in the underlying thermostat formulation. Here, a comparison of both approaches is presented, to ensure compatible results and to justify this transition. Therefore the reference case from the above investigations is equilibrated and subsequently loaded using the NPH ensemble with an additional Langevin thermostat. The comparison of the results is shown in Fig. 4.12.

The NPT ensemble employing the Nosé-Hoover thermostat results in Young's moduli of 6.07 GPa and 5.24 GPa for the fitting in the strain ranges of 0.001 - 0.01 and 0.005 - 0.025, respectively. The NPH ensemble with the additional Langevin thermostat leads to values of 6.09 GPa and 5.24 GPa. Both cases show an outstanding agreement. Thus, the usage of the Langevin thermostat in the following chapter is feasible.

4.4.6 Verification of the Approach for the Calculation of the Local Elastic Properties

In order to verify the new approach for calculating the local elastic properties from MD simulations presented in section 2.2.1, the reference epoxy from section 4.4.1 is reconsidered. To ease the comprehensibility, from here on the new approach is denoted as the "local approach", whereas the combination of the Virial stress and the box strain is called the "classical approach". The goal of this section is to show the equivalence of both approaches for a box of pure polymer. It was stated before that the classical approach can only deliver the elastic properties globally for the whole simulation box. To be able to compare both approaches, instead of dividing the models into several subsections, the local approach is performed for only one section, which is equal to the whole simulation box. In other words, for verification purposes, the local approach is not used to calculate local elastic properties in this section, but the global ones. The calculation of the local interphase properties, for which the local approach is designed, is demonstrated in the following chapter.

Firstly, a reasonable value for the interaction radius has to be identified. Therefore, the strain of the simulation box is calculated using Eq. (2.14) with increasing r_{inter} and compared to the classical strain definition calculated from Eq. (2.6). The criterion for choosing the interaction radius is a converged strain value and a good agreement between the two strain measures of the local and the classical approach. Fig. 4.13 shows the comparison of both strains. It can be seen that this criterion is fulfilled for sufficiently large values of r_{inter}. From here on, the interaction radius is chosen to be 6.5 Å for all further simulations, including the investigation of the interphase in the following chapter.

The comparison of the stress-strain behavior of the local and the classical approach for the reference epoxy simulation box is plotted in Fig. 4.14. The shown gray curve

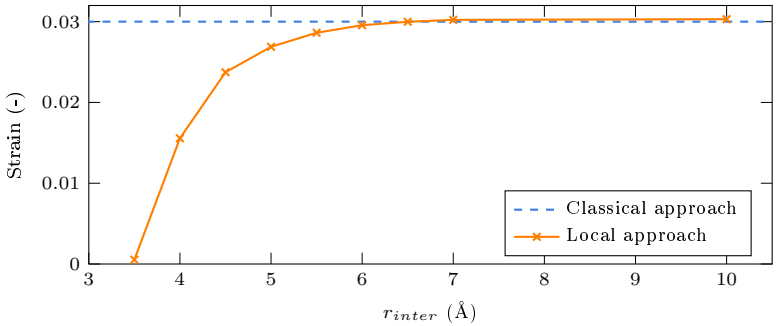

Figure 4.13: Dependence of the strain calculated using Eq. (2.14) on the interaction radius r_{inter}.

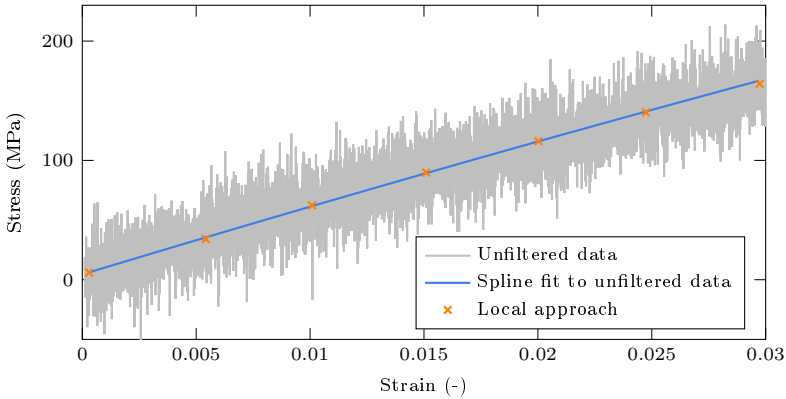

Figure 4.14: Comparison of the stress-strain curve calculated using Virial stress and box strain and using the local approach presented in section 2.2.1.

is the unfiltered stress-strain data, as previously shown in Fig. 4.5. The blue curve is intended to ease the comparison between the two approaches and represents a spline fit to the unfiltered data. The orange markers show the stresses and strains calculated using the local approach (Eq. (2.10) and Eq. (2.14)). Thereby, each point represents one deformed configuration. Again, the region R is chosen to be equal to the whole simulation box and the results are averaged for three randomly generated simulation boxes and the three spatial directions. Fig. 4.14 shows that both approaches agree outstandingly for all deformed configurations. Furthermore, it can be seen that also the non-linearity of the original data and of the spline fit can be

reproduced by using multiple deformed configurations. Hence, as promised earlier, the local approach is not limited to the calculation of the local elastic properties, but is also capable of capturing inelastic phenomena.

In case of the local approach, the stiffness is calculated from the stresses and strains in the reference state and the deformed configuration at a strain of 0.01. Assuming an isotropic behavior, the Young's modulus yields

$$E_{loc} = \frac{\sigma^{def} - \sigma^{ref}}{\epsilon^{def} - \epsilon^{ref}}. \tag{4.3}$$

The Poisson's ratio is calculated similarly to the classical approach using Eq. (4.2).

Tab. 4.3 provides an overview of the resulting elastic properties. Both approaches agree outstandingly, with a slightly higher stiffness, but a lower Poisson's ratio in case of the local approach. It can be concluded that the local approach is capable of calculating the correct response for the reference epoxy. Hence, in the following chapter, it will be applied to the characterization of the elastic interphase properties of the boehmite/epoxy interphase.

Table 4.3: Comparison of the elastic properties from the classical and the local approach.

	Classical approach	Local approach
Young's modulus E (MPa)	6070 ± 589	6174 ± 481
Shear modulus G (MPa)	2293 ± 281	2367 ± 203
Poisson's ratio ν (-)	0.324 ± 0.047	0.305 ± 0.011

4.5 Conclusions

In this chapter, details of the generation, simulation and ultimately the results of the pure epoxy simulations were discussed. The elastic properties of the reference system (i.e. for instance a high degree of curing above 90%, a strain rate of $\dot{\epsilon} = 10^7 1/s$ and a Lennard-Jones potential for the nonbonding interactions) yielded in a Young's modulus of 6.07 GPa and a Poisson's ratio of 0.324. The experimentally measured values are $E = 3.37$ GPa and $\nu = 0.39$. The cause of the resulting large deviations was addressed by performing parametric studies at different strain rates, with different cross-linking assumptions and different force field options.

It has been shown that all the investigated parameters and cases considerably influence the calculated elastic properties. It seems feasible to find combinations of these parameters, with which the experimental results can be reproduced. However, with the given validation possibilities it is impossible to determine the correct set of parameters. As discussed earlier, the literature is divided, as many studies report a good agreement between the numerical and experimental results and others show large differences. All of these studies have in common that the reason for the matching or deviating behavior remains unclear. From the authors' point of view, it is pointless to adjust the previously investigated (or possible additional) parameters until a good agreement between the numerical and the experimental results is reached since it is safe to assume that many possible combinations exist. Which one is the correct one? For the rest of this thesis, the properties and parameters of the reference case are used, since they reflect the original assumptions concerning the network morphology, which were made based on information from the manufacturer [106] and decided upon together with some of the project partners in the FOR2021 project. Based on the available experimental insights and the expertise of the coworkers, these assumptions should provide the most realistic description of the polymer network structure. Furthermore, it was shown that the deviations between the experimental and numerical results are not necessarily connected to the network structure, but could be attributed to the high strain rates used in the numerical simulations.

The previous discussion is often concealed in the literature. Future research should focus on disarticulating this complex topic and aim at establishing better validation possibilities, e.g. of the network morphology. First attempts in this field were made by Unger et al. [125], who compared the reaction kinetics from MD simulations to near-infrared spectroscopy results. This method, which provides an indirect validation of the network structure, is, however, not applicable for the present epoxy system, since it cannot distinguish between the reactive sites (e.g. hydroxyl groups) of the monomer and curing agent used in the present thesis.

Furthermore, in this chapter, the newly developed approach for calculating the local elastic properties from MD simulations was verified for the pure epoxy. Since an outstanding agreement with the classical approach using the Virial stress and the box strain was observed, the local approach will be used in the following chapter for the investigation of the local elastic interphase properties.

5 Atomistic Scale: Boehmite-Epoxy Interphase

An interphase is a newly created phase, which can develop at the boundary of adjacent spatial regions of different matter. Thereby, it should be distinguished between the terms interface and interphase. An interface is the boundary of the two phases, in other words, the two-dimensional contact area of the regions of different matter. The interphase, in contrast, has a thickness and hence a three-dimensional extent. The reasons for the development of an interphase are versatile. In the present case of a boehmite/epoxy material combination, the interphase can only be found in the amorphous polymer region. The crystalline structure of boehmite does not show any considerable interphase effects. In particular, the BNP/epoxy interphase is caused by two effects. Firstly, the physical interactions between boehmite and epoxy lead to repulsive forces and a shift of polymer away from the interface. Secondly, the BNPs can interfere with the epoxy cross-linking and thus affect the polymer network structure. The mechanism behind this and the influence on the elastic interphase properties are discussed in this chapter.

To obtain the elastic properties of the interphase, two different approaches are investigated: An AFM simulation-based approach and the new method for the calculation of the local elastic properties from MD simulations, as described in section 2.2.1. As explained when the idea of simulating AFM was introduced in chapter 3, these simulations rely on the molecular static implementation of the MDFEM. The implications of this approach have already been discussed. Again, from the authors' point of view, the presented AFM simulations should be updated to a full-featured MD approach, including the dynamic cross-linking, as discussed in section 4.3. This is of significant importance for polymer simulations, in which the lack of a correct representation of the temperature can considerably influence the results. The AFM simulation-based approach for characterizing the BNP/epoxy interphase is an important contribution and is hence comprised in this thesis. However, it is no longer used in the multi-scale framework and has thus not been updated. This fact should be kept in mind while reading this chapter, especially when it comes to the transferability of the results obtained with the two approaches.

As stated in the introduction, a direct experimental measurement of the elastic properties of the BNP/epoxy interphase was not reported in the literature. Also in the scope of the FOR2021 project, this goal could not be reached, which is why a summary of the experimental results, as is was presented in the previous chapters, is not shown here.

5.1 Numerical Characterization of the Interphase using AFM Simulations

5.1.1 Modeling and Simulation Aspects

The generation of the simulation models is in large parts based on the model generation presented in the previous chapters. Specifically, the general idea of simulating AFM and the generation of the crystalline structure of boehmite are shown in section 3.2.1 and the epoxy cross-linking is explained in section 4.3. For the AFM simulations presented in this chapter, the old non-simulative epoxy cross-linking approach implemented in the MolWizard is used. In the following, only differences to what was discussed earlier are described.

The main difference in the generation of the chemical structure is that the boehmite surface hydroxyl groups can join the epoxy cross-linking reaction (see section 4.1, Fig. 4.3). To illustrate this, Fig. 5.1 highlights all reactive hydroxyl groups of the whole system with green marks. The boehmite hydroxyl groups highlighted in Fig. 5.1 (a) can behave similarly to the ones of the agent molecules, highlighted in Fig. 5.1 (c). Thereby, the reactivity of the different (i.e. boehmite (Fig. 5.1 (a)), epoxy (Fig. 5.1 (b)) and curing agent (Fig. 5.1 (c))) hydroxyl groups is experimentally unknown and subject of the investigations presented in this chapter. Surface modifications, which are typically applied to influence the chemical interaction between NPs and polymer, are not modeled explicitly. With this simplification, the effort of the model generation is reduced. Furthermore, for many surface modifications, the exact reaction mechanisms and the resulting long-range effects on the polymer network are experimentally unknown as well. Instead, in this thesis, the reactivity of the boehmite surface hydroxyl groups is varied (see also section 5.2.1). For the old cross-linking approach implemented in the MolWizard, the number of cross-links created between boehmite and epoxy can be specified directly. In the following AFM simulations, three cases are compared, which are denoted as no chemical bonding (between boehmite and epoxy), medium chemical bonding (corresponds to 15% of the surface hydroxyl groups of boehmite being bonded to the epoxy) and strong chemical bonding (corresponds to 25% of the surface hydroxyl groups being bonded to the epoxy).

To create the AFM models for the characterization of the interphase, simulation boxes containing a 3 nm BNP at a low weight fraction of 1% are generated. These models are cut in the middle, so that the particle is cut in half, to make the interphase accessible. Subsequently, the AFM tip is generated and added to the model, as described in section 3.2.1. The whole model is then equilibrated for a period of 150 ps at a time step of 1 fs. Afterward, the AFM tip is shifted to the desired measuring point. To save computational time, the model is further reduced by cutting out the cubic part under the AFM tip, as indicated by the dashed orange

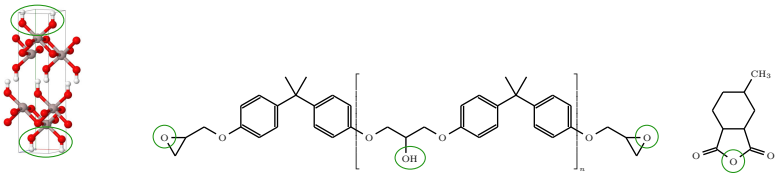

Figure 5.1: Chemical structures of (a) the unit cell of boehmite, (b) the molecular structure of the epoxy monomer and (c) the molecular structure of the curing agent. The green marks highlight all reactive hydroxyl groups.

lines in Fig. 5.2. The size of the cutout is determined by parametric studies, which are presented in section 5.1.3. After reducing the model, another relaxation of 100 ps is performed, before the AFM tip displacement of 1 nm in a period of 300 ps at a time step of 1 fs is applied.

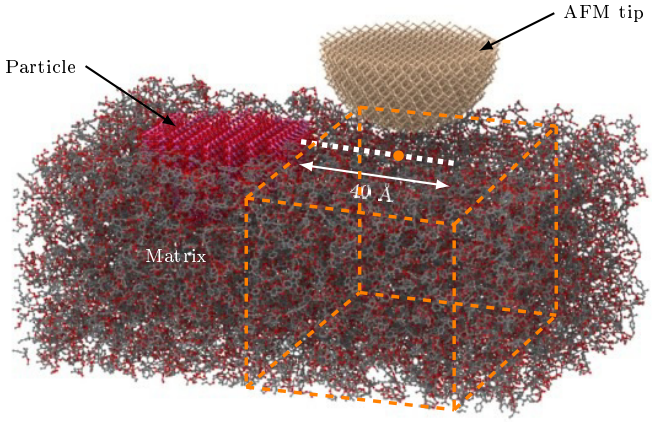

Figure 5.2: Schematic illustration of the AFM measuring points and the reduction of the simulation box.

5.1.2 Characteristics of the Interphase Network Structure

Before the elastic properties are presented, the influence of the interfacial bonding on the interphase morphology of the polymer is discussed. Therefore, Fig. 5.4

provides insight into the characteristics of the interphase network structure. The profiles of four characteristic variables are shown: the mass density, the epoxy cross-link density (i.e. the number of cross-links per unit volume excluding connections between boehmite and epoxy), the total cross-link density (including connections between boehmite and epoxy) and the amount of curing agent molecules per unit volume. The shown profiles are obtained by slicing the simulation models into spherical shells around the particle center of mass (see Fig. 5.3), calculating each of the characteristic variables and normalizing it with respect to the volume of the spherical shell. The characteristic variables are then plotted against the distance to the particle center of mass. The two extreme cases, which are the case without chemical bonding between the BNP and the epoxy (blue in Fig. 5.4) and the case with strong chemical bonding (orange in Fig. 5.4) are compared to the values of the bulk epoxy material (gray in Fig. 5.4), which was calculated from the pure epoxy models from the previous chapter. The vertical dashed lines in Fig. 5.4 indicate the phase boundaries of boehmite and the interphase. How the interphase boundaries are defined is explained in the following paragraphs. Using spherical shells for a not exactly spherical particle (see Fig. 5.3) leads to a certain smearing of the characteristic variables close to the BNP surface. This makes an exact definition of the boehmite boundary difficult. As compromise between all profiles shown in Fig. 5.4, the boundary of the BNP is assumed to be located at a distance of 17 Å from the particle center of mass. As explained earlier, the results shown here are no

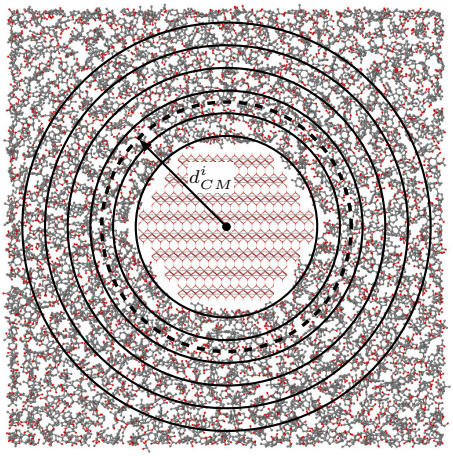

Figure 5.3: Schematic illustration of the calculation of the characteristic variables plotted in Fig. 5.4 (d^i_{CM} describes the mid-interval distance of slice i from the particle center of mass).

longer used in the multi-scale framework. Thus, this uncertainty is accepted for the following explanation of the network morphology.

The mass density profiles are shown in Fig. 5.4 (a). The boundary of the boehmite region can clearly be identified, as both density profiles exhibit a sudden drop of the density at around 18 Å away from the particle center of mass. It does not exactly coincide with the defined boehmite boundary because of the previously mentioned smearing due to using spherical shells for calculating the shown profiles. In the chemically unbonded case (blue curve), a significantly reduced density compared to the bulk epoxy is observed in the adjacent region of approximately 7 Å thickness. This reduction is due to the expulsion of epoxy caused by the physical interactions between the BNP and the epoxy. The chemically bonded case, shown in orange, also shows a reduced mass density region of approximately the same size. However, the reduction is significantly mitigated and bridged by the chemical bonds between boehmite the epoxy. Both cases reach the bulk epoxy density at a distance to the particle center of mass of approximately 25 Å. The simulations predict a bulk density of 1.161 g/cm^3, which is in good agreement with the literature values of 1.15 - 1.2 g/cm^3 [106].

The epoxy cross-link density profiles are plotted in Fig. 5.4 (b). The shown profiles include all cross-links created between two epoxy monomers or between epoxy monomers and curing agent molecules but exclude cross-links between epoxy and the BNP. From the comparison of the two cases, it could be concluded there are no considerable differences. However, this conclusion would be incorrect. In the chemically unbonded case, the epoxy cross-link density correlates well with the mass density profile from Fig. 5.4 (a). Since the epoxy is repelled from the region close to the BNP surface, the amount of cross-links is reduced compared to the bulk epoxy. The mass density profile of the strong chemical bonding case revealed that the expulsion of the material is much lower. In other words, the mass density in the interphase region with enabled chemical bonding is higher compared to the unbonded case. If the mass density is closer to the one of the bulk polymer, the same should apply to the epoxy cross-link density. This, however, is not the case in Fig. 5.4 (b), as both cases show an almost similar trend. Thus, it can be concluded that the enabled chemical bonding between the BNP and the epoxy impedes the epoxy cross-linking close to the BNP surface.

The total cross-link density profiles, shown in Fig. 5.4 (c), substantiate this argumentation. Since there is no chemical connection between boehmite and epoxy, the shown blue curve for the chemically unbonded case matches the one from Fig. 5.4 (b). In the chemically bonded case (orange), the total cross-link density shows a good agreement with the bulk epoxy for distances to the particle center of mass greater than 20 Å. In contrast, the epoxy cross-link density from 5.4 (b) reaches the bulk epoxy values at around 25 Å. This comparison shows that close to the boehmite

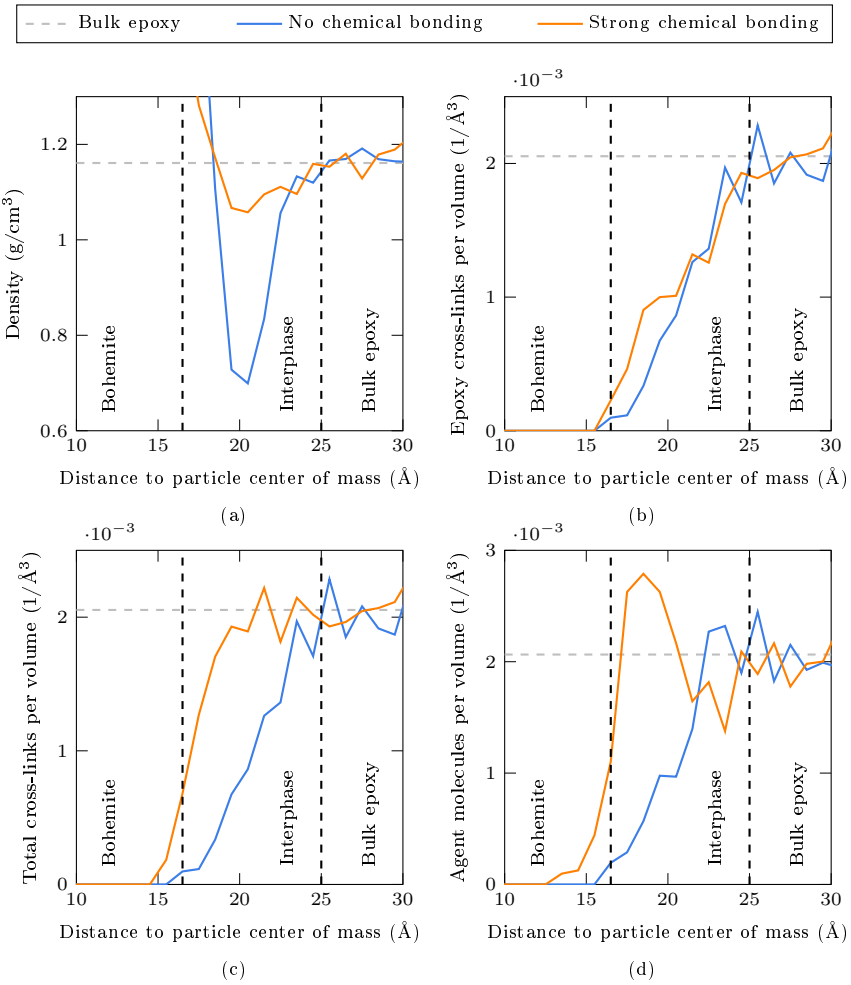

Figure 5.4: Comparison of the interphase network morphology of the BNP/epoxy samples without chemical bonding and with strong chemical bonding between the BNP and the epoxy after the equilibration simulations: (a) Radial mass density, (b) epoxy cross-link density, (c) total cross-link density and (d) density of curing agent molecules. The vertical dashed lines indicate the phase boundaries of boehmite and the interphase.

surface the majority of cross-links are created between boehmite and epoxy, leading to a low cross-linked epoxy region.

Another support can be found in the plot of the curing agent density profiles, which are shown in Fig. 5.4 (d). In the chemically unbonded case, again, the shown trend correlates well with the mass density and cross-link density profiles. The chemically bonded case leads to an accumulation of curing agent molecules close to the BNP surface, which explains the bridging of the mass density profile from Fig. 5.4 (a). Adjacent, towards the bulk material, a region of reduced curing agent density can be found.

The interphase in the chemically unbonded case is determined by the repulsion between boehmite and epoxy caused by the nonbonding interactions. This expresses through the region of reduced density shown in Fig. 5.4 (a) and the outward shift in the remaining three profiles. In the chemically bonded case, the repulsion between the two phases is mitigated by the covalent bonds. In addition, an alteration of the epoxy network due to the presence of the BNP is observed. In both cases, the interphase can be found between 17 and 25 Å away from the particle center of mass, which leads to a thickness of approximately 8 Å.

5.1.3 Preliminary Simulations

Similarly to the preliminary AFM simulations of the boehmite in chapter 3, the purpose of this section is to find the minimum required AFM tip and sample sizes. Therefore, AFM simulations of the bulk epoxy are conducted, with the AFM tip radii ranging from 1 to 5 nm and the sample sizes ranging from $9 \times 5.4 \times 9$ nm^3 to $15 \times 9 \times 15$ nm^3 with a constant aspect ratio. The sample size for the simulations with varying tip radii is chosen to be $15 \times 9 \times 15$ nm^3 and the tip radius for the simulations with varying sample size is chosen to be 3 nm. The results for both studies are shown in Fig. 5.5 and Fig. 5.6, respectively.

With increasing AFM tip size, the calculated moduli converge against a value of approximately 3.6 GPa. Small radii lead to an underestimation of the Young's modulus, but already for a tip radius of 3 nm, the deviation from the converged modulus is below 4%. As a compromise between efficiency and accuracy, for all following simulations, the tip size is chosen to be 3 nm. Generally, the AFM simulations seem to slightly overestimate the Young's modulus of the epoxy, but with an error of 7% they still show a good agreement with the result from the macroscopic tensile tests (3.37 GPa, Jux et al. [95]).

To this point, the good agreement between the simulated results and the experiments on the one hand and the large deviations from the results from chapter 4 on the other hand may seem surprising. The reason for this has partly been explained in the introduction of this chapter. The simulations presented here were performed

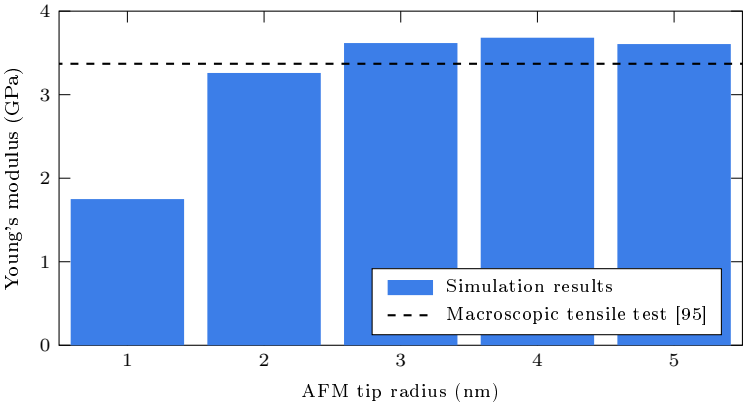

Figure 5.5: Influence of the AFM tip radius on the calculated Young's modulus of the bulk epoxy.

using the MDFEM, employing an NVE ensemble without a proper initialization of the energy. This means that temperature-related effects were not considered correctly. Again, from the author's point of view, this is inadequate and the simulations should be updated to a full-featured MD approach. Furthermore, in preparation for the AFM simulations, pure epoxy simulations were calibrated to fit the results of experimental tensile tests. Thereby, the effects discussed in chapter 4 were ignored. To correctly predict the interphase properties, it is crucial to understand these effects and incorporate them accordingly into the simulations. Since the AFM results presented in this section are no longer part of the multi-scale framework, these two recommendations were not realized here.

Compared to the boehmite samples from section 3.2.2, the FDC curves simulated for the bulk epoxy plotted in Fig. 5.6 show significantly larger fluctuations, which is particularly visible for the smaller models. The reason for this behavior is the amorphous polymer network, which is prone to sudden structural changes, like snaps from one equilibrium position to another. To allow for a reasonable fitting of the Hertz curve, the AFM tip displacement is increased compared to the AFM simulations of boehmite to a maximum value of 1.5 nm. The straight dashed lines in Fig. 5.6 represent the onset of a deviation of the simulated curves from the Hertz curve, which is caused by boundary effects. No dashed line is shown for the smallest sample size of $9 \times 5.4 \times 9$ nm^3 since its initial stiffness is already too high. The largest sample size of $15 \times 9 \times 15$ nm^3 is also not represented by a dashed line since a good agreement between the simulated curve and the Hertz curve is observed in the whole simulated displacement range. Similarly to the boehmite AFM simulations,

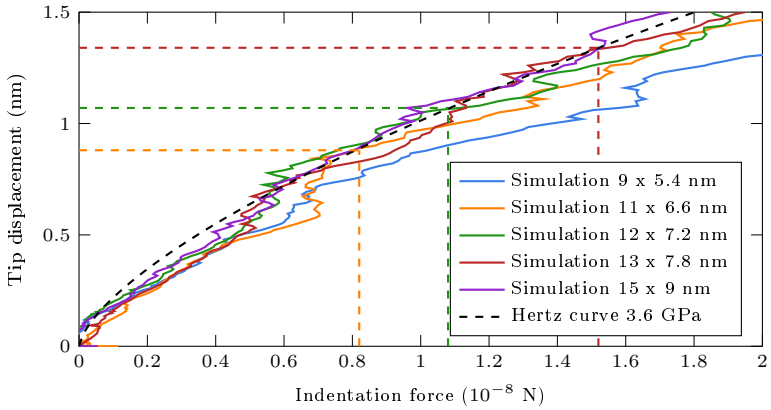

Figure 5.6: Influence of the sample size on the calculated FDC curves of epoxy. Only data points left of the vertical dashed lines are considered in the fit.

the onset of the deviation is shifted to lower deformations, when the sample size is decreased. To receive a sufficiently large range for the Hertz fit, but at the same time limit the numerical cost, a sample size of 12 × 7.2 × 12 nm^3 is chosen for all further simulations.

5.1.4 Elastic Properties of the Interphase

To obtain the gradient of the interphase Young's modulus (i.e. the dependence of the Young's modulus on the distance to the BNP surface), for each bonding case, 15 indentations are simulated on a radial line between 0 and 40 Å away from the particle surface, as illustrated in Fig. 5.2. The results are shown in Fig. 5.7. Similar to AFM experiments, the region close to the particle surface cannot be characterized, since, depending on the tip size, the tip flank and the particle overlap. Thus, in the region of approximately 1.7 nm around the particle, a mixed modulus is calculated. This region is excluded from Fig. 5.7 and the x-axis starts at a value of 1.5 nm.

Fig. 5.7 shows the comparison of the three different bonding cases. The reference case, which has no chemical bonding between the BNP and the matrix, but only physical interactions, exhibits a constant Young's modulus slightly above the experimental value. In this case, no interphase is visible, as it is hidden in the region where a mixed modulus is calculated (the x-axis in Fig. 5.7 starts at 1.5 nm). This is in agreement with the findings concerning the characteristics of the interphase network structure, where no alteration of the polymer network was observed. The second

case, denoted as medium chemical bonding (15% of the boehmite surface hydroxyl groups bonded to the epoxy), clearly shows a region of reduced Young's modulus which can be found between 18 and 38 Å away from the particle surface. The maximum stiffness reduction is approximately 1 GPa, which corresponds to a decrease of around 30%. Further away from the particle, the Young's modulus reaches the bulk epoxy value. The third case, which has a strong chemical bonding between the BNP and the epoxy (25% of the boehmite surface hydroxyl groups bonded to the epoxy), exhibits an even softer and larger interphase. In fact, the used models are too small to actually measure the extent of the interphase. The Young's modulus is reduced by a maximum of approximately 2 GPa, which is a decrease of 60%. Generally, in both chemically bonded cases, the reduction of the interphase stiffness can be attributed to the reduced epoxy cross-linking in the vicinity of the BNPs.

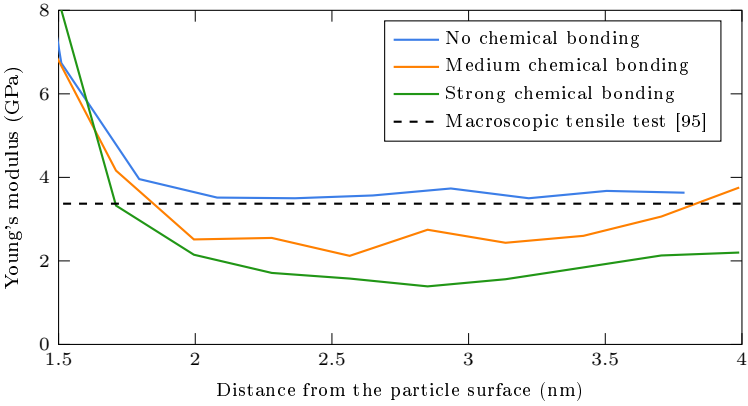

Figure 5.7: Interphase Young's modulus in dependence on the distance of the indentation from the particle surface.

Using AFM simulations for the determination of the elastic interphase properties has considerable drawbacks. Firstly, as mentioned before, due to the overlap of the AFM tip and the particle, mixed moduli are calculated instead of the actual interphase moduli in a region close to the BNP surface. It is shown later that the elastic properties of this region dominate the overall effective interphase properties. Secondly, even for small AFM tips, the probe volume is quite large. As schematically illustrated in Fig. 5.8, this leads to a smearing of the real stiffness gradient. Thus, the Young's moduli measured by AFM can be inaccurate and not representative of the exact measuring position. Furthermore, it can be assumed that the interphase thickness is overestimated due to the smearing, which is particularly problematic for small interphases, like the one investigated here. In fact, for the strong chemical bonding case, an interphase thickness of 8 Å was determined from the network

characteristics, whereas the AFM simulations indicate a drastically larger interphase. Thirdly, the network characteristics discussed above show that even without chemical bonds between boehmite and epoxy a small interphase exists, which is caused by the physical interactions. The same effect can occur between the AFM tip and the sample. Hence, in both AFM experiments and simulations, a mixed modulus of the tip-sample interphase and the sample is measured, which can lead to further inaccuracies. These major disadvantages led to the development of an alternative approach, which is presented in the following section.

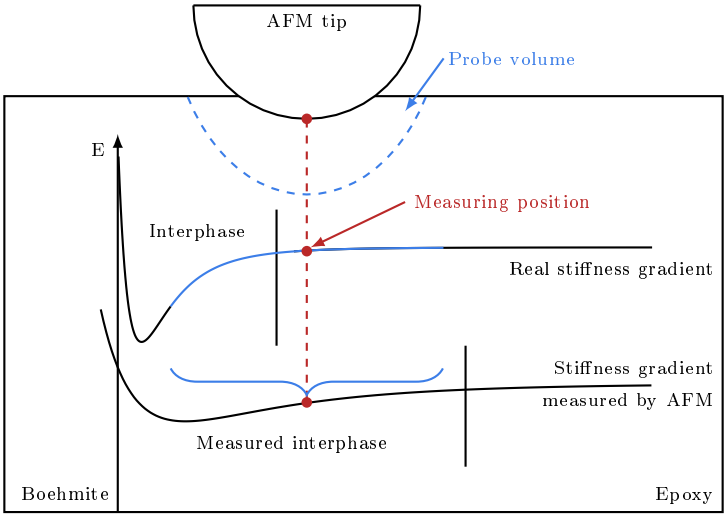

Figure 5.8: Schematic illustration of the smearing of the elastic properties in AFM.

5.2 Numerical Characterization of the Interphase of Layered Samples

To overcome the aforementioned difficulties, the previously introduced new approach for the direct calculation of the local elastic properties from MD simulations (compare section 2.2.1) is used to obtain the elastic properties of the BNP/epoxy interphase. The framework presented in the following comprises two characteristic features. Firstly, all simulations and hence the calculation of the local interphase properties are performed on layered samples that consist of a boehmite region embedded in two epoxy films, as shown in Fig. 5.9. The idea of layered samples has been successfully used for the non-mechanical characterization of the interphase in

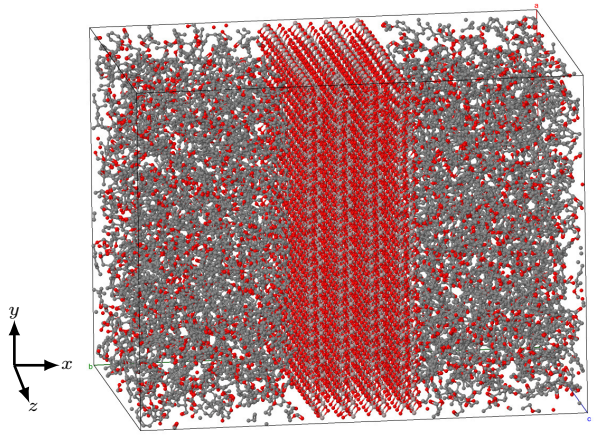

Figure 5.9: Exemplary model containing four boehmite layers embedded in two epoxy films.

the literature, as e.g. shown in [77–79]. Besides the geometrical simplification and hence the simplification of the calculation of the local elastic properties, with this approach, it is possible to get rid of particle size related effects. Secondly, and fundamentally, the approach presented in the following divides the simulation models into subsections, which are in this particular case slices of the model perpendicular to the boehmite layers. For each slice, the stress and strain tensor and ultimately the elastic properties are calculated according to section 2.2.1. Depending on the exact choice of the subsections (i.e. for instance the slice thickness), the effective interphase properties or the stiffness gradient throughout the interphase is accessible.

5.2.1 Modeling and Simulation Aspects

Similar to the previously discussed AFM simulations, the generation of the layered models is largely based on the previous chapters and sections. Thus, only the peculiarities of the layered structures are presented here. The model size for the following simulations is chosen to be $8.4 \times 6.5 \times 6.2$ nm^3. The in-plane dimensions (y- and z-direction) are determined based on the crystalline structure, so that periodicity is achieved. The thickness of the boehmite region is chosen in such a way that no physical interactions between the two epoxy layers are present. This is fulfilled for a thickness of 2.4 nm, which corresponds to four boehmite layers. The epoxy films

must be thicker than the maximum interphase thickness, which is caused by the presence of the boehmite layers. It is shown later that this assumption is fulfilled for the chosen thickness of 3.3 nm. It should be noted that in this setup no specific weight fraction is used. Since only the interphase properties are determined, and not the NC properties, the weight fraction is irrelevant for the simulations.

All simulations are performed with a full-featured MD approach using LAMMPS [103] in combination with the Dreiding force field [112], harmonic bond potentials and Lennard-Jones-(12,6) potentials for the nonbonding interactions. With the exceptions discussed in the following, all parameters are similar to the cross-linking simulations of the pure epoxy from chapter 4. It was previously mentioned that the simulations of the layered structures are performed employing an NPH ensemble with a Nosé-Hoover barostat [113] and an additional Langevin thermostat [114] instead of the Hoover NPT. The reason for this is illustrated in Fig. 5.10. Due to the internal formulation of the Nosé-Hoover thermostat, the temperature is always controlled globally for the whole simulation box. If, like in the present case, materials of vastly different structures are combined in one model, this approach can lead to unphysical temperature profiles, as can be seen in Fig. 5.10 (a). Using the Hoover NPT, the crystalline boehmite region has a significantly higher temperature than the specified 300 K, while the polymer region remains at 0 K. The Langevin thermostat, in contrast, can be used to control the temperature in subsections of the simulation model. Here, three regions are defined, which correspond to the boehmite region and the two epoxy regions. Fig. 5.10 (b) shows, that with this approach a reasonable temperature profile can be achieved. The peaks or lows in both subfigures, that reach beyond the boundaries of the plot, correspond to the inter-layer gaps between the boehmite sheets or between boehmite and the adjacent epoxy region. In these regions, only a small number of atoms may be used for the temperature calculation, which can lead to meaningless values. It should furthermore be noted, that a Langevin thermostat does not produce an exact physical ensemble, but can be assumed to produce comparable results to the Hoover NPT for large enough systems. This has previously been proven for the bulk epoxy simulations in section 4.4.5.

The layered structures are cross-linked with the dynamic approach presented in section 4.3. Similar to the generation of the AFM models, the boehmite surface hydroxyl groups are enabled to join the polymer cross-linking reaction, as described in section 5.1.1. In the curing simulations, cross-links are formed, whenever reactive sites come closer than a specified maximum reaction distance. By varying these distances, the interfacial bonding can be changed. In the following, two cases are simulated, whose chemical structures are shown in Fig. 5.11. The corresponding maximum reaction distances, which are linearly increased throughout the simulations, are presented in Tab. 5.1.

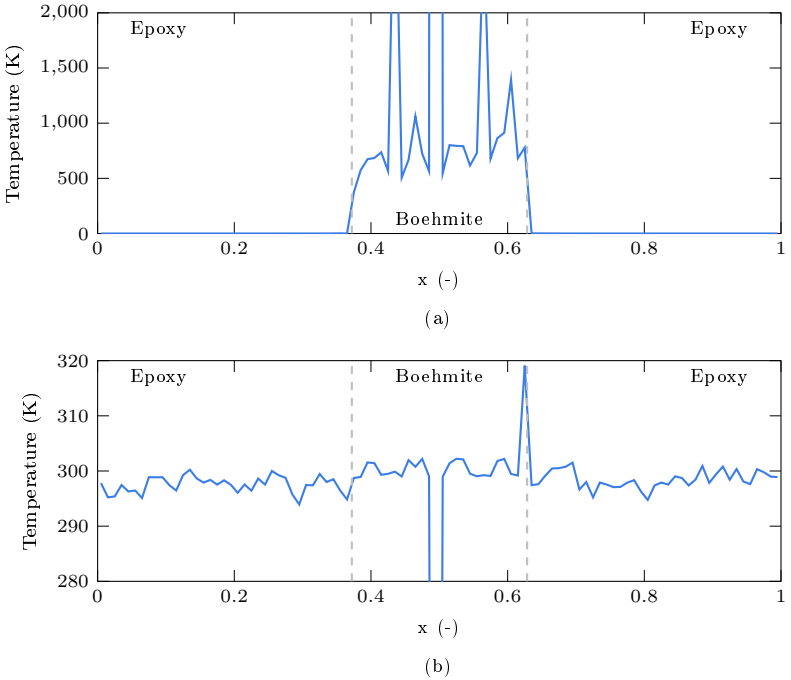

Figure 5.10: Comparison of the temperature profiles simulated with (a) an isothermal-isobaric (NPT) ensemble and (b) an isoenthalpic-isobaric (NPH) ensemble with an additional Langevin thermostat.

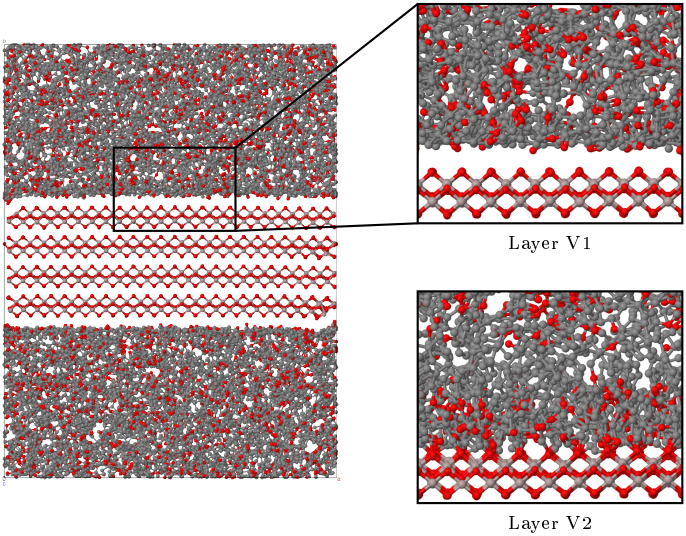

Figure 5.11: Comparison of the molecular structures of the chemically unbonded case (Layer V1) and the chemically bonded case (Layer V2).

Table 5.1: Maximum reaction distances and curing characteristics (r_x: maximum reaction distance, Indices: $_{est}$: esterification, $_{eth}$: etherification, $_b$: esterification or etherification of boehmite hydroxyl groups).

Model type	Pure epoxy	Layer V1	Layer V2
r_{est} (Å)	2.5 - 4.5	2.5 - 7.0	2.5 - 7.0
r_{eth} (Å)	1.5 - 3.5	1.5 - 4.0	1.5 - 4.0
$r_{est,b}$ (Å)	-	-	6.5 - 11.5
$r_{eth,b}$ (Å)	-	-	5.0 - 10.0
Degree of curing (%)	92	88	55
Boehmite OH usage (%)	-	-	49

The term degree of curing describes the percent usage of the methyl groups of the monomers. As a reference, the degree of curing of the bulk epoxy simulation box from chapter 4 is shown, which amounted to 92%. The assumptions of the two bonding cases discussed here can be understood as extreme cases, which deliver an upper and lower bound for the interfacial bonding and thus for the elastic interphase properties. Case one, which will be denoted as Layer V1 from here on, has no chemical bonds between the boehmite region and the surrounding epoxy. The comparison to the bulk epoxy shows that slightly larger maximum reaction distances have to be used to obtain a comparable degree of cross-linking. This is caused by the reduced mobility of the monomers and curing agents due to the presence of the boehmite layer. Case two, which will be denoted as Layer V2 in the following, has a strong chemical interaction between the boehmite layer and the surrounding epoxy regions. This expresses through considerably larger maximum reaction distances of the boehmite surface hydroxyl groups. With the assumptions shown in Tab. 5.1, approximately 49% of the surface hydroxyl groups of the boehmite have developed covalent bonds to the epoxy, which is indicated by the term Boehmite OH usage in Tab. 5.1. As a result, the degree of curing in the polymer region is significantly reduced compared to Layer V1. A more detailed discussion of the characteristics of the cured network structure in dependence on the interfacial bonding can be found in section 5.2.2.

After the curing simulations, the generated systems are cooled down and equilibrated for a period of 1.5 ns at a temperature of 300 K and a pressure of 1 atm. The uniaxial tension is applied at a temperature of 300 K with a strain rate of 10^7 1/s and a pressure of 1 atm in the transverse directions. For both the equilibration and the loading, an NPH ensemble with and additional Langevin thermostat is used, as explained before.

5.2.2 Characteristics of the Interphase Network Structure

In this section, the characteristics of the interphase network structure are discussed in detail. Therefore, the variation of three characteristic variables over the interphase thickness is analyzed, which are the mass density, the total cross-link density (i.e. the total amount of cross-links per unit volume including cross-links between boehmite and epoxy) and the amount of curing agents per unit volume. These profiles are calculated by slicing the simulation box into 100 slices parallel to the boehmite sheets (which corresponds to the x-direction). For each slice, the respective characteristic variable is calculated and plotted against the x-coordinate of the corresponding slice. Fig. 5.12 illustrates this procedure for 8 slices.

The gradients of the characteristic variables are shown in Fig. 5.13. The gray and colored dashed lines indicate the phase boundaries of boehmite and the respective interphase. The orange curves refer to the case Layer V1 (no chemical bonding

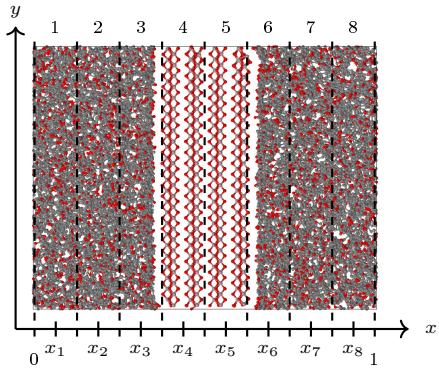

Figure 5.12: Schematic illustration of the calculation of the characteristic variables plotted in Fig. 5.13.

between the boehmite and the epoxy region) and the green curves to Layer V2 (covalent bonding between the layers). The shown boundaries are the result of the network characteristics presented in this section. How the positions of the phase boundaries were determined is explained at the end of this subsection.

The mass density profiles are shown in Fig. 5.13 (a). The boehmite region, bounded by the gray dashed lines, can clearly be distinguished from the epoxy region. Even the four layers, that the boehmite region consists of, are visible. With a value of 2.79 g/cm^3, the average boehmite density shows a good agreement with the value of 2.84 g/cm^3 reported in the literature [36]. In the epoxy region, the mass density profile of Layer V1 shows the typical variation in the vicinity of boehmite, which is due to the repulsion between the boehmite and the epoxy region caused by the nonbonding interactions. This variation has been comprehensively reported in the literature (e.g. in [73, 77]). Apart from that, a good agreement between the mass density of the bulk polymer of Layer V1 and the pure epoxy polymer box is visible. The average polymer density is 1.16 g/cm^3, which is in good agreement with experimental data reported in the literature (i.e. 1.15 - 1.2 g/cm^3 [106]). The mass density profile of Layer V2, in contrast, reveals significant differences. The gap between the polymer and the boehmite region caused by the repulsion is reduced. This is a result of the considerable amount of cross-links between boehmite and epoxy, as approximately half of the boehmite surface hydroxyl groups are chemically bonded to epoxy monomers. Furthermore, the aforementioned variation of the mass density is overlayed by a second effect. Caused by the covalent bonds between boehmite and epoxy, a significant amount of curing agent molecules and monomers is drawn to the boehmite surface, forming a high-density region in the vicinity of the boehmite. This, in turn, causes a slight mass density reduction in the adjacent

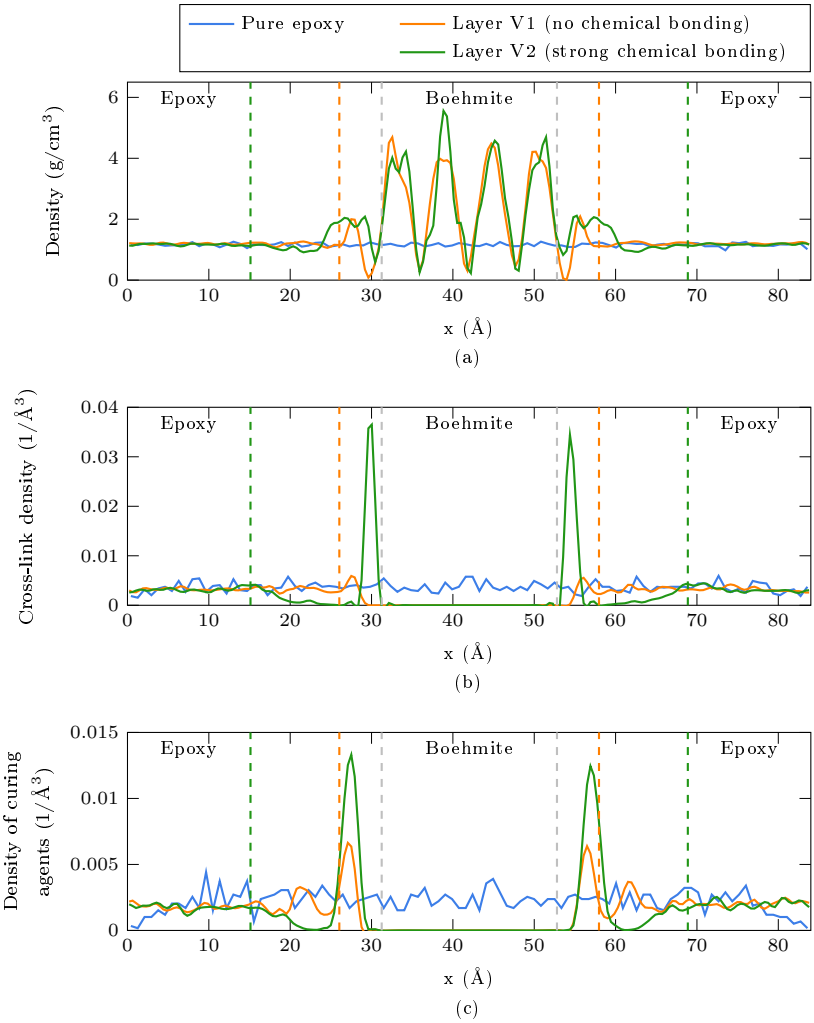

Figure 5.13: Characteristics of the cured network structure of the two different bonding cases Layer V1 and Layer V2 compared to the pure epoxy polymer box: (a) mass density; (b) cross-link density and (c) density of agent molecules. The gray dashed lines indicate the phase boundaries of boehmite and the respective colored dashed lines depict the interphase boundaries for the two investigated bonding cases.

region towards the bulk material.

The cross-link density profiles are shown in Fig. 5.13 (b). In the boehmite region, bounded by the gray dashed lines, the cross-link density is zero. In accordance with the findings from the mass density profile, the epoxy regions of Layer V1 behave similarly to the pure epoxy box except for the repulsion region close to the boehmite surface. In other words, an undisturbed epoxy network can form in almost the whole epoxy region. Again, the cross-link density profile of Layer V2 shows considerable differences. A significant amount of cross-links is formed close to the boehmite surface, which mainly connect reactive sites of boehmite and epoxy. This leads to an adjacent region of very low cross-linked epoxy. Beyond x-values of approximately 15 and 69 Å, the cross-link density reaches the bulk epoxy values and thus has a comparable network structure.

The profiles of the density of curing agent molecules are shown in Fig. 5.13 (c). Again, the repulsion between boehmite and epoxy is visible. The peaks in the Layer V1 profile, located at x-values of approximately 28 and 56 Å, seem to be disproportionally high and are thus assumed to not only originate from the repulsion. Instead, this effect could be caused by the presence of the boehmite region, which forms a barrier for the highly mobile curing agent and by the gap between boehmite and epoxy, which provides an energetically favorable location for the agent molecules. In case of the chemically bonded regions (Layer V2), caused by the cross-linking between epoxy and boehmite, even more hardener molecules gather at the boehmite surface, leading to a distinct depletion of curing agents in the adjacent epoxy region.

Concluding from the aforementioned, Layer V1 largely behaves like three separate phases, except for the repulsion region. In contrast, Layer V2 deviates significantly in all the three characteristic variables, leading to a considerably changed polymer network in the vicinity of the boehmite region. Per definition, an interphase is a region of changed material caused by the presence of a second phase. For Layer V1, the interphase is determined by the repulsion of epoxy close to the boehmite surface, as can be seen in the mass density profile. This is in accordance with existing literature (e.g. [73, 77]) and the results from section 5.1.2, leading to an interphase thickness of approximately 5 Å (as indicated by the dashed orange lines in Fig. 5.13). Layer V2, however, shows that this is only valid as long as no chemical bonding between the phases is present. If the phases are covalently bonded, the interphase region may rather be defined by the altered polymer network, leading to a larger interphase thickness of approximately 15 Å, as indicated by the dashed green lines in Fig. 5.13. The changed polymer network is generally in accordance with the findings from section 5.1.2. However, the interphase thickness was reported to have a thickness of 8 Å in section 5.1.2. The differences can be attributed to two effects. Firstly, in the layered structures, a much higher amount of bonded boehmite surface hydroxyl groups of 50% (compared to the maximum of 25% in the AFM models) was assumed, which is expected to have a bigger impact on the interphase network and

to result in a larger interphase. Secondly, the usage of a real MD approach including temperature can lead to a better equilibration and hence to a more realistic network structure.

A validation of these results with experimental studies is challenging since a direct characterization of the local network structure or density in the interphase region has not been established so far. However, there are some studies, that seem to support the findings presented above. Stafford et al. [126] and Torres et al. [127] performed AFM experiments on layered polymethylmethacrylate (PMMA)/polydimethyl-siloxane samples with varying PMMA film thickness. The results were fitted with a micro-mechanical model, resulting in an interphase thickness of 2 nm and 3.5 nm, respectively. In another article, Ciprari et al. [128] measured the interphase thickness employing thermogravimetric analysis. The resulting interphase thickness of PMMA and polystyrene with different fillers was reported to fall within the range of 4 - 10 nm. It should not remain unmentioned that other studies report larger interphases. Ghasem Zadeh Khorasani et al. [129], for instance, performed ImAFM experiments and reported an interphase thickness of 50 nm for boehmite epoxy NCs. Generally, the transferability of the experimental and numerical results is questionable, since the simulations imply an idealized structure, which can be used to investigate the interphase separated from other effects, that may be present in the experiments, such as a possibly particle size dependency or agglomeration. In turn, the idealized models may lack some important effects, like a possible segregation of the constituents of the polymer at the phase boundary.

5.2.3 Elastic Properties of the Interphase

After the discussion of the network characteristics, the influence of the interfacial bonding between boehmite and the surrounding epoxy on the elastic interphase properties is addressed in this section. Therefore, the layered models are subjected to an in-plane tensile load. A loading perpendicular to the layers is neglected since it results in comparatively large inter-layer deformations between boehmite and epoxy and between the boehmite layers. This makes a correlation between the findings concerning the network characteristics and the results of the mechanical loading increasingly difficult. To compensate this, the number of simulation models is increased to ten randomly generated models per case (i.e. Layer V1 and Layer V2). After loading, the local approach from section 2.2.1 is used to calculate the local elastic properties of the interphase. Two different cases are considered in the following. Firstly, similar to the previously explained network characteristics, the models are divided into 100 slices parallel to the boehmite sheets (compare Fig. 5.12). This allows for the calculation of the stiffness gradient throughout the interphase. Secondly, the models are divided only into five slices, which correspond to the boehmite region, the two bulk epoxy regions and the two interphase regions.

With this approach, the effective interphase properties can be determined as an input for the microscale simulations presented in the following chapter.

Fig. 5.14 plots the Young's modulus profiles calculated with the local approach dividing the models in 100 slices. The dashed lines in Fig. 5.14 are inherited from section 5.2.2, where the gray dashed lines indicated the boehmite boundaries and the colored dashed lines showed the boundaries of the respective interphase. The black dashed line in Fig. 5.14 marks the Young's modulus of the pure epoxy, as calculated in section 4.4.1.

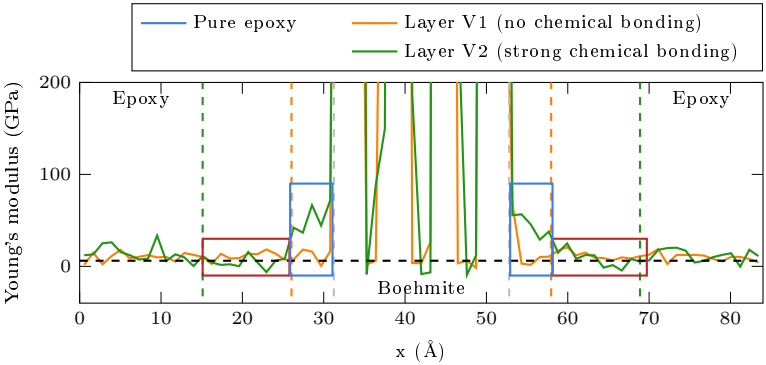

Figure 5.14: Young's modulus profile for the two different bonding cases Layer V1 (no chemical bonding) and Layer V2 (strong chemical bonding).

The boehmite and epoxy regions can clearly be distinguished in the profiles shown in Fig. 5.14, as at the gray dashed lines the stiffness drastically increases. Even the four boehmite layers and the interlayer gaps can be identified. The boehmite stiffness is not calculated here since the assumption of an isotropic material is not valid for the layered crystalline structure of boehmite. The assumption of an orthotropic behavior, in turn, requires the simulation of more load states (e.g. shear loading), to be able to calculate the nine independent material parameters.

The regions of interest, the interphase regions, are located between the gray dashed lines and the respectively colored dashed lines in Fig. 5.14. The orange curve represents the chemically unbonded case (Layer V1) and the green curve the case with covalent bonds between boehmite and epoxy (Layer V2). Layer V1 exhibits no significant deviations from the pure epoxy, as the stiffness is almost constant in the range of the bulk epoxy stiffness. This mirrors the findings of the characteristics of the network structure presented in section 5.2.2, where no considerable alteration of the Layer V1 interphase network was observed. Layer V2 shows distinct deviations from the bulk epoxy stiffness in the regions close to the boehmite surface highlighted

by the blue boxes. These regions are characterized by an increased mass density, an accumulation of curing agent molecules and a high inter-layer cross-linking. The so changed network leads to a significantly increased Young's modulus in this region compared to Layer V1. The regions highlighted by the red boxes, in turn, have a slightly reduced mass density and a much lower cross-link density. Thus, a reduction of the Young's modulus is expected. However, the results calculated for the 100 thin slices are not sensitive enough, to clearly reveal such effects.

The shown stiffness gradients provide an insight into the influence of the changed network structure on the local elastic properties of the NC interphase. However, due to the low thickness of the slices and the rather low number of simulations, the stresses and strains are averaged over a low number of atoms, which can result in comparatively large stiffness fluctuations or sometimes even unphysical behavior. To overcome this and to provide input for the FE models on the next higher scale, the effective interphase properties are calculated. Therefore, instead of 100 slices, the models are subdivided into five slices, that correspond to the boehmite region (bounded by the gray dashed lines in Fig. 5.14), the two interphase regions (between the gray and the respective colored dashed lines) and the two bulk epoxy regions (outside of the colored dashed lines). For each of these five regions, the stresses, strains and the elastic properties are calculated using the local approach. The results are shown in Tab. 5.2.

Table 5.2: Effective elastic properties of polymer matrix and the interphase for the two different bonding cases Layer V1 and Layer V2: Young's modulus E, Shear modulus G and Poisson's ratio ν.

	Layer V1		Layer V2	
	Bulk epoxy	Interphase	Bulk epoxy	Interphase
E (MPa)	5998 ± 170	4961 ± 350	6083 ± 293	22818 ± 159
G (MPa)	2247 ± 38	1904 ± 57	2305 ± 87	8643 ± 67
ν (-)	0.334	0.303	0.320	0.320

The resulting bulk epoxy properties are in good agreement with the ones calculated for the pure epoxy simulation box from section 4.4.1. The interphase of Layer V1 has a slightly reduced stiffness, which is caused by the weak physical interaction between boehmite and epoxy. The resulting interphase stiffness is approximately 5 GPa, which corresponds to a reduction of 17% compared to the bulk epoxy. The interphase of Layer V2, in contrast, has a significantly increased stiffness, caused by the strong chemical bonding between boehmite and epoxy. This leads to a Young's modulus of approximately 22.8 GPa, which is nearly four times the bulk epoxy stiffness. The overall increase of the interphase stiffness for Layer V2 indicates that the influence of the high-density region with a high density of inter-layer cross-links

(blue region in Fig. 5.14) dominates the effects related to curing agent depletion and reduced cross-linking (red region in Fig. 5.14). The shear moduli of the interphases result in values of 1904 and 8643 MPa, which is a reduction of 15% and an increase of 275% for Layer V1 and Layer V2, respectively. The poisons ratios are calculated using the relation $\nu = E/2G - 1$, leading to values of 0.303 and 0.320. There is no standard deviation given for the Poisson's ratios since they are calculated from the average Young's modulus and the average shear modulus.

It should again be mentioned that a validation using experiments is challenging. To the best knowledge of the author, there is no direct experimental measurement of the elastic interphase properties available in the literature. Studies, which apply indirect methods, such as the ones discussed in the previous section [126–128], typically report interphase stiffnesses below the bulk polymer modulus. This is in agreement with the results of the AFM simulations presented in section 5.1 and also with the results of the Layer V1 case discussed above. The results presented in the named articles, however, were obtained by fitting micro-mechanical models to AFM results. Thus, and because of the restrictions of the AFM itself (i.e. e.g. the overlap between the particle phase and the AFM tip and the smearing of the material behavior due to the large probe volume), it is questionable if the experiments would be able to measure the small region of increased stiffness, which was found for the chemically bonded case discussed above. Of course, as mentioned before, Layer V2 represents an extreme case and thus the increased interphase stiffness does as well.

5.3 Conclusions

In this chapter, two approaches for the characterization of the boehmite/epoxy interphase were presented and discussed. The ultimate goal was to gain an insight into the influence of the interfacial bonding between the crystalline filler and the polymer on the elastic interphase properties.

The investigation of the network characteristics of the different bonding cases exposes the nature and also the size of the interphase region. Thereby, a good correlation between the findings on a particulate AFM model and the layered samples is observed. In both cases, if the boehmite and epoxy regions are chemically unbonded, an undisturbed epoxy network can form almost until the phase boundary. The interphase is then mainly characterized by a changed density profile due to the repulsion caused by the physical interactions between boehmite and epoxy. In the chemically bonded cases, the interphase is not only defined by a changed polymer density, but also by an alteration of the network structure. Thus, it seems reasonable to check the curing characteristics, such as the cross-link density, in addition to the mass density, to define the spatial extent of the interphase. With a thickness of 8 Å for the particulate sample, the interphase was found to be of similar thickness

in the chemically unbonded and strongly bonded (i.e. 25% of the boehmite surface hydroxyl groups being bonded to the epoxy) case. The chemically unbonded layered models (Layer V1) show a reasonable agreement with the AFM samples and result in an interphase thickness of 5 Å. For Layer V2 (50% of the boehmite surface hydroxyl groups being bonded to the epoxy), in contrast, the interphase thickness amounted to 15 Å. The differences can be attributed to the higher amount of interfacial cross-links and the more realistic equilibration obtained with the full-featured MD approach used for the layered structures.

The interphase stiffness profiles calculated from the AFM simulations show a maximum reduction of the Young's modulus of 30 to 50% compared to the bulk epoxy. Furthermore, from the stiffness gradient, an interphase thickness of 38 Å was calculated for the medium bonding case. The case with strong chemical bonding showed an even larger interphase, which could not be quantified, because the simulation models were too small. These values conflict with the findings concerning the network characteristics, where independently of the interfacial bonding an interphase thickness of only 5 Å was observed. Since the curing characteristics are compatible with the ones of the layered structures, the reason for this behavior is presumably the smearing of the material behavior caused by the large probe volume. Besides that, a disadvantage of the AFM simulations is the inevitable measurement of mixed moduli close to the BNP, which prevents a proper calculation of the interphase Young's modulus. To solve these problems, the BNP/epoxy interphase was investigated using the new approach for the direct calculation of the local elastic properties from MD simulations. For the chemically unbonded case, a reduction of the effective interphase stiffness compared to the bulk epoxy stiffness of 17% was obtained. The extreme case of enabled chemical bonding resulted in an increase of the interphase stiffness of 275% compared to the bulk epoxy. Thus, the small region of significantly increased stiffness close to the particle surface found in the stiffness profiles dominates the effective interphase stiffness. Due to the overlap of AFM tip and particle, the AFM simulations are not able to extract the properties in this region and hence predict inaccurate effective interphase stiffnesses. The downside of the layered models is that they are not sensitive enough to clearly reveal the expected region of reduced stiffness, which is observed in the AFM simulations. Still, this region is included in the calculation of the effective Young's moduli. If the stiffness gradient is needed, the sensitivity could be improved by increasing the number of random models used in the underlying MD simulations.

An important extension of the work presented in this chapter is a comprehensive investigation of the influence of agglomeration on the formation of the interphase. In the scope of this thesis, a possible influence is neglected and the effective interphase properties are assumed to be independent of the state of agglomeration. Hence, in chapter 6, the main mechanism is the reduction of the interphase volume caused by the closely located primary particles inside of the agglomerates. The validity of this assumption is unproven. It is imaginable that epoxy, which is trapped between

boehmite particles, develops a different interphase than epoxy on the outside. This effect could be considered by simulating UCs consisting of agglomerated particles embedded in the polymer. This, however, seems unfeasible with MD simulations, since the numerical effort would exceed the available resources. Coarse-graining methods can help to establish such simulations. Nevertheless, the extraction of the local elastic properties from such models is complicated because of the complex geometry. As an alternative approach, again layered structures can be used, which consist of an epoxy film embedded in two boehmite regions, as shown in Fig. 5.15. With this approach, the situation inside of an agglomerate can be mimicked and varying epoxy film thicknesses can be used to calculate the interphase properties depending on the interparticulate distance.

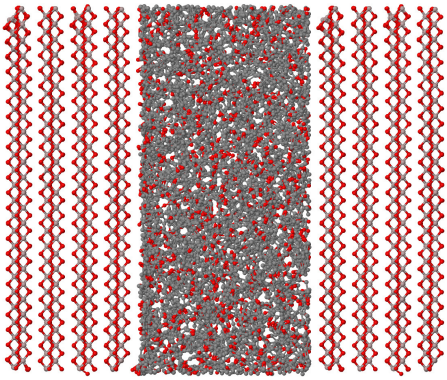

Figure 5.15: Layered model for the investigation of the interphase formation inside of agglomerates: Epoxy film surrounded by two boehmite layers.

All the findings presented in this chapter strongly depend on the assumptions made in the model generation process and, specifically on an adequate modeling of the chemical structure of the interphase. Because of the lack of possibilities for experimental validation, it remains unclear how representative the used models and the underlying assumptions are. Further scientific work should aim at establishing direct validation possibilities, both from the numerical and experimental perspective. Other extensions of the presented methods are the implementation of coarse-grained force fields, which would allow for the simulations of larger time and length scales and hence more realistic systems. Furthermore, a proper consideration of the effects discussed for the bulk epoxy in chapter 4, such as strain rate effects or effects related to the choice of the force field, should be striven for.

6 Microscale

With the findings from the previous chapters, the transition from the atomistic level to the continuum based microscale is accomplished. In this chapter, the FE models are constructed based on the elastic properties of the constituents and geometrical aspects, such as the interphase thickness or the cumulative distribution function of the primary particle distances. The ultimate goal is to investigate the influence of three major effects, which are the elastic interphase properties, the agglomerate size and size distribution and the question of whether the agglomerates are filled with polymer or not.

Three levels of detail are considered in this chapter, which are shown in Fig. 6.1. The first case, illustrated in Fig. 6.1 (a), are RVEs consisting of homogeneously distributed BNPs embedded in the epoxy matrix. These models are intended to provide an insight into the influence of the elastic interphase properties on the NC behavior separated from agglomeration effects. Additionally, they are used to calibrate the FEM simulations, e.g. regarding the choice of the boundary conditions. The findings of these RVEs are then transferred to the agglomerate UCs, which represent the second case, as shown in Fig. 6.1 (b). With these models, the influence of the reduction of the interphase volume due to agglomeration and the question of whether agglomerates are filled with polymer or not are addressed. The last case, illustrated in Fig. 6.1 (c), are agglomerate RVEs. These models contain a

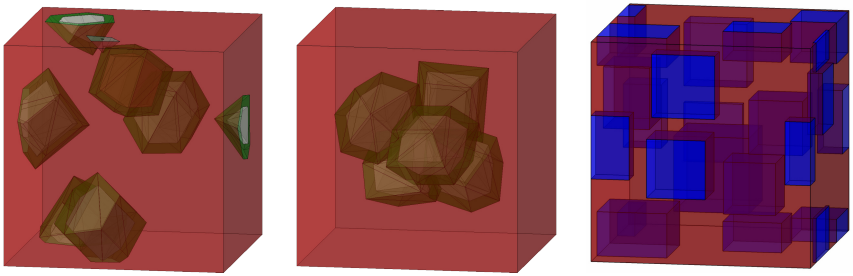

(a) (b) (c)

Figure 6.1: Exemplary FE model of (a) an RVE of homogeneously distributed BNPs in epoxy matrix, (b) an agglomerate UC and (c) an agglomerate RVE.

representative number of agglomerates according to the experimental agglomerate size distribution and utilize the elastic properties obtained from the agglomerate UCs. Ultimately, they allow for a comparison of the simulated NC properties to the experiments.

6.1 Experimental Characterization of the Boehmite/Epoxy Nanocomposite

Within the FOR2021 project, the mechanical behavior of the boehmite/epoxy NC was comprehensively characterized by macroscopic experiments. In [95], the elastic properties were studied depending on the surface modification and thus, presumably, also depending on the interfacial bonding. In particular, two cases were investigated, which are unmodified and acetic acid modified BNPs. Thereby, the unmodified case is assumed to chemically react with the polymer, whereas the acetic acid presumably shields the BNPs from the epoxy and prevents chemical interactions. The key results of this study are presented in Fig. 6.2 (a). Both modifications lead to an almost linear increase of the Young's modulus with increasing weight fraction of the BNPs. The overall difference between the two surface modifications is small, with a maximum deviation of 6% for the maximum BNP weight fraction of 15%. However, the trend of the acetic acid modification leading to a higher stiffness compared to the unmodified BNPs is surprising. It could be interpreted in such a way that the acetic acid leads to an undisturbed polymer network with a higher stiffness in the vicinity of the boehmite surface and thus to a higher overall Young's modulus. This, however, is in contradiction to the findings from chapter 5, where the effective interphase stiffness was found to be significantly increased when chemical bonding between the particle and the polymer is present. The exact reason for the higher Young's modulus in case of the acetic acid modification remains unclear. It can be speculated that the assumed weakening or prevention of chemical interactions by the acetic acid is incorrect. Preliminary AFM results seem to substantiate this hypothesis [130].

Furthermore, the Young's modulus of the unmodified BNP NC was investigated in dependence on the mean agglomerate size, as reported in [131] and shown in Fig. 6.2 (b). In this article, three different average agglomerate sizes of 138, 224 and 354 nm were investigated. With a maximum difference of 71 MPa between the smallest and the largest agglomerate size, which is a percentage of 1.8%, the resulting influence on the Young's modulus is small. Still, from the three available data points, a declining trend can be observed. The comparison to the Young's modulus of the average agglomerate size of 105 nm from [95], however, does not fit in this trend. Presumably, the samples are from different batches, which is why a direct comparison could be misleading.

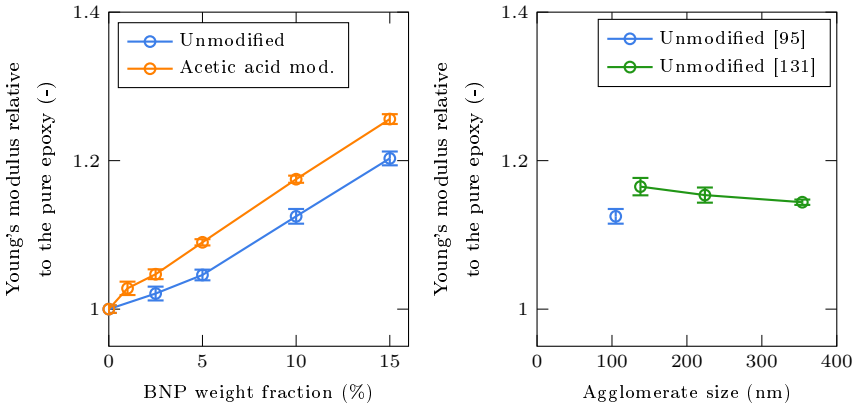

Figure 6.2: Experimental studies of (a) the Young's modulus in dependence on the surface modification and the particle weight fraction at a mean agglomerate size of 105 nm from [95] and (b) the Young's modulus in dependence on the mean agglomerate size at a weight fraction of 10% from [95, 131].

Agglomerates typically do not have an exact spherical shape. From a numerical perspective it is unclear how the agglomerate size can be objectively calculated. Furthermore, from the authors' point of view, the important parameter is the number of primary particles per agglomerate rather than the agglomerate size itself. To relate the experimental results to the numerical results, the number of primary particles per agglomerate has to be correlated to the agglomerate size. Here, a closest sphere packing and spherical primary particles and agglomerates are assumed. Since the experimentally observed influence of the agglomerate size on the elastic properties is small, these assumptions should have a minor influence on the comparison between experiment and simulation. With the above assumptions, the number of primary particles per agglomerate can be calculated as

$$n_{pp} \approx 0.74 \frac{d_{agg}^3}{d_{pp}^3}. \tag{6.1}$$

Thereby, d_{agg} and d_{pp} are the agglomerate diameter and the primary particle diameter, respectively and 0.74 is a factor to describe the fraction of the agglomerate volume that is occupied by particles in the closest sphere packing. The estimated numbers of primary particles per agglomerate are shown in Tab. 6.1.

Table 6.1: Estimated number of primary particles per agglomerate in dependence on the agglomerate size.

Agglomerate diameter (nm)	Estimated number of primary particles
105	312
138	709
224	3031
354	11963

6.2 Homogeneously Distributed Primary Particle RVEs

In this section, the modeling, calibration and simulation results of the RVEs containing homogeneously distributed primary particles are presented. In the following, these models are denoted as "homogeneous RVEs".

6.2.1 Modeling and Simulation Aspects

The primary particles, whose shape is chosen based on information from the manufacturer [111] and experimentally confirmed through X-ray diffraction measurements [109], are known from the previous chapters and modeled with the reduced primary particle size of 3 nm. The interphases are assumed to have the same but accordingly enlarged shape as the particles. The thickness is chosen based on the findings from chapter 5 with values of 0.5 nm for the chemically unbonded and 1.5 nm for the bonded case.

The fundamental idea of the generation of the homogeneous RVEs is a hardcore algorithm, which has been implemented into Abaqus. These algorithms are typically used for the generation of random models with a rather low volume or weight fractions. The particles are randomly placed into the simulation box with random orientation and checked for intersection with already placed particles. If an intersection is detected, the particle is removed and placed at another random position, until no intersection occurs anymore. In contrast to the particles, the interphases may intersect. In other words, particles can be placed closer to each other than twice the interphase thickness. The whole geometry is periodic, meaning that particles and interphases that protrude beyond the box boundaries reappear on the opposing boundary, as can be seen in Fig. 6.1 (a).

One purpose of the homogeneous RVEs is to investigate if periodic boundary conditions are necessary for the microscale simulations. Thus, a periodic mesh is required.

Even though the outer surfaces are symmetric, this can be challenging because of the non-symmetric inner structure of the microscale models. The process is complicated by the lack of periodic mesh constraints in the Abaqus meshing tool. Furthermore, copying the surface mesh from one surface to the opposing surface could not be satisfactorily established in an automated way. Thus, the models are exported and meshed in Gmsh [132], an open-source tool that provides the necessary features to generate periodic meshes, and re-imported into Abaqus.

The FE simulations presented in the following are performed with the commercially available Abaqus solver. All materials are modeled as linear and isotropic, employing the elastic material model, which is available in Abaqus. A summary of the elastic properties applied, which were obtained in the previous chapters, is presented in Tab. 6.2. Due to the geometrical complexity, the models are meshed with quadratic tetrahedral elements (C3D10). Since a linear material is used, the simulation results are assumed to show a minor dependence on the chosen element size, especially for quadratic elements. This assumption is checked in the following section, where the element size for further simulations is presented. In addition, PBCs and DBCs are compared to detect if PBCs are necessary for the microscale simulations.

Table 6.2: Summary of the elastic properties applied to the simulation of the microscale RVEs.

	Young's modulus (GPa)	Poisson's ratio (-)
Boehmite	212	0.22
Bulk epoxy	6.04	0.33
Interphase V1 (no chemical boning)	4.96	0.30
Interphase V2 (chemical bonding)	22.82	0.32

6.2.2 Simulation Results

The elastic properties of the microscale models are calculated using the homogenization approach presented in section 2.2.2. For this, the models are subjected to tensile and shear loads in all spatial directions. Before the ultimate results are presented, the influence of the BCs, the mesh size and the homogenization approach applied is addressed. This calibration is performed on a model consisting of 5 randomly distributed BNPs (comparable to Fig. 6.1 (a)) without interphases. Subsequently, the representativeness of the generated RVEs is investigated, before the influence of the elastic interphase properties, the particle weight fraction and the primary particle size is discussed.

Mesh Size Dependency

As stated before, because of the linear material applied, the results are assumed to show a minor mesh size dependency. Nevertheless, two significantly different meshes are generated and simulated in the following. The reference case has a relatively fine mesh with a maximum element edge length of 1 nm and approximately 25000 second-order tetrahedral elements. The other case has a considerably coarser mesh with a maximum element size of 5 nm and around 5000 elements. The meshes of both models are compared in Fig. 6.3.

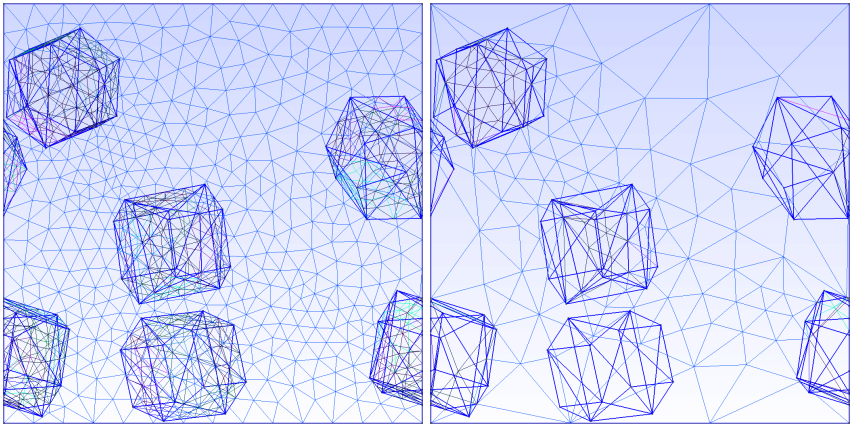

(a) (b)

Figure 6.3: Comparison of the two mesh sizes used in this section: (a) fine mesh with an element size l < 1 nm and 25000 elements and (b) coarse mesh with an element size l <5 nm and 5000 elements.

The resulting stiffness matrices calculated using periodic boundary conditions are presented in Eq. (6.2) for the reference case (fine mesh) and in Eq. (6.3) for the coarse case.

$$\mathbb{C}_{PBC,fine} = \begin{bmatrix} 9757.75 & 4776.96 & 4761.20 & -10.34 & -6.45 & 6.14 \\ 4776.97 & 9756.53 & 4770.23 & 1.15 & -5.96 & 3.01 \\ 4761.19 & 4770.20 & 9809.46 & 1.42 & 10.10 & -16.31 \\ -10.29 & 1.20 & 1.47 & 2494.51 & 3.77 & -6.59 \\ -6.45 & -5.97 & 10.09 & 3.77 & 2488.47 & -0.84 \\ 6.14 & 3.01 & -16.31 & -6.59 & -0.84 & 2497.02 \end{bmatrix} \quad (6.2)$$

$$\mathbb{C}_{PBC,coarse} = \begin{bmatrix} 9789.71 & 4778.07 & 4761.36 & -11.80 & -8.19 & 6.43 \\ 4778.08 & 9790.26 & 4772.86 & 1.39 & -6.92 & 3.37 \\ 4761.33 & 4772.82 & 9852.30 & 2.37 & 10.39 & -17.60 \\ -11.72 & 1.46 & 2.43 & 2511.21 & 4.16 & -7.67 \\ -8.19 & -6.92 & 10.39 & 4.16 & 2504.23 & -0.38 \\ 6.42 & 3.37 & -17.61 & -7.67 & -0.38 & 2514.01 \end{bmatrix} \quad (6.3)$$

The results confirm that the simulations are not very sensitive to the mesh size. Despite the much larger element size and the considerably lower number of elements, the stiffness matrices show only small differences. The maximum deviation of the normal components amounts to 0.68%, which is sufficiently small to accept the coarser mesh for all further simulations.

Choice of the Boundary Conditions

In section 2.2.2, different boundary conditions were discussed. Typically, the literature reports the most realistic prediction of the elastic properties using PBCs. However, for complex heterogeneous microstructures, PBCs can be difficult to realize, as, besides a periodic inner structure, a periodic mesh is desirable[1]. Furthermore, depending on the application (i.e. the compositions of the microstructure, the material of the constituent phases, etc.), the Voigt and Reuss bounds may be close to each other, making PBCs expendable [133]. Thus, in the following, the example model from the previous section is subjected to DBCs to investigate the necessity of PBCs in the scope of this thesis. The stiffness matrix for PBCs was already shown in Eq. (6.2). The resulting stiffness matrix for DBCs using the reference mesh is plotted in Eq. (6.4).

$$\mathbb{C}_{DBC} = \begin{bmatrix} 10881.67 & 4882.61 & 4898.84 & -7.99 & 3.44 & -4.76 \\ 4882.61 & 11247.21 & 4954.22 & 25.44 & -10.28 & -8.20 \\ 4898.84 & 4954.22 & 11862.09 & 6.95 & -15.50 & -23.79 \\ -7.99 & 25.44 & 6.95 & 3156.95 & -4.56 & -14.82 \\ 3.44 & -10.28 & -15.50 & -4.56 & 3121.07 & 1.40 \\ -4.76 & -8.20 & -23.79 & -14.82 & 1.40 & 3250.36 \end{bmatrix} \quad (6.4)$$

By comparing the matrices shown, considerable differences are evident. The maximum deviation of the normal components amounts to 17%, which is why DBCs are

[1] A periodic mesh is not obligatory since for non-periodic meshes the displacement fields can be interpolated. This, however, is highly complex in practical application and thus not further considered here

considered to be not accurate enough. Hence, PBCs are used for the homogenization from the micro- to macroscale for the rest of this thesis.

Choice of the Homogenization Method

As explained in section 2.2.2, the homogenized stress and strain of the microscale models are typically calculated as the volume average of the element stresses and strains (see Eq. (2.17)). Due to the presence of the RFAs in the agglomerate UCs in section 6.3.2, this approach cannot be used for these models. The RFAs represent air inside of the agglomerates and thus not a solid material. Hence, they are not meshed and stress and strain cannot be volume averaged for the whole model properly. It was shown in section 2.2.2 that the homogenized stress and strain can alternatively be expressed through the reaction forces acting on the box boundaries and the box deformation (see Eq. 2.18 and Eq. 2.19). This equivalence is shown in a practical application for the homogeneous RVEs in the following. Eq. (6.5) shows the stiffness matrix calculated using the alternative approach.

$$\mathbb{C}_{PBC,RF} = \begin{bmatrix} 9757.72 & 4776.94 & 4761.18 & -10.34 & -6.45 & 6.14 \\ 4776.94 & 9756.49 & 4770.20 & 1.15 & -5.96 & 3.01 \\ 4761.18 & 4770.20 & 9809.46 & 1.42 & 10.10 & -16.31 \\ -10.34 & 1.14 & 1.42 & 2494.51 & 3.77 & -6.59 \\ -6.45 & -5.96 & 10.10 & 3.77 & 2488.47 & -0.84 \\ 6.14 & 3.01 & -16.31 & -6.59 & -0.84 & 2497.02 \end{bmatrix} \tag{6.5}$$

The above stiffness matrix shows an outstanding agreement with the reference stiffness matrix (see Eq. (6.2)), which was calculated with the volume averaging approach. Thus, using the alternative approach is feasible for the calculation of the elastic properties of the agglomerate UCs in section 6.3.2.

Representativeness of the RVEs

The normal elements of the reference stiffness matrix from Eq. (6.2) have a maximum deviation of 0.64%. Thus, from here on, the material is assumed to be isotropic and the elastic constants are calculated as follows. Firstly, the Lamé constants are obtained by averaging the normal and shear components of the stiffness matrix according to

$$\mu = \frac{\mathbb{C}_{1212} + \mathbb{C}_{1313} + \mathbb{C}_{2323}}{3} \tag{6.6}$$

and

$$\lambda = \frac{\mathbb{C}_{1111} + \mathbb{C}_{2222} + \mathbb{C}_{3333}}{3} - 2\mu. \tag{6.7}$$

Therewith, the Young's modulus can be calculated as

$$E = \frac{\mu(3\lambda + 2\mu)}{\lambda + \mu} \tag{6.8}$$

and the Poisson's ratio is obtained from the relation

$$\nu = \frac{\lambda}{2(\lambda + \mu)}. \tag{6.9}$$

To receive meaningful elastic properties, it is important to check whether the applied VEs are representative of the real material. An RVE consists of a sufficiently large number of primary particles, to represent a statistically homogeneous particle distribution. To ensure this, VEs containing three, five and ten primary particles are simulated. The results are plotted in Fig. 6.4 (a). For each case, a statistically representative number of random realizations was investigated to ensure converged results, as exemplarily shown in Fig. 6.4 (b) for the RVEs containing ten primary particles. As can be seen in Fig. 6.4 (a), already for five primary particles, a reasonably converged Young's modulus is observed, as the difference from the ten particle case is only 0.29%. Since all of the presented cases require a rather low numerical effort, for the study shown in the following subsection, the RVEs containing ten primary particles are used. The advantage of this case is that already for 20 random realizations, the Young's modulus is sufficiently converged (see 6.4 (b)). For the five primary particle RVEs, with 60, approximately three times as many random realizations are necessary. In conclusion, for the following study 20 random realizations of the RVEs containing ten primary particles are used.

Elastic Properties of the Homogeneous RVEs

With the calibrated homogeneous RVEs, the dependence of the elastic properties on three main parameters is investigated, which are the elastic interphase properties, the particle weight fraction and the primary particle size. The simulation results are plotted in Fig. 6.5.

Fig. 6.5 (a) shows the influence of the interfacial bonding and the BNP weight fraction on the Young's modulus for the reduced primary particle size of 3 nm. In both interphase cases, an approximately linear relation is observed. For a low weight fraction of 1%, both cases are close to each other in the range of the bulk epoxy

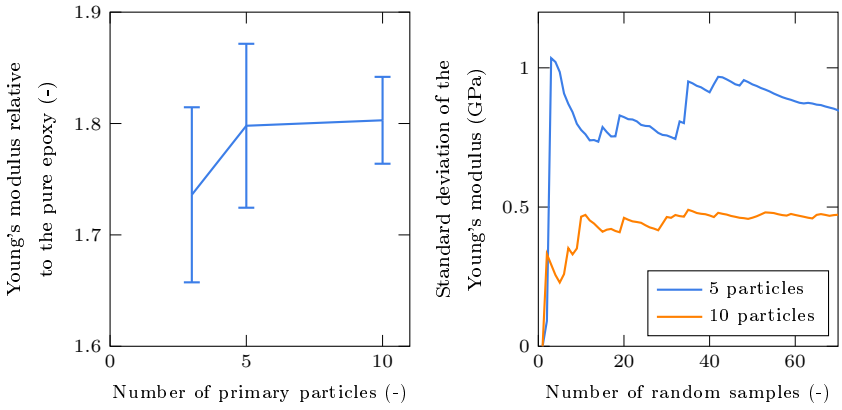

Figure 6.4: Numerical results of (a) the dependence of the Young's modulus on the number of primary particles per RVE and (b) the convergence behavior of the standard deviation for the RVE containing five and ten primary particles.

stiffness. With increasing weight fraction, the chemically bonded interphase (Layer V2) can unfold its potential and the gap between the two interphase cases increases. For the largest investigated weight fraction of 10%, the chemically bonded case is more than 70% stiffer than the unbonded case (Layer V1).

The influence of the interfacial bonding in combination with the primary particle size is shown in Fig. 6.5 (b) for a constant BNP weight fraction of 10%. The chemically bonded case (Layer V2) can be regarded as a demonstration of the nano-effect discussed in the introduction and illustrated in Fig. 1.2. With decreasing primary particle size, the specific surface area and thus the interphase volume increases. Hence, the high elastic properties of the interphase gain in influence and the effective NC properties increase. Though the influence is barely visible, the chemically unbonded case (Layer V1) shows exactly the opposite trend, as the effective Young's modulus of the NC slightly increases with increasing primary particle size. Similarly to the bonded case, for larger primary particles the interphase volume decreases and so does the influence of the interphase properties, which are lower than the bulk epoxy properties.

Generally, whenever a homogeneous primary particle distribution is present, a high BNP weight fraction, small primary particles and a chemical bonding between the particles and the polymer are beneficial for the elastic NC properties. As stated ear-

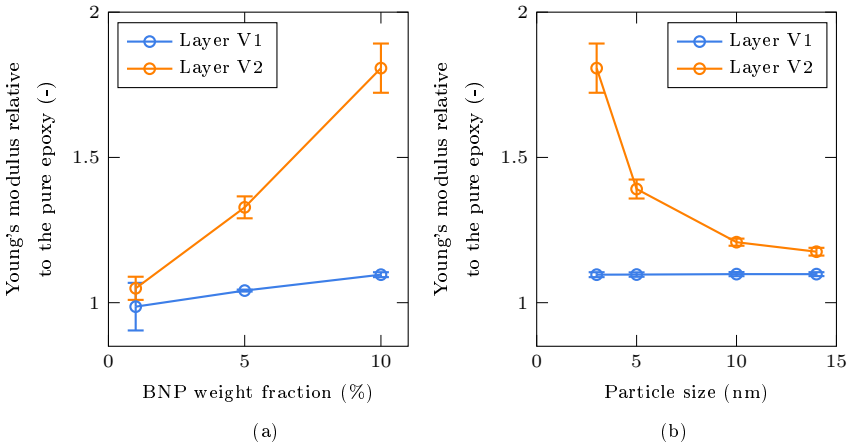

Figure 6.5: Young's modulus of the homogeneous RVEs (a) depending on the BNP weight fraction for a constant primary particle size of 3 nm and (b) depending on the primary particle size for a constant weight fraction of 10%.

lier, the investigated interphase cases represent extreme cases, so the shown curves provide upper and lower limits for the possible elastic NC properties. For a BNP weight fraction of 10%, the potential of the homogeneous primary particle distribution, and hence the NC, is estimated with an increase of the Young's modulus of approximately 80% compared to the unfilled epoxy. It should be noted that the extrapolation of the shown results to higher BNP weight fractions is prone to errors, since additional effects may become relevant. For instance, for higher weight fractions, the probability of particles that are located close to each other increases. This can reduce the amount of interphase volume or even unexpectedly influence the network formation of the polymer.

6.3 Agglomerate UCs

6.3.1 Modeling and Simulation Aspects

The generation of the agglomerate UCs is more complex than the one of the homogeneous RVEs. As stated in the introduction, the modeling of agglomerates is only rarely discussed in the literature. The only approach, which is specifically designed for agglomerates, was published by Pontefisso et al. [87]. This article presents a quite

complex and expensive algorithm for the generation of densely packed agglomerates. Of course, other literature about the generation of fiber-matrix RVEs with high volume fractions, such as the studies of Wongsto and Li [134] and Melro et al. [135], can be adapted to the generation of agglomerates. Here, a simpler hardcore algorithm is introduced, which is schematically illustrated in Fig. 6.6 (a) and as a flow chart in Fig. 6.6 (b). The first particle is always placed in the middle of the simulation box with a random orientation. To place the next particle, a sphere around the center of mass (CM) of the first particle is introduced. The algorithm tries to randomly rotate and place the second particle so that its center of mass (CM_i) is inside of the sphere. The particle can only be placed, if there is no intersection with the already existing particle. Otherwise, the new particle is removed and the process is repeated until the particle can be placed or a maximum number of iterations, n_{max}, is reached. If the particle could not be placed in n_{max} iterations, the radius r of the sphere is gradually increased by Δr, until it is possible to add the particle to the system. After placing the particle, the agglomerate is shifted, so that the center of mass of the agglomerate coincides with the center of the simulation box. Then, the whole process is repeated, until the desired number of primary particles i_{max} is reached.

The challenge of such an algorithm is to achieve a realistic distribution of the primary particles within the agglomerates. Since no experimental data concerning the inner structure of the agglomerates is available, a verification with the results from section 3.3.4 is striven for. There, the cumulative distribution function of the equilibrium distances of two neighboring particles was investigated employing MD simulations. The goal for the agglomerate generation is a good agreement between this probability distribution and the cumulative nearest neighbor distribution resulting from the agglomerate generator. To achieve this, the parameters of the algorithm presented above, mainly the number of tries for placing a particle while keeping the sphere radius constant, n_{max}, and the incremental increase of the sphere radius, Δr, are adjusted. Fig. 6.7 shows the comparison of the cumulative distribution function from section 3.3.4 (blue) and the ones from the agglomerate generator for two selected cases with different parameters (green and orange).

Fig. 6.7 shows that the algorithm needs a proper calibration to produce the correct particle distribution. As the comparison of the blue and green curves shows, with the wrong parameters, there is a large discrepancy between the cumulative distribution function from the MD simulations and the one produced with the agglomeration algorithm. However, the orange curve shows that it is possible to calibrate the algorithm so that a good agreement between MD and FEM is achieved. The parameters, with which the orange cumulative distribution function was produced, are n_{max}=12 and Δr=0.12*r.

After placing the particles, there are two possibilities for the further model generation, which are invoked depending on whether the model shall contain RFAs or not.

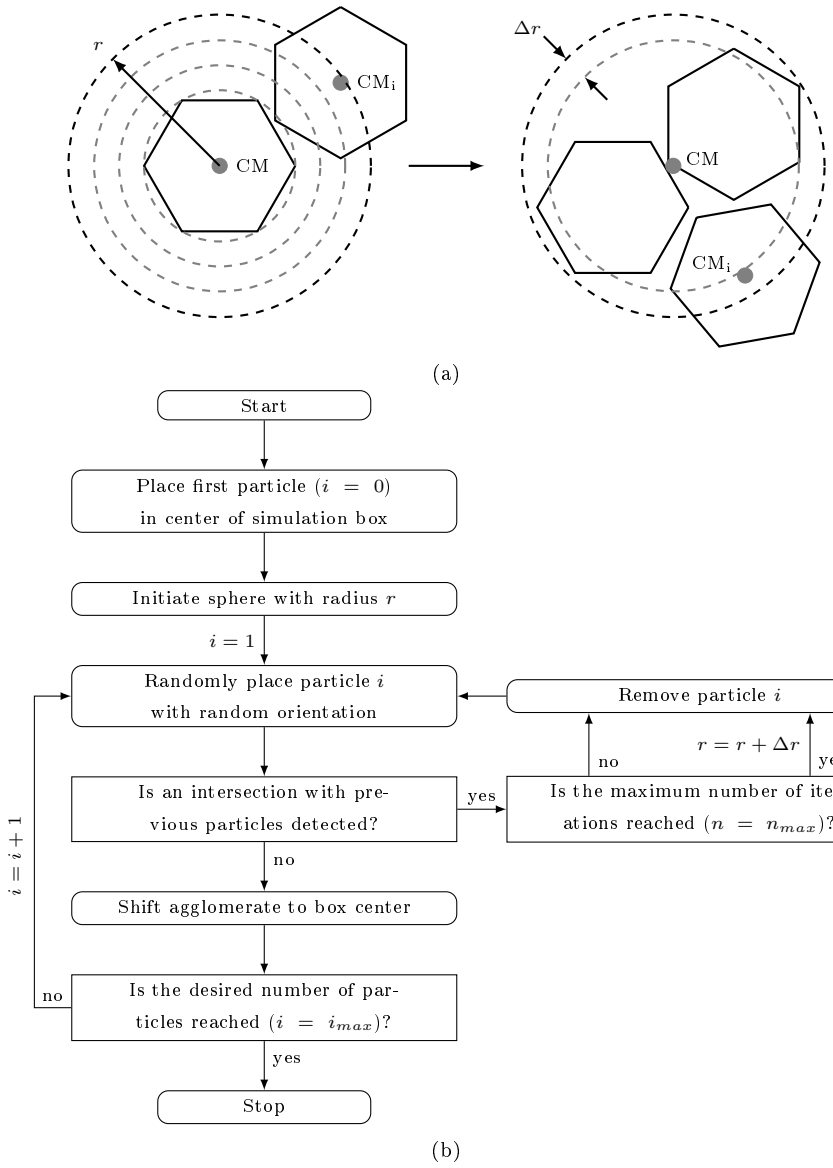

Figure 6.6: Agglomerate generation: (a) schematic illustration and (b) flow chart.

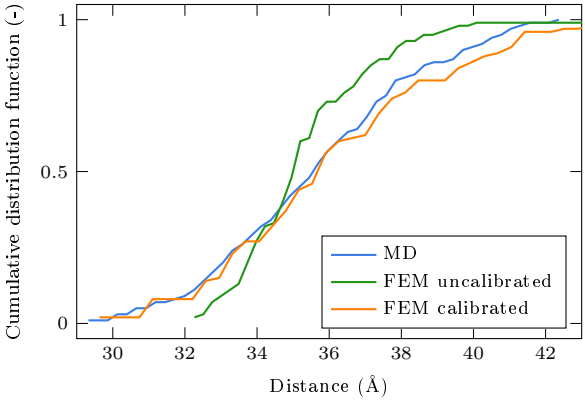

Figure 6.7: Comparison of the cumulative distribution functions of the equilibrium distances from the MD simulations from chapter 3 and the FEM model generation.

If no RFAs are present, the remaining model generation is similar to the homogeneous RVEs. In this case, the interparticulate interactions within the agglomerates play a minor role, but the interaction with the polymer dominates. After placing the particles, the interphases are generated. Of course, the interphases will overlap, which is the main difference to the homogeneous RVEs and the effect of interest in these models. The resulting reduction of the overall interphase volume leads to a dependence of the elastic properties of the agglomerate UC on the number of primary particles. If no RFA is present, the elastic properties applied for all constituents are similar to the homogeneous RVEs, as presented in Tab. 6.2.

In case an RFA area is present, a DEM-like approach is introduced to describe the interparticulate interactions inside the agglomerates. Therefore, the particles are cut out of the simulation box and a reference point is introduced for each primary particle. If the respective particle is in the outer region of the agglomerate and has an interface to the polymer, the reference point is coupled to the polymer through a kinematic coupling. Additionally, spring elements, whose behavior is modeled with the force-displacement curves from section 3.3, are introduced between each pair of particles or, to be precise, between each pair of reference points representing the particles. By replacing each particle with a reference point, the particles are treated as rigid bodies. This simplification is justified, since on the one hand the deformation of the particles is included in the force-displacement curves, which describe the interparticulate interactions, and on the other hand considerable deformations were not observed in the simulations from section 3.3. The interphases are created

similarly to the other models presented in this chapter. The generation of the RFAs is not trivial since, again, there is no experimental data about their existence and their possible geometry available. Generally, because of these uncertainties, the whole model generation process is designed in a modular way, so that details, such as the generation of the RFAs, can be updated whenever new insights are available. The approach for generating the RFAs in the scope of this thesis is schematically illustrated in Fig. 6.8. For each vertex of each primary particle, the distance to the agglomerate center of mass is determined. Then, the convex hull is calculated, considering only the n_{vert} (e.g. three) vertices of each particle, that are closest to the agglomerate center of mass. The resulting convex hull is cut from the models, leading to an empty, non-meshed region representing the RFAs. The influence of the n_{vert} parameter on the RFA volume fraction and the elastic properties of the agglomerate UCs is shown later.

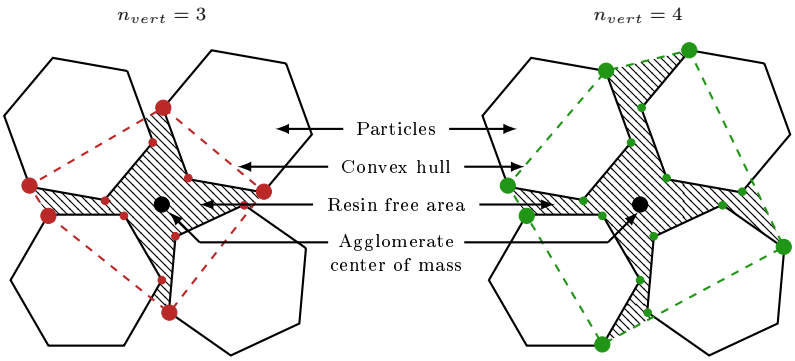

Figure 6.8: Schematic illustration of the modeling of the RFAs. The colored dots mark the n_{vert} vertices of each particle, which are closest to the agglomerate center of mass. The small colored dots are located inside of the convex hull.

An exemplary agglomerate UC model is plotted in Fig. 6.9 (a). All agglomerate UCs are generated with a periodic mesh, as shown in Fig. 6.9 (b). This is much easier compared to the homogeneous RVEs since by partitioning the outer surfaces of the UCs appropriately the Abaqus meshing tool is capable of generating the desired periodicity. In all remaining points, the agglomerate UCs accord with the homogeneous RVEs.

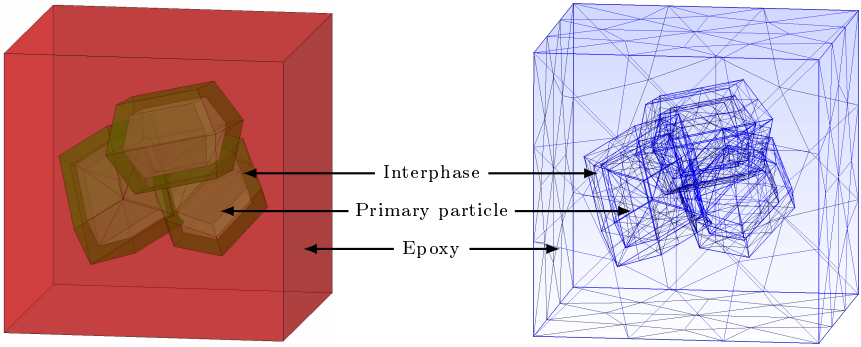

Figure 6.9: Illustration of (a) an exemplary model and (b) an exemplary FE mesh of an agglomerate UC with three primary particles.

6.3.2 Simulation Results

The simulations of the agglomerate UCs are largely based on the findings from the homogeneous RVEs. This concerns, for instance, the choice of the PBCs and the used mesh size. The homogenization of the elastic properties of the agglomerate UCs is performed with the alternative approach using the reaction forces and simulation box deformations instead of the volume-averaged stress and strain. Similar to the homogeneous RVEs, for each case shown in the following, a statistically representative number of random realizations is simulated, so that the standard deviations converge (compare Fig 6.4 (b)).

Influence of the n_{vert} Parameter

Before the influence of the interfacial bonding and the agglomerate size on the Young's modulus of the agglomerate UCs is discussed, the n_{vert} parameter, which determines the size of the RFA, is addressed. The graph shown in Fig. 6.10 (a) indicates that an almost linear dependence of the RFA volume fraction on the n_{vert} parameter exists. Moreover, the volume fraction and its slope increase with an increasing number of primary particles per agglomerate. This effect is expected since the ratio of agglomerate volume to agglomerate surface increases with increasing agglomerate size. In other words, bigger agglomerates contain a larger cavity volume, can lead to a higher RFA volume fraction.

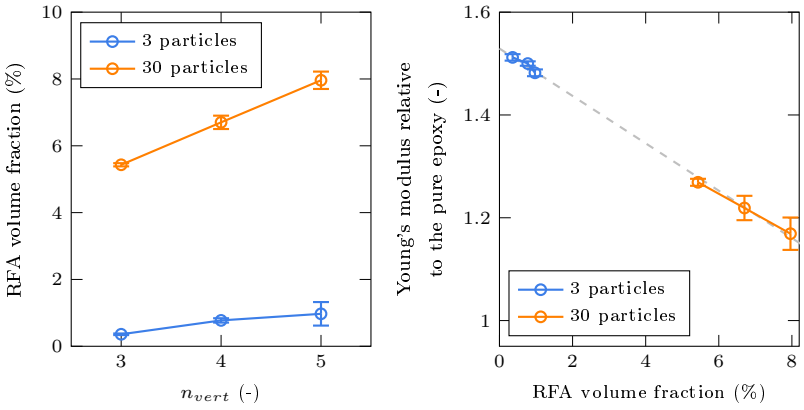

Figure 6.10: Numerical results of (a) the RFA volume fraction in dependence on the n_{vert} parameter and the number of primary particles per agglomerate and (b) the Young's modulus of the agglomerate UCs in dependence on the RFA volume fraction and the number of primary particles per agglomerate.

The influence of the RFA volume fraction on the Young's modulus of the agglomerate UCs is shown in Fig. 6.10 (b). As indicated by the dashed gray line, again, a linear relation is observed. The blue curve represents an agglomerate consisting of three primary particles. Since for small agglomerates the RFA volume fraction is generally small, with a maximum difference of 3% a low influence on the Young's modulus is observed. With increasing agglomerate size, the RFA volume fraction increases and thus the Young's moduli are significantly influenced by both the presence and the amount of RFA. The largest of the investigated values, $n_{vert} = 5$, leads to a reduction of the Young's modulus by 600 MPa compared to $n_{vert} = 3$, which is a percentage of approximately 10%.

Due to the lack of experimental data, the choice of the n_{vert} parameter is ambiguous. In the following, a conservative value of $n_{vert} = 3$ is used. The results shown in the following section indicate that this choice still tends to underestimate the experimental Young's moduli and hence overestimate the RFA volume. The results presented in the following can thus be understood as a lower bound to the elastic properties if the agglomerate UCs.

Influence of the Interphase, the RFA and the Agglomerate Size

Ultimately, in this section, the influence of three main factors on the elastic properties is investigated, which are the interfacial bonding, the number of primary particles per agglomerate and the presence of an RFA. The results are collectively shown in Fig. 6.11.

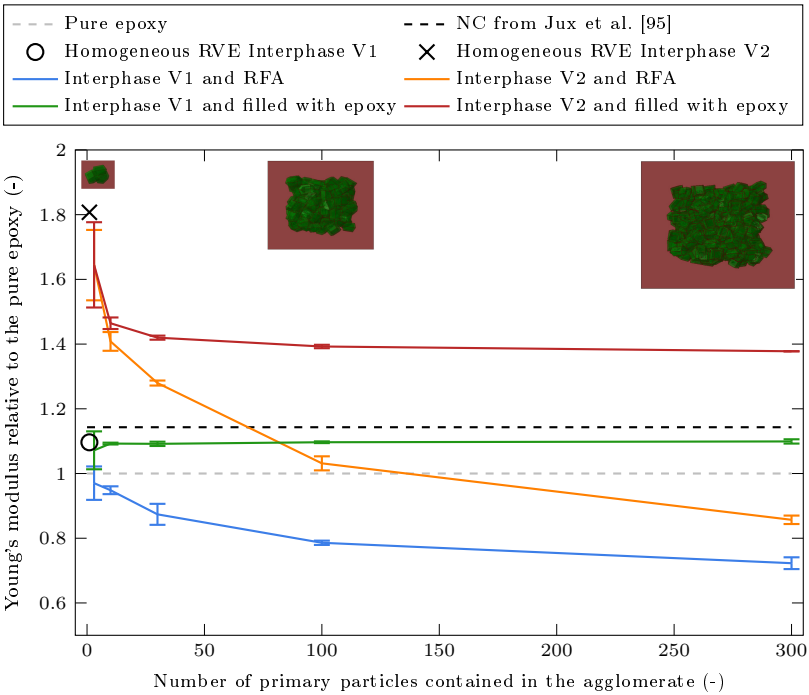

Figure 6.11: Dependence of the Young's modulus of the agglomerate UCs on the number of primary particles per agglomerate, the interfacial bonding and the existence of an RFA.

To understand the discussion presented in the following, some facts should be noted. Firstly, all models contain a fixed BNP mass fraction of 10%. Hence, the size of the agglomerate UCs increases with an increasing number of primary particles, as illustrated in Fig. 6.11. Secondly, for each data point shown in Fig. 6.11, a statistically representative number of samples was simulated, until the standard deviation converges, comparable to Fig. 6.4 (b). This is because, in contrast to e.g. fiber matrix UCs, the agglomerate UCs have a random inner structure. Thirdly, the

convergence of the Young's moduli in Fig. 6.11 should not be misinterpreted as an increasing representativeness of the UC (as it was presented for the homogeneous RVEs, compare section 6.2.2). Using a UC approach implies that the real material consists of a periodic repetition of the UC. Thus, the investigated UCs represent a NC containing only one specific agglomerate size. Since this is not the case for real NCs, agglomerate RVEs are simulated in the following section. Instead, the observed convergence results from the inner structure of the UCs, as discussed in detail in the following. Lastly, the comparison to the experimental results reported by Jux et al. [95] is of qualitative nature. This is because of the difficult calibration and large deviations between the simulations and the experiments of the bulk epoxy from chapter 4. Thus, all results are normalized to the bulk epoxy stiffness (gray dashed line). The dashed black line represents the percentage increase of the Young's modulus observed in the experiments. Generally, for a proper comparison of the simulation results to the experimental values, the agglomerate size distribution should be taken into account, as shown in the following section.

Fig. 6.11 illustrates the influence of the interfacial bonding, the RFA and the agglomerate size on the Young's modulus of the agglomerate UC. For comparison, experimental values for the pure epoxy and the NC from [95] are shown. The average agglomerate size from the experimental study can be found at the far right of the diagram at around 300 primary particles. In principle, two major effects are observed. Firstly, ignoring the RFAs and only taking into account the red and the green curves, the influence of the reduction of the interphase volume with an increasing number of primary particles is visible. This effect is caused by the closely located primary particles and the resulting overlap of the interphases. The green curve (Interphase V1, no chemical bonding) is almost independent of the number of primary particles per agglomerate. This is because the interphase stiffness is close to the bulk epoxy stiffness and hence the reduction of the overall interphase volume plays a minor role. The red case (Interphase V2, strong chemical bonding), in contrast, shows a significant decrease in the UC stiffness with an increasing number of primary particles per agglomerate. The interphase is much stiffer than the bulk epoxy and thus the reduction of the interphase volume has a significant influence. As expected, the percentage reduction of the interphase volume converges with increasing agglomerate size, which leads to the converging Young's moduli observed for the red curve.

Secondly, comparing the blue and the orange curves, an overlayed effect caused by the presence of the RFA is observed. As explained before, with increasing agglomerate size, the volume fraction of the RFA increases. This leads to a higher amount of weakly interacting inner surface where the particles are not bordering with polymer and the weak interparticulate interactions dominate. This results in a considerable reduction of the Young's moduli of the agglomerate UCs for both interphase cases. Even for comparatively small agglomerates with less than 150 primary particles, the stiffness of both cases drops below the bulk epoxy modulus.

So far, the chemically unbonded case with filled agglomerates (green curve) provides the best approximation of the experimental NC response. However, as stated before, a comparison between simulations and experiments is postponed to the following section, since the agglomerate size distribution is not included here. Still, three recommendations for the optimization of the elastic NC properties can be derived from the results shown. As expected, an enhanced interfacial bonding between the reinforcement phase and the polymer leads to a higher Young's modulus. Furthermore, except for the chemically unbonded case filled with polymer (green curve), a finer dispersion of the agglomerates results in a higher stiffness. This is supported by the shown results of the homogeneous RVEs, which possess the highest Young's moduli and can be considered as an ideal dispersion. Last but not least, as long as a homogeneous distribution of primary particles cannot be realized in reality, it is beneficial to ensure that agglomerates are filled with polymer to obtain the best elastic properties.

6.4 Agglomerate RVEs

In reality, NCs do not contain only one specific agglomerate size, but an agglomerate size distribution. To consider this, in this section agglomerate RVEs are investigated as the ultimate outcome and the highest level of the proposed multi-scale framework. The model generation and the respective simulation results are presented in the following.

6.4.1 Modeling and Simulation Aspects

Again, the generation of the agglomerate RVEs is largely based on the modeling of the homogeneous RVEs presented in section 6.2.1 and only differences are discussed here. In principle, no particles or agglomerates are modeled anymore, but the agglomerate RVEs consist of a homogeneous distribution of agglomerate UCs, as can be seen in Fig. 6.12 (a) and (b). The first step in the model generation is the determination of the agglomerate sizes contained in the RVE based on the experimental agglomerate size distribution, which is shown in Fig. 6.12 (c). This agglomerate size distribution is nothing but a probability distribution of agglomerate sizes, which is used as an input to determine the agglomerate size distribution of the RVEs. Three example choices for RVEs containing 20 UCs are shown in Fig. 6.12 (d). With the known agglomerate sizes, the size of the UCs and the RVE can be calculated. The material parameters of each UC are interpolated or extrapolated from the results shown in Fig. 6.11 using a logarithmic function.

The RVEs presented here demand for a lower BNP mass fraction than the underlying UCs. This is because it is impossible to fill the RVE volume only with UCs and at

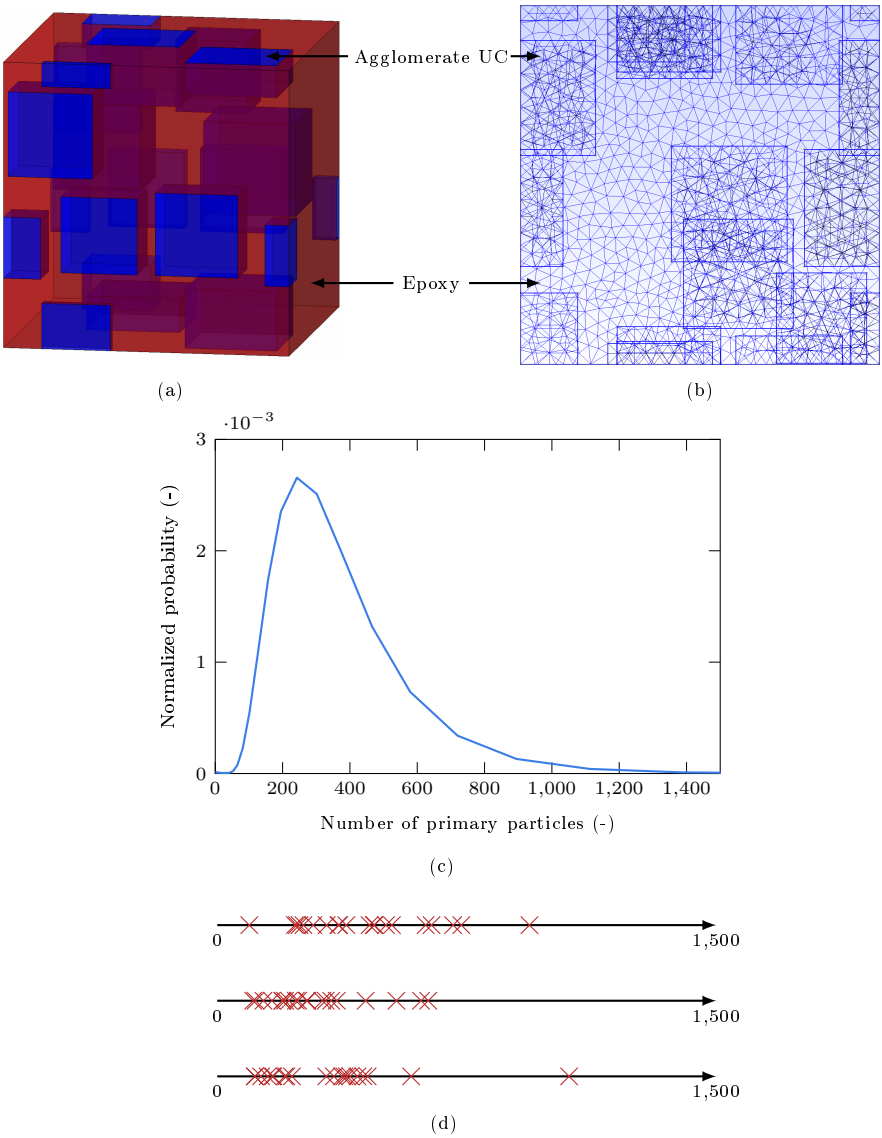

Figure 6.12: Illustration of (a) an exemplary model and (b) an exemplary FE mesh of an agglomerate RVE, (c) the normalized agglomerate size distribution [109] and (d) three example distributions for agglomerate RVEs consisting of 20 UCs.

the same time satisfy the agglomerate size distribution. Hence, it is recommendable to use the highest possible mass fraction in the agglomerate UC simulations. In the scope of this thesis, the UCs presented above were modeled with a weight fraction of 10%. For the generation of the agglomerate RVEs, a simple hardcore algorithm is used for randomly placing the UCs into the RVE starting with the largest UC. This algorithm is capable of generating RVEs with a mass fraction up to around 4.5%. However, to be able to compare the simulation results to experimentally measured values, the mass fraction of the RVEs is chosen to be 2.5%. As an extension of the work presented here, the framework can be equipped with a more advanced algorithm, which allows for the generation of models containing higher BNP mass fractions.

The remaining model generation is similar to the homogeneous RVEs, including the choice of PBCs and the chosen mesh size. To obtain a periodic mesh, Gmsh [132] is used.

6.4.2 Simulation Results

Representativeness of the Agglomerate RVEs

Similar to the homogeneous RVEs, it is necessary to study the representativeness of the generated RVEs to obtain meaningful results. Therefore, agglomerate RVEs with an increasing number (i.e. 1, 3, 5, 10 and 20) of agglomerate UCs are investigated. For each case, a statistically representative number of random samples is simulated, so that the standard deviation converges. The dependence of the simulated Young's modulus on the number of UCs per RVE is plotted in Fig. 6.13 (a). Using one UC per RVE leads to a slight underestimation of the Young's modulus and to a large standard deviation. Already for five UCs per RVE, a converged Young's modulus is obtained, as the difference to the RVE containing ten UCs is only 0.02%. Similar to the homogeneous RVEs, the simulations presented here require a quite low numerical effort. Hence, in the following, RVEs containing ten UCs are used. Fig. 6.13 (b) shows the convergence of the standard deviation of the Young's modulus for these RVEs. A sufficient convergence is observed for 20 random realizations, which are used to obtain representative results in the following.

Influence of the Interphase and the RFA on the elastic properties of Boehmite/Epoxy NCs

The results presented in this section are the ultimate outcome of the multi-scale framework presented in this thesis. Four cases are investigated in the following, which are the two interfacial bonding cases (Interphase V1: chemically unbonded and Interphase V2: chemically bonded) and for each interphase case the two RFA

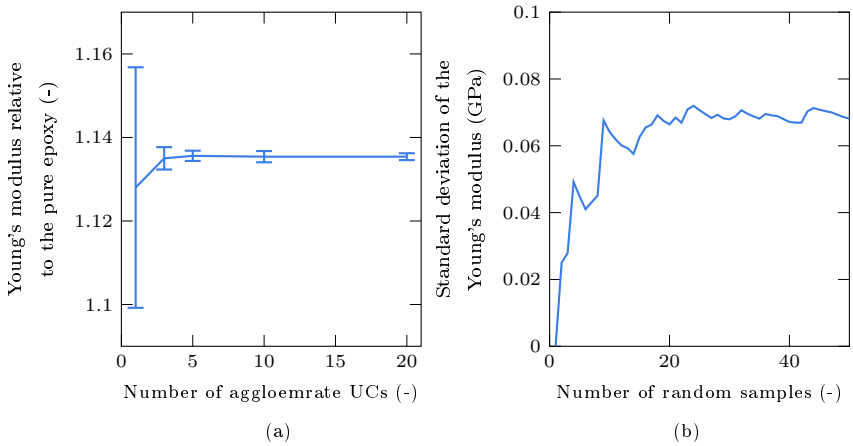

Figure 6.13: Numerical results of (a) the dependence of the Young's modulus on the number of agglomerate UCs per RVE and (b) the convergence behavior of the standard deviation for the RVE containing 10 UCs.

cases (with RFA (i.e. unfilled) and without RFA (i.e. filled with polymer)). The normalized Young's moduli of all four cases are presented in Fig. 6.14. For comparison, the experimental results for the pure epoxy and the NC with a BNP weight fraction of 2.5% are shown.

Several conclusions can be drawn from Fig. 6.14. The two interphase cases without an RFA lead to a percentage increase of the Young's modulus compared to the bulk epoxy of 1.5% and 5.9% for Interphase V1 and Interphase V2, respectively. The best prediction of the experimentally measured NC properties is provided by the chemically unbonded case (Interphase V1) without an RFA, which shows a deviation from the experiments of approximately 0.6%. It should be kept in mind that the numerical results were simulated for a reduced primary particle size of 3 nm, whereas the experiments were obtained for a primary particle size of 14 nm. Despite the discrepancy in primary particle size, a comparison of the Interphase V1 case is meaningful, as a negligible dependence of the Young's modulus on the primary particle size was found in section 6.2 (compare Fig. 6.5 (b)). Since the experimental results suggest a slightly higher Young's modulus than the simulations, a certain chemical bonding between the BNPs and the epoxy can be expected in the real material. An evaluation of the exact amount is challenging, since a second effect, the existence and extent of the RFA, is overlayed. Though the RFA for both interphase cases leads to considerably reduced Young's moduli compared to the bulk epoxy and a drastic underestimation of the stiffness, its existence cannot be ruled

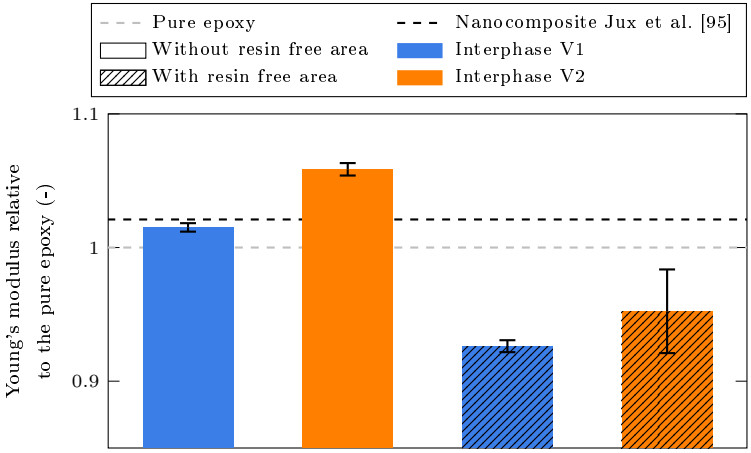

Figure 6.14: Dependence of the Young's modulus of the agglomerate RVEs on the interphase case and the presence of an RFA.

out completely. It should be kept in mind that the RFA, as it is modeled in the scope of this thesis, almost covers the whole agglomerate. Thus, the simulations should result in a lower bound. It is imaginable that a smaller RFA around the core of the agglomerate exists. To take this into account, in future work, the framework could be equipped with a more realistic RFA modeling approach. Generally, as a guideline for the development of NCs, it is particularly important to ensure that agglomerates are filled with polymer to obtain the best elastic properties. Furthermore, by improving the chemical interactions between the BNPs and the epoxy, an increase of the elastic properties of up to 6% can be reached, which is almost three times the current experimental value.

To further demonstrate the potential of the NCs, the influence of the agglomerate size distribution on the Young's modulus for a constant weight fraction of 2.5% is shown in Fig. 6.15 (a). Only the two cases without the RFA are plotted, since they predict the most realistic results. To generate the underlying models, the experimental agglomerate size distribution (compare Fig. 6.12 (c)) was scaled to smaller or larger mean agglomerate sizes. From the graph in Fig. 6.15 (a), it can be seen that the chemically unbonded case (Interphase V1) shows an almost constant Young's modulus independent of the agglomerate size. For the chemically bonded case (Interphase V2), in contrast, the Young's modulus increases with decreasing agglomerate size. For agglomerate sizes above 100 nm, the influence is small and the simulations predict an almost converged Young's modulus. This is quantitatively in agreement with the experiments from section 6.1. A qualitative comparison of the

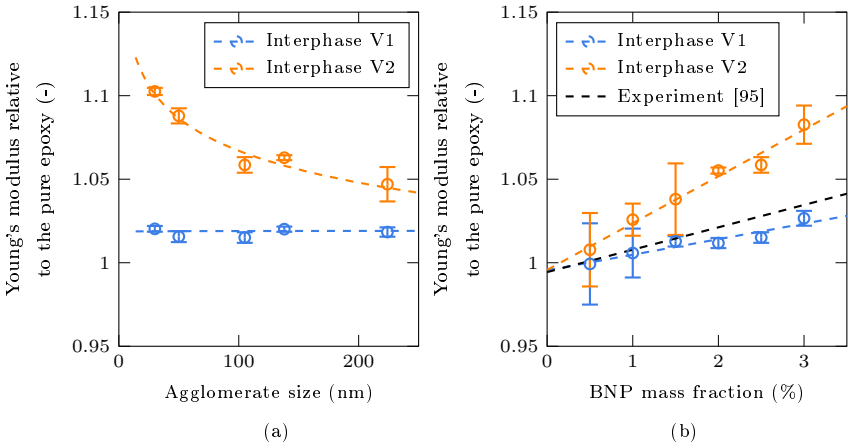

Figure 6.15: Numerical investigation of the influence of (a) the mean agglomerate size on the Young's modulus for a mass fraction of 2.5% and (b) the BNP mass fraction on the Young's modulus for a mean agglomerate size of 105 nm.

results is impossible because of the different BNP mass fractions in the experiments and the simulations. For agglomerates smaller than 100 nm, a significant increase of the Young's modulus is observed. A size of 14 nm, which is the primary particle size and hence corresponds to an ideal dispersion, yields a percentage increase of the Young's modulus of 12.3% compared to the bulk epoxy. This is more than twice the increase of the 105 nm mean agglomerate size with the same weight fraction. Furthermore, it is in the same range as the experimental result of the 105 nm agglomerate size with a weight fraction of 10%.

The unused potential is further underlined by the influence of the BNP weight fraction on the Young's modulus, as shown in Fig. 6.15 (b). An approximately linear dependence is observed for both interphase cases. The comparison to the fit of the experimental measurements demonstrates that the lower bound, the Interphase V1 case, provides a better approximation. The extrapolation of the curves to a weight fraction of 10%, which might be interesting for real technical applications, results in a percentage increase of the Young's moduli of 8.9% and 27.6% for the chemically unbonded case and the chemically bonded case, respectively. For comparison, the experiments yielded an increase of 12.5%. It can be concluded that the NC contains a large unused potential, as with an improved interfacial bonding, the percentage increase of the elastic properties can be doubled.

6.5 Conclusions

In this chapter the highest level of the multi-scale framework, the microscale, was presented. The results and findings from the previous chapters were assembled to RVEs containing homogeneously distributed primary particles, agglomerate UCs and agglomerate RVEs.

With the homogeneous RVEs, the influence of the interfacial bonding, the BNP weight fraction and the size of the BNPs was examined for an ideally dispersed system. It was found that a chemical interaction between the BNPs and the epoxy leads to higher elastic properties compared to the unbonded case. With increasing BNP weight fraction and decreasing primary particle size, the chemical bonding and the resulting stiff interphase can unfold their potential. For a weight fraction of 10% and a primary particle size of 3 nm, an increase of the Young's modulus of approximately 81% compared to the bulk epoxy was achieved. For comparison, the chemically unbonded case results in an increase of around 10% for the same weight fraction and primary particle size.

The real material contains agglomerates. Hence, the results of the homogeneous RVEs are not representative of the NC and agglomeration was introduced into the microscale models. This comprises the modeling of the agglomerates themselves and the consideration of the agglomerate size distribution and a possible RFA. The comparison of the results of the agglomerate RVEs to the experimental study revealed that the chemically unbonded case without an RFA provides the best approximation of the experimental results. The simulation results of this case are slightly softer than the experiments, which is why a certain interfacial bonding between the BNPs and the epoxy in reality is likely. A conclusive statement can, however, not be made, since the two effects of the interfacial bonding and the RFA volume fraction are overlayed. The assumptions concerning the RFA made in the scope of this thesis certainly overestimate the RFA volume fractions and hence underestimate the NC Young's modulus. Still, it is imaginable that a small RFA around the core of the agglomerates exists. For instance, it is possible that the assumptions of the chemically bonded case (Interphase V2) are correct and the existence of a small RFA reduces the elastic Young's modulus to the experimentally measured one.

With the given input, assumptions and validation possibilities, the framework can provide upper and lower bounds to the elastic properties of the BNP/epoxy NC. Furthermore, the chemically unbonded case without an RFA leads to a reasonable prediction of the experimentally obtained values. Still, related to the above discussion, an exact calibration of all underlying effects cannot be assured yet. Future research should focus on establishing more sophisticated validation possibilities along with the whole framework. An example concerning the work presented in this chapter would be the experimental determination of the existence and the possible extent of an RFA.

7 Summary, Conclusions and Outlook

7.1 Summary and Conclusions

In this thesis, a multi-scale framework for the prediction of the elastic properties of NCs has been proposed, which incorporates effects related to the interphase formation between NPs and the surrounding polymer and agglomeration. The elastic properties of each constituent, namely the BNPs, the epoxy and the interphase region, and the interparticulate interactions have been calculated and homogenized on the atomistic level and passed to the higher scale. On the micro-level, the input from the atomistic simulations was assembled and continuum models were developed, which contain homogeneous particle distributions or agglomerates.

Experimental AFM measurements conducted by the colleagues from the BAM revealed large deviations of the elastic properties of boehmite compared to the literature. To understand the cause of the differences, a new MD simulation-based approach was introduced, which mimics the AFM testing conditions. The obtained Young's moduli of the perfect boehmite crystal under multiaxial compression load amounted to 232, 136 and 267 GPa in x-, y- and z-direction. Generally, the behavior of crystalline materials is mostly brittle and hence elastic until failure. However, depending on the loading direction, an additional inelastic deformation mechanism was found for the BNPs embedded in the polymer matrix. The slippage of the physically interacting boehmite sheets significantly reduces the Young's modulus to values in the range of 30 - 40 GPa. It furthermore causes a highly inelastic behavior, which can partly be reversed, e.g. by restoring forces introduced by the AFM tip during the retraction or by the far filed lattice structure of the boehmite. The inelastic slippage particularly affects small crystals, such as the investigated primary particles. However, MD based tensile tests of NC UCs showed that slippage of the boehmite sheets is not expected under tensile or shear load in the elastic regime. This is because of the much weaker load transfer from the epoxy to the BNPs, compared to the direct loading introduced by the AFM tip.

The interparticulate interactions, which are needed for the simulation of the unfilled agglomerates on the microscale, were determined through statistical numerical tension, compression and shear tests between two randomly orientated particles. From these simulations, force-displacement curves under tension and compression were recorded. The shear behavior was found to be almost frictionless and was neglected

in the microscale simulations. Similar to the MD based tensile tests of the NC UCs, no significant deformation of the particles was observed under tension and compression load.

The second phase, the epoxy, was characterized using numerical tensile and shear tests. The literature lacks a comprehensive MD based investigation of epoxy polymers and leaves many points open or reports inconsistent results. Thus, the influence of different parameters, such as the strain rate, the network structure and the chosen force field parameters, was studied. All the investigated effects and parameters showed a considerable influence on the elastic properties of the polymer. Thus, a proper calibration of the epoxy models with the given experimental data is unfeasible. For the subsequent work presented throughout the thesis, the elastic properties of the reference system ($E = 6.07$ GPa, $\nu = 0.324$) were used, even though they show large deviations from the experimentally measured epoxy stiffness. From the authors' perspective, a systematic study, both experimentally and numerically, is indispensable to improve the understanding of the polymer. It should especially be focused on establishing validation possibilities, with which a more direct assessment of the modeling assumptions is possible. This, in turn, is crucial for a proper investigation of related effects, such as the interphase formation.

The BNP/epoxy interphase was investigated employing the previously introduced AFM simulations. For the chemically unbonded case, no interphase was found and an undisturbed epoxy network could form almost until the phase boundary. With enabled chemical bonding between the BNPs and the polymer, an alteration of the epoxy network was observed, which led to a reduced interphase stiffness compared to the bulk polymer. The AFM simulations have a major drawback when used for multi-phase materials since close to the phase boundary the measurement of mixed moduli is inevitable. Thus, a method for the direct calculation of the local elastic properties from MD simulations was developed and used for the determination of the BNP/epoxy interphase properties. The investigation of two extreme cases revealed a significant influence of the interfacial bonding between the BNP and the epoxy on the elastic properties. In case the BNPs do not chemically react with the epoxy, the interphase is only caused by the repulsion between boehmite and epoxy due to the physical interactions. The resulting interphase has a thickness of 5 Å and an effective interphase stiffness of approximately 4.96 GPa, which is a reduction of 17% compared to the bulk epoxy. If a strong chemical bonding is present, the interphase is additionally characterized by a significantly altered polymer network. In this case, with a thickness of 15 Å, the interphase is three times as thick and has an effective Young's modulus of 22.82 GPa, which is an increase of 275% compared to the bulk epoxy stiffness.

Ultimately, the previous results and findings were assembled to continuum models with homogeneously distributed BNPs or agglomerates. The potential of the NCs is indicated by the investigation of the RVEs consisting of homogeneously distributed

BNPs in the epoxy matrix, which represent an ideal dispersion. For the real primary particle size of 14 nm and a weight fraction of 10%, an increase of the Young's modulus of approximately 18% is possible, if BNPs and epoxy are chemically bonded. Further improvements up to an increase of 81% can be achieved using smaller primary particles with a size of 3 nm. Agglomeration reduces the elastic properties of the NC. This is mainly because of the reduction of the overall interphase volume if primary particles are closely located inside of the agglomerates. Also, the presence of an RFA can considerably lower the elastic properties. However, for BNP/epoxy NCs it plays a minor role and, if at all, can be expected to affect only a small region of the agglomerate. The best prediction of the experimentally measured Young's modulus is observed for the chemically unbonded case without an RFA. Since the experiments are slightly stiffer, a certain chemical bonding can be expected in the real material. Since two overlayed effects, the interfacial bonding and the RFA, are present, an exact quantification cannot be performed with the given results.

With the available input, assumptions and validation possibilities, the presented framework can provide upper and lower bounds to the elastic properties of BNP/epoxy NCs. Even more, with the chemically unbonded case without an RFA, a reasonable prediction of the experimentally measured Young's modulus could be achieved. In the following section, possible improvements and extensions are discussed.

7.2 Outlook

According to the previous explications, three main research areas can be identified for future work.

7.2.1 Validation of the Proposed Approach

A weak spot of the work presented in this thesis is the deficient validation. This is on the one hand because of the large scale separation between the experiments and simulations, concerning both the time and length scales. For instance, macroscopic tensile tests typically have a spatial extent of several millimeters and a strain rate of around 10^{-4}. The MD simulations, in contrast, use a simulation box size of several nanometers and a strain rate in the range of 10^{7} to 10^{9} 1/s. On the other hand, mainly due to the small spatial extent of the involved phases, there simply exist no experiments that can capture the desired properties or characteristics with a sufficient resolution. An example is the altered epoxy network structure of the interphase in the presence of the boehmite particles, which cannot be directly experimentally measured.

As previously discussed, the literature leaves the influence of a strain rate dependence of the elastic properties of the epoxy open. Hence, an indirect validation of

the model generation of the epoxy through the comparison of the Young's modulus or other thermomechanical properties is unfeasible. At the same time, a direct comparison of the network structure of the models and the real material is impossible because of experimental limitations. From the authors' point of view, new validation possibilities are indispensable. An attempt to validate the model generation was made by Unger et al. [125], who validated the curing kinetics of epoxy with experimental near-infrared spectroscopy measurements. However, due to the chemical composition, this approach does not apply to the epoxy system used throughout this thesis. Further developments concerning a direct comparison of the molecular structure of the atomistic models and the real material can help to significantly enhance the understanding of the polymer and improve the calibration of the models. Another possible approach is the comprehensive experimental investigation of the influence of the strain rate on the elastic properties of epoxy. Furthermore, the application of coarse-graining methods [136–138] can help to reduce the time scale gap between experiments and simulations and to further study the influence of the strain rate on the elastic properties of epoxy numerically.

The uncertainties concerning the modeling of the epoxy stretch through large parts of the presented work since e.g. the determination of the interphase properties on the atomistic scale relies on an adequate modeling of the polymer. Other open points in the experimental literature concern, for instance, the thickness, molecular structure and elastic properties of the interphase, the interaction between the primary particles and the question whether the agglomerates are filled with polymer or not.

7.2.2 More Realistic Modeling

The proposed framework is a considerable step forward from the state of the art towards a more realistic numerical modeling and simulation of NCs. Still, there are possibilities to further improve the approach, which, in large parts, go hand in hand with the discussions about the validation in the previous section. Some known issues, that could be addressed, are described in the following. Improved validation possibilities will certainly reveal additional potential for future research.

One aspect, which should be further studied is the formation of the interphase inside of the agglomerates. It was discussed earlier that the assumption of effective interphase properties in combination with the reduced interphase volume inside of the agglomerates might be overly simplified. A possible idealized approach to address this issue was discussed in the concluding section of chapter 5. By inverting the layered models and simulating an epoxy film of varying thickness surrounded by two boehmite layers, the situation inside of an agglomerate could be mimicked. Furthermore, coarse-graining methods can help to simulate small agglomerates in a molecular resolution and act as a guideline for the continuum agglomerate UCs. Simulating agglomerates with a realistic primary particle size and number of primary

particles completely with coarse-grained MD is unfeasible, leaving the proposed multi-scale framework indispensable.

In general, coarse-graining methods are promising to increase the representativeness of the models, as the simulated length and time scales can typically be extended by up to two orders of magnitude. This can be helpful in many ways. For instance, as stated earlier, the gap concerning the experimental and numerical strain rates can be reduced. Coarse-graining can furthermore allow for the simulation of realistic primary particle sizes, e.g. for the determination of the interparticulate force-displacement curves to describe the particle interactions. This, in turn, will allow for the simulation of real primary particle sizes on the microscale, which will improve the comparability between the experiments and the simulations.

7.2.3 Extension of the Multi-Scale Framework

To ultimately deliver input for the simulation of real structures, the proposed multi-scale framework can be enhanced to capture fibers or voids on additional higher scales. Also, an extension to predict the nonlinear and viscoelastic response of NCs is possible. Furthermore, other effects, e.g. related to temperature, can be included, to be able to simulate the temperature-dependent elastic behavior or even calculate thermal properties, such as the thermal expansion coefficient. This could, for instance, allow for the simulation of the influence of NPs on the shrinkage behavior of NCs. The critical point in this view is the determination of the effective thermal properties of the particle-matrix interphase. The proposed method for the calculation of the local elastic properties does in its current version not support this feature since an exact choice of the interphase volume is not necessary for the elastic properties. As long as the interphase on the atomistic scale and its representation on the microscale are of the same thickness, the results are correct. However, the calculation of thermal properties, such as the thermal expansion coefficient, relies on the thorough determination of the interphase volume under different thermal conditions.

Bibliography

[1] C. Arlt. *Wirkungsweisen Nanoskaliger Böhmite in Einem Polymer Und Seinem Kohlenstofffaserverbund Unter Druckbelastung*. PhD thesis, Otto-von-Guericke-Universität Magdeburg, Fakultät für Maschinenbau, 2011.

[2] N. Shahid, R. G. Villate, and A. R. Barron. Chemically functionalized alumina nanoparticle effect on carbon fiber/epoxy composites. *Composites Science and Technology*, 65(14):2250–2258, November 2005. ISSN 0266-3538. doi: 10.1016/j.compscitech.2005.04.001.

[3] B. Arash, Q. Wang, and V. K. Varadan. Mechanical properties of carbon nanotube/polymer composites. *Scientific Reports*, 4:6479, October 2014. ISSN 2045-2322. doi: 10.1038/srep06479.

[4] J. Douce, J. Boilot, J. Biteau, L. Scodellaro, and A. Jimenez. Effect of filler size and surface condition of nano-sized silica particles in polysiloxane coatings. *Thin Solid Films*, 466(1):114–122, November 2004. ISSN 0040-6090. doi: 10.1016/j.tsf.2004.03.024.

[5] B. Arash, H. S. Park, and T. Rabczuk. Coarse-grained model of the J-integral of carbon nanotube reinforced polymer composites. *Carbon*, 96:1084–1092, January 2016. ISSN 0008-6223. doi: 10.1016/j.carbon.2015.10.058.

[6] S. Fu, X. Feng, B. Lauke, and Y. Mai. Effects of particle size, particle/matrix interface adhesion and particle loading on mechanical properties of particulate–polymer composites. *Composites Part B: Engineering*, 39(6):933–961, September 2008. ISSN 1359-8368. doi: 10.1016/j.compositesb.2008.01.002.

[7] P. H. C. Camargo, K. G. Satyanarayana, and F. Wypych. Nanocomposites: Synthesis, structure, properties and new application opportunities. *Materials Research*, 12(1):1–39, March 2009. ISSN 1516-1439. doi: 10.1590/S1516-14392009000100002.

[8] F. H. Gojny, M. H. G. Wichmann, B. Fiedler, and K. Schulte. Influence of different carbon nanotubes on the mechanical properties of epoxy matrix composites – A comparative study. *Composites Science and Technology*, 65(15):2300–2313, December 2005. ISSN 0266-3538. doi: 10.1016/j.compscitech.2005.04.021.

[9] Yuanxin Zhou, F. Pervin, L. Lewis, and S. Jeelani. Experimental study on the thermal and mechanical properties of multi-walled carbon nanotube-reinforced epoxy. *Materials Science and Engineering: A*, 452-453:657–664, April 2007. ISSN 0921-5093. doi: 10.1016/j.msea.2006.11.066.

[10] K. Majdzadeh-Ardakani, A. H. Navarchian, and F. Sadeghi. Optimization of mechanical properties of thermoplastic starch/clay nanocomposites. *Carbohydrate Polymers*, 79(3):547–554, February 2010. ISSN 0144-8617. doi: 10.1016/j.carbpol.2009.09.001.

[11] S. Singha and M. J. Thomas. Dielectric properties of epoxy nanocomposites. *IEEE Transactions on Dielectrics and Electrical Insulation*, 15(1):12–23, February 2008. ISSN 1070-9878. doi: 10.1109/T-DEI.2008.4446732.

[12] Y. Shen, Y. H. Lin, and C.-W. Nan. Interfacial Effect on Dielectric Properties of Polymer Nanocomposites Filled with Core/Shell-Structured Particles. *Advanced Functional Materials*, 17(14):2405–2410, 2007. ISSN 1616-3028. doi: 10.1002/adfm.200700200.

[13] T. Kashiwagi, E. Grulke, J. Hilding, K. Groth, R. Harris, Kathryn Butler, John Shields, Semen Kharchenko, and Jack Douglas. Thermal and flammability properties of polypropylene/carbon nanotube nanocomposites. *Polymer*, 45(12):4227–4239, May 2004. ISSN 0032-3861. doi: 10.1016/j.polymer.2004.03.088.

[14] J. Zhang, J. Lou, S. Ilias, P. Krishnamachari, and J. Yan. Thermal properties of poly(lactic acid) fumed silica nanocomposites: Experiments and molecular dynamics simulations. *Polymer*, 49(9):2381–2386, April 2008. ISSN 0032-3861. doi: 10.1016/j.polymer.2008.02.048.

[15] C. Zhao, H. Qin, F. Gong, M. Feng, S. Zhang, and M. Yang. Mechanical, thermal and flammability properties of polyethylene/clay nanocomposites. *Polymer Degradation and Stability*, 87(1):183–189, January 2005. ISSN 0141-3910. doi: 10.1016/j.polymdegradstab.2004.08.005.

[16] M. F. Uddin and C. T. Sun. Strength of unidirectional glass/epoxy composite with silica nanoparticle-enhanced matrix. *Composites Science and Technology*, 68(7):1637–1643, June 2008. ISSN 0266-3538. doi: 10.1016/j.compscitech.2008.02.026.

[17] A. K. Subramaniyan and C. T. Sun. Enhancing compressive strength of unidirectional polymeric composites using nanoclay. *Composites Part A: Applied Science and Manufacturing*, 37(12):2257–2268, December 2006. ISSN 1359-835X. doi: 10.1016/j.compositesa.2005.12.027.

[18] F. J. Galindo-Rosales, P. Moldenaers, and J. Vermant. Assessment of the Dispersion Quality in Polymer Nanocomposites by Rheological Methods. *Macromolecular Materials and Engineering*, 296(3-4):331–340, 2011. ISSN 1439-2054. doi: 10.1002/mame.201000345.

[19] E. E. Ureña-Benavides, M. J. Kayatin, and V. A. Davis. Dispersion and Rheology of Multiwalled Carbon Nanotubes in Unsaturated Polyester Resin. *Macromolecules*, 46(4):1642–1650, February 2013. ISSN 0024-9297. doi: 10.1021/ma3017844.

[20] F. Bensadoun, N. Kchit, C. Billotte, F. Trochu, and E. Ruiz. A Comparative Study of Dispersion Techniques for Nanocomposite Made with Nanoclays and an Unsaturated Polyester Resin. https://www.hindawi.com/journals/jnm/2011/406087/, 2011.

[21] M. F. Uddin and C. T. Sun. Improved dispersion and mechanical properties of hybrid nanocomposites. *Composites Science and Technology*, 70(2):223–230, February 2010. ISSN 0266-3538. doi: 10.1016/j.compscitech.2009.09.017.

[22] N. Sapiai, A. Jumahat, N. Manap, and M. A. I. Usoff. EFFECT OF NANOFILLERS DISPERSION ON MECHANICAL PROPERTIES OF CLAY/EPOXY AND SILICA/EPOXY NANOCOMPOSITES. *Jurnal Teknologi*, 76(9), September 2015. ISSN 2180-3722. doi: 10.11113/jt.v76.5687.

[23] R. D. West and V. M. Malhotra. Rupture of nanoparticle agglomerates and formulation of Al2O3-epoxy nanocomposites using ultrasonic cavitation approach: Effects on the structural and mechanical properties. *Polymer Engineering & Science*, 46(4):426–430, April 2006. ISSN 0032-3888, 1548-2634. doi: 10.1002/pen.20513.

[24] Y. Zare. Study of nanoparticles aggregation/agglomeration in polymer particulate nanocomposites by mechanical properties. *Composites Part A: Applied Science and Manufacturing*, 84:158–164, May 2016. ISSN 1359-835X. doi: 10.1016/j.compositesa.2016.01.020.

[25] H. Shin, S. Yang, J. Choi, S. Chang, and M. Cho. Effect of interphase percolation on mechanical behavior of nanoparticle-reinforced polymer nanocomposite with filler agglomeration: A multiscale approach. *Chemical Physics Letters*, 635:80–85, August 2015. ISSN 0009-2614. doi: 10.1016/j.cplett.2015.06.054.

[26] W. Gao, L. Ding, and Y. Zhu. Effect of Surface Modification on the Dispersion, Thermal Stability and Crystallization Properties of PET/CaCO3 Nanocomposites. *Tenside Surfactants Detergents*, 54(3):230–237, May 2017. ISSN 0932-3414. doi: 10.3139/113.110490.

[27] J. Böhm. Über Aluminium- und Eisenhydroxyde. I. *Zeitschrift für anorganische und allgemeine Chemie*, 149(1):203–216, 1925. ISSN 1521-3749. doi: 10.1002/zaac.19251490114.

[28] X. Bokhimi, J. A. Toledo-Antonio, M. L. Guzmán-Castillo, and F. Hernández-Beltrán. Relationship between Crystallite Size and Bond Lengths in Boehmite. *Journal of Solid State Chemistry*, 159(1):32–40, June 2001. ISSN 0022-4596. doi: 10.1006/jssc.2001.9124.

[29] A. B. Kiss, G. Keresztury, and L. Farkas. Raman and i.r. spectra and structure of boehmite (γ-AlOOH). Evidence for the recently discarded D172h space group. *Spectrochimica Acta Part A: Molecular Spectroscopy*, 36(7):653–658, January 1980. ISSN 0584-8539. doi: 10.1016/0584-8539(80)80024-9.

[30] D. Tunega, H. Pašalić, M. H. Gerzabek, and H. Lischka. Theoretical study of structural, mechanical and spectroscopic properties of boehmite ($\upgamma$-AlOOH). *Journal of Physics: Condensed Matter*, 23(40):404201, September 2011. ISSN 0953-8984. doi: 10.1088/0953-8984/23/40/404201.

[31] Y. Noel, R. Demichelis, F. Pascale, P. Ugliengo, R. Orlando, and R. Dovesi. Ab initio quantum mechanical study of γ-AlOOH boehmite: Structure and vibrational spectrum. *Physics and Chemistry of Minerals*, 36(1):47–59, January 2009. ISSN 1432-2021. doi: 10.1007/s00269-008-0257-z.

[32] J. Karger-Kocsis and L. Lendvai. Polymer/boehmite nanocomposites: A review. *Journal of Applied Polymer Science*, 135(24):45573, 2018. ISSN 1097-4628. doi: 10.1002/app.45573.

[33] J. Fankhänel, D. Silbernagl, M. Ghasem Zadeh Khorasani, B. Daum, A. Kempe, H. Sturm, and R. Rolfes. Mechanical Properties of Boehmite Evaluated by Atomic Force Microscopy Experiments and Molecular Dynamic Finite Element Simulations. *Journal of Nanomaterials*, 2016:1–13, 2016. doi: 10.1155/2016/5017213.

[34] R. C. Streller. *Boehmite Als Nanofüllstoffe Für Polypropylen-Nanocomposites Und Nanopartikel-Modifizierte Polypropylen/Kautschuk-Blends*. PhD thesis, Albert-Ludwigs-Universität Freiburg im Breisgau, Fakultät für Chemie, Pharmazie und Geowissenschaften, 2008.

[35] Nabaltec AG. Datasheet. APYRAL®, June 2018.

[36] Sasol Germany GmbH. Datasheet. Disperal HP14, March 2014.

[37] M. Kroupa, M. Klejch, M. Vonka, and J. Kosek. Discrete Element Modeling (DEM) of Agglomeration of Polymer Particles. *Procedia Engineering*, 42:58–69, January 2012. ISSN 1877-7058. doi: 10.1016/j.proeng.2012.07.395.

[38] H. C. Hamaker. The London—van der Waals attraction between spherical particles. *Physica*, 4(10):1058–1072, October 1937. ISSN 0031-8914. doi: 10.1016/S0031-8914(37)80203-7.

[39] C. Argento and R. H. French. Parametric tip model and force–distance relation for Hamaker constant determination from atomic force microscopy. *Journal of Applied Physics*, 80(11):6081–6090, December 1996. ISSN 0021-8979. doi: 10.1063/1.363680.

[40] K. Hongo and R. Maezono. A Computational Scheme To Evaluate Hamaker Constants of Molecules with Practical Size and Anisotropy. *Journal of Chemical Theory and Computation*, 13(11):5217–5230, November 2017. ISSN 1549-9618. doi: 10.1021/acs.jctc.6b01159.

[41] I. Yarovsky and E. Evans. Computer simulation of structure and properties of crosslinked polymers: Application to epoxy resins. *Polymer*, 43(3):963–969, February 2002. ISSN 0032-3861. doi: 10.1016/S0032-3861(01)00634-6.

[42] C. Wu and W. Xu. Atomistic molecular modelling of crosslinked epoxy resin. *Polymer*, 47(16):6004–6009, July 2006. ISSN 0032-3861. doi: 10.1016/j.polymer.2006.06.025.

[43] V. Varshney, S. S. Patnaik, A. K. Roy, and B. L. Farmer. A Molecular Dynamics Study of Epoxy-Based Networks: Cross-Linking Procedure and Prediction of Molecular and Material Properties. *Macromolecules*, 41(18):6837–6842, September 2008. ISSN 0024-9297. doi: 10.1021/ma801153e.

[44] P.-H. Lin and R. Khare. Molecular Simulation of Cross-Linked Epoxy and Epoxy-POSS Nanocomposite. *Macromolecules*, 42(12):4319–4327, June 2009. ISSN 0024-9297. doi: 10.1021/ma9004007.

[45] C. Li and A. Strachan. Molecular simulations of crosslinking process of thermosetting polymers. *Polymer*, 51(25):6058–6070, November 2010. ISSN 0032-3861. doi: 10.1016/j.polymer.2010.10.033.

[46] E. Hädicke and H. Stutz. Comparison of the structure of step-growth networks obtained by Monte Carlo simulation and branching theory. *Journal of Applied Polymer Science*, 85(5):929–935, 2002. ISSN 1097-4628. doi: 10.1002/app.10385.

[47] K.-C. Cheng and W.-Y. Chiu. Monte Carlo Simulation of Polymer Network Formation with Complex Chemical Reaction Mechanism: Kinetic Approach on Curing of Epoxides with Amines. *Macromolecules*, 27(12):3406–3414, June 1994. ISSN 0024-9297. doi: 10.1021/ma00090a040.

[48] D. Rigby and R.-J. Roe. Molecular dynamics simulation of polymer liquid and glass. I. Glass transition. *The Journal of Chemical Physics*, 87(12):7285–7292, December 1987. ISSN 0021-9606. doi: 10.1063/1.453321.

[49] K. F. Mansfield and D. N. Theodorou. Molecular dynamics simulation of a glassy polymer surface. *Macromolecules*, 24(23):6283–6294, November 1991. ISSN 0024-9297. doi: 10.1021/ma00023a034.

[50] C. Li and A. Strachan. Molecular scale simulations on thermoset polymers: A review. *Journal of Polymer Science Part B: Polymer Physics*, 53(2):103–122, 2015. ISSN 1099-0488. doi: 10.1002/polb.23489.

[51] D. N. Theodorou and U. W. Suter. Atomistic modeling of mechanical properties of polymeric glasses. *Macromolecules*, 19(1):139–154, January 1986. ISSN 0024-9297. doi: 10.1021/ma00155a022.

[52] M. Parrinello and A. Rahman. Crystal Structure and Pair Potentials: A Molecular-Dynamics Study. *Physical Review Letters*, 45(14):1196–1199, October 1980. doi: 10.1103/PhysRevLett.45.1196.

[53] D Brown and J. H. R. Clarke. Molecular dynamics simulation of an amorphous polymer under tension. 1. Phenomenology. *Macromolecules*, 24(8):2075–2082, April 1991. ISSN 0024-9297. doi: 10.1021/ma00008a056.

[54] C. Li and A. Strachan. Molecular dynamics predictions of thermal and mechanical properties of thermoset polymer EPON862/DETDA. *Polymer*, 52(13):2920–2928, June 2011. ISSN 00323861. doi: 10.1016/j.polymer.2011.04.041.

[55] N. B. Shenogina, M. Tsige, S. S. Patnaik, and S. Mukhopadhyay. Molecular modeling of elastic properties of thermosetting polymers using a dynamic deformation approach. *Polymer*, 54(13):3370–3376, June 2013. ISSN 0032-3861. doi: 10.1016/j.polymer.2013.04.034.

[56] S. V. Kallivokas, A. P. Sgouros, and D. N. Theodorou. Molecular dynamics simulations of EPON-862/DETDA epoxy networks: Structure, topology, elastic constants, and local dynamics. *Soft Matter*, 15(4):721–733, January 2019. ISSN 1744-6848. doi: 10.1039/C8SM02071J.

[57] S. Yang and J. Qu. Computing thermomechanical properties of crosslinked epoxy by molecular dynamic simulations. *Polymer*, 53(21):4806–4817, September 2012. ISSN 0032-3861. doi: 10.1016/j.polymer.2012.08.045.

[58] C. Li, G. A. Medvedev, E.-W. Lee, J. Kim, J. M. Caruthers, and A. Strachan. Molecular dynamics simulations and experimental studies of the thermomechanical response of an epoxy thermoset polymer. *Polymer*, 53(19):4222–4230, August 2012. ISSN 00323861. doi: 10.1016/j.polymer.2012.07.026.

[59] G. M. Odegard, T. C. Clancy, and T. S. Gates. Modeling of the mechanical properties of nanoparticle/polymer composites. *Polymer*, 46(2):553–562, January 2005. ISSN 0032-3861. doi: 10.1016/j.polymer.2004.11.022.

[60] Z. Hashin and S. Shtrikman. A variational approach to the theory of the elastic behaviour of multiphase materials. *Journal of the Mechanics and Physics of Solids*, 11(2):127–140, March 1963. ISSN 0022-5096. doi: 10.1016/0022-5096(63)90060-7.

[61] T Mori and K Tanaka. Average stress in matrix and average elastic energy of materials with misfitting inclusions. *Acta Metallurgica*, 21(5):571–574, May 1973. ISSN 0001-6160. doi: 10.1016/0001-6160(73)90064-3.

[62] Y. Benveniste. A new approach to the application of Mori-Tanaka's theory in composite materials. *Mechanics of Materials*, 6(2):147–157, June 1987. ISSN 0167-6636. doi: 10.1016/0167-6636(87)90005-6.

[63] Y. Zare and H. Garmabi. Thickness, modulus and strength of interphase in clay/polymer nanocomposites. *Applied Clay Science*, 105-106:66–70, March 2015. ISSN 0169-1317. doi: 10.1016/j.clay.2014.12.016.

[64] Y. Zare and K. Y. Rhee. Multistep modeling of Young's modulus in polymer/clay nanocomposites assuming the intercalation/exfoliation of clay layers and the interphase between polymer matrix and nanoparticles. *Composites Part A: Applied Science and Manufacturing*, 102:137–144, November 2017. ISSN 1359-835X. doi: 10.1016/j.compositesa.2017.08.004.

[65] N. Nikfar, Y. Zare, and K. Y. Rhee. Dependence of mechanical performances of polymer/carbon nanotubes nanocomposites on percolation threshold. *Physica B: Condensed Matter*, 533:69–75, March 2018. ISSN 0921-4526. doi: 10.1016/j.physb.2018.01.008.

[66] Y. Zare, M. Fasihi, and K. Y. Rhee. Efficiency of stress transfer between polymer matrix and nanoplatelets in clay/polymer nanocomposites. *Applied Clay Science*, 143:265–272, July 2017. ISSN 0169-1317. doi: 10.1016/j.clay.2017.03.043.

[67] F. Bondioli, V. Cannillo, E. Fabbri, and M. Messori. Epoxy-silica nanocomposites: Preparation, experimental characterization, and modeling. *Journal of Applied Polymer Science*, 97(6):2382–2386, 2005. ISSN 1097-4628. doi: 10.1002/app.21854.

[68] R. Qiao and L. C. Brinson. Simulation of interphase percolation and gradients in polymer nanocomposites. *Composites Science and Technology*, 69(3):491–499, March 2009. ISSN 0266-3538. doi: 10.1016/j.compscitech.2008.11.022.

[69] J. Seiler and J. Kindersberger. Insight into the interphase in polymer nanocomposites. *IEEE Transactions on Dielectrics and Electrical Insulation*, 21(2): 537–547, April 2014. ISSN 1070-9878. doi: 10.1109/TDEI.2013.004388.

[70] D. Platz, D. Forchheimer, E. A. Tholén, and D. B. Haviland. Interaction imaging with amplitude-dependence force spectroscopy. *Nature Communications*, 4:1360, January 2013. ISSN 2041-1723. doi: 10.1038/ncomms2365.

[71] M. Cho, S. Yang, S. Chang, and S. Yu. A study on the prediction of the mechanical properties of nanoparticulate composites using the homogenization method with the effective interface concept. *International Journal for Numerical Methods in Engineering*, 85(12):1564–1583, 2011. ISSN 1097-0207. doi: 10.1002/nme.3039.

[72] Y. Zare and K. Y. Rhee. Accounting the reinforcing efficiency and percolating role of interphase regions in tensile modulus of polymer/CNT nanocomposites. *European Polymer Journal*, 87:389–397, February 2017. ISSN 0014-3057. doi: 10.1016/j.eurpolymj.2017.01.007.

[73] M. Malagù, M. Goudarzi, A. Lyulin, E. Benvenuti, and A. Simone. Diameter-dependent elastic properties of carbon nanotube-polymer composites: Emergence of size effects from atomistic-scale simulations. *Composites Part B: Engineering*, 131:260–281, December 2017. ISSN 1359-8368. doi: 10.1016/j.compositesb.2017.07.029.

[74] K. Farah, F. Leroy, F. Müller-Plathe, and M. C. Böhm. Interphase Formation during Curing: Reactive Coarse Grained Molecular Dynamics Simulations. *The Journal of Physical Chemistry C*, 115(33):16451–16460, August 2011. ISSN 1932-7447. doi: 10.1021/jp203480q.

[75] A. K. Subramaniyan and C. T. Sun. Continuum interpretation of virial stress in molecular simulations. *International Journal of Solids and Structures*, 45(14):4340–4346, July 2008. ISSN 0020-7683. doi: 10.1016/j.ijsolstr.2008.03.016.

[76] M. L. Falk and J. S. Langer. Dynamics of Viscoplastic Deformation in Amorphous Solids. *Physical Review E*, 57(6):7192–7205, June 1998. ISSN 1063-651X, 1095-3787. doi: 10.1103/PhysRevE.57.7192.

[77] C. M. Hadden, D. R. Klimek-McDonald, E. J. Pineda, J. A. King, A. M. Reichanadter, I. Miskioglu, S. Gowtham, and G. M. Odegard. Mechanical properties of graphene nanoplatelet/carbon fiber/epoxy hybrid composites: Multiscale modeling and experiments. *Carbon*, 95:100–112, December 2015. ISSN 0008-6223. doi: 10.1016/j.carbon.2015.08.026.

[78] O. Aluko, S. Gowtham, and G. M. Odegard. Multiscale modeling and analysis of graphene nanoplatelet/carbon fiber/epoxy hybrid composite. *Composites Part B: Engineering*, 131:82–90, December 2017. ISSN 1359-8368. doi: 10.1016/j.compositesb.2017.07.075.

[79] Y. Li, S. Wang, B. Arash, and Q. Wang. A study on tribology of nitrile-butadiene rubber composites by incorporation of carbon nanotubes: Molecular dynamics simulations. *Carbon*, 100:145–150, April 2016. ISSN 0008-6223. doi: 10.1016/j.carbon.2015.12.104.

[80] J. Liu, Y. Gao, D. Cao, L. Zhang, and Z. Guo. Nanoparticle Dispersion and Aggregation in Polymer Nanocomposites: Insights from Molecular Dynamics Simulation. *Langmuir*, 27(12):7926–7933, June 2011. ISSN 0743-7463. doi: 10.1021/la201073m.

[81] X. Deng, Z. Huang, W. Wang, and R. N. Davé. Investigation of nanoparticle agglomerates properties using Monte Carlo simulations. *Advanced Powder Technology*, 27(5):1971–1979, September 2016. ISSN 0921-8831. doi: 10.1016/j.apt.2016.06.029.

[82] S. Díez Orrite, S. Stoll, and P. Schurtenberger. Off-lattice Monte Carlo simulations of irreversible and reversible aggregation processes. *Soft Matter*, 1(5): 364–371, October 2005. ISSN 1744-6848. doi: 10.1039/B510449A.

[83] D.-L. Shi, X.-Q. Feng, Y. Y. Huang, K.-C. Hwang, and H. Gao. The Effect of Nanotube Waviness and Agglomeration on the Elastic Property of Carbon Nanotube-Reinforced Composites. *Journal of Engineering Materials and Technology*, 126(3):250–257, June 2004. ISSN 0094-4289. doi: 10.1115/1.1751182.

[84] M. Shokrieh and R. Rafiee. Stochastic multi-scale modeling of CNT/polymer composites. *Computational Materials Science*, 50(2):437–446, December 2010. ISSN 0927-0256. doi: 10.1016/j.commatsci.2010.08.036.

[85] X. Ma, Y. Zare, and K. Y. Rhee. A Two-Step Methodology to Study the Influence of Aggregation/Agglomeration of Nanoparticles on Young's Modulus of Polymer Nanocomposites. *Nanoscale Research Letters*, 12, December 2017. ISSN 1931-7573. doi: 10.1186/s11671-017-2386-0.

[86] M. A. Ashraf, W. Peng, Y. Zare, and K. Y. Rhee. Effects of Size and Aggregation/Agglomeration of Nanoparticles on the Interfacial/Interphase Properties and Tensile Strength of Polymer Nanocomposites. *Nanoscale Research Letters*, 13, July 2018. ISSN 1931-7573. doi: 10.1186/s11671-018-2624-0.

[87] A. Pontefisso, M. Zappalorto, and M. Quaresimin. An efficient RVE formulation for the analysis of the elastic properties of spherical nanoparticle

reinforced polymers. *Computational Materials Science*, 96:319–326, January 2015. ISSN 0927-0256. doi: 10.1016/j.commatsci.2014.09.030.

[88] Frédéric Feyel and Jean-Louis Chaboche. FE2 multiscale approach for modelling the elastoviscoplastic behaviour of long fibre SiC/Ti composite materials. *Computer Methods in Applied Mechanics and Engineering*, 183(3):309–330, March 2000. ISSN 0045-7825. doi: 10.1016/S0045-7825(99)00224-8.

[89] Frédéric Feyel. A multilevel finite element method (FE2) to describe the response of highly non-linear structures using generalized continua. *Computer Methods in Applied Mechanics and Engineering*, 192(28):3233–3244, July 2003. ISSN 0045-7825. doi: 10.1016/S0045-7825(03)00348-7.

[90] Mohammad Silani, Saeed Ziaei-Rad, Hossein Talebi, and Timon Rabczuk. A semi-concurrent multiscale approach for modeling damage in nanocomposites. *Theoretical and Applied Fracture Mechanics*, 74:30–38, December 2014. ISSN 0167-8442. doi: 10.1016/j.tafmec.2014.06.009.

[91] Ted Belytschko and Jeong-Hoon Song. Coarse-graining of multiscale crack propagation. *International Journal for Numerical Methods in Engineering*, 81 (5):537–563, 2010. ISSN 1097-0207. doi: 10.1002/nme.2694.

[92] L. Nasdala, A. Kempe, and R. Rolfes. The molecular dynamic finite element method (MDFEM). *Computers Materials and Continua*, 19(1), 2010.

[93] Lutz Nasdala, Andreas Kempe, and Raimund Rolfes. Are finite elements appropriate for use in molecular dynamic simulations? *Composites Science and Technology*, 72(9):989–1000, May 2012. ISSN 0266-3538. doi: 10.1016/j.compscitech.2012.03.008.

[94] Lutz Nasdala and Gerald Ernst. Development of a 4-node finite element for the computation of nano-structured materials. *Computational Materials Science*, 33(4):443–458, June 2005. ISSN 0927-0256. doi: 10.1016/j.commatsci.2004.09.047.

[95] M. Jux, J. Fankhänel, B. Daum, T. Mahrholz, M. Sinapius, and R. Rolfes. Mechanical properties of epoxy/boehmite nanocomposites in dependency of mass fraction and surface modification - An experimental and numerical approach. *Polymer*, 141:34–45, April 2018. ISSN 0032-3861. doi: 10.1016/j.polymer.2018.02.059.

[96] M. Zhou. A new look at the atomic level virial stress: On continuum-molecular system equivalence. *Proceedings of the Royal Society of London. Series A: Mathematical, Physical and Engineering Sciences*, 459(2037):2347–2392, September 2003. doi: 10.1098/rspa.2003.1127.

[97] B. Liu and X. Qiu. How to Compute the Atomic Stress Objectively? https://www.ingentaconnect.com/content/asp/jctn/2009/00000006/00000005/art00019%3bjsessionid=94pt27kdkgmqc.x-ic-live-01, May 2009.

[98] R. Clausius. XVI. On a mechanical theorem applicable to heat. *The London, Edinburgh, and Dublin Philosophical Magazine and Journal of Science*, 40(265):122–127, August 1870. ISSN 1941-5982. doi: 10.1080/14786447008640370.

[99] J. Fankhänel, B. Arash, and R. Rolfes. Elastic interphase properties of nanoparticle/epoxy nanocomposites: A molecular dynamics study. *Composites Part B: Engineering*, 176:107211, November 2019. ISSN 1359-8368. doi: 10.1016/j.compositesb.2019.107211.

[100] R. Hill. Elastic properties of reinforced solids: Some theoretical principles. *Journal of the Mechanics and Physics of Solids*, 11(5):357–372, September 1963. ISSN 0022-5096. doi: 10.1016/0022-5096(63)90036-X.

[101] W. Voigt. Ueber die Beziehung zwischen den beiden Elasticitätsconstanten isotroper Körper. *Annalen der Physik*, 274(12):573–587, 1889. ISSN 1521-3889. doi: 10.1002/andp.18892741206.

[102] A. Reuss. Berechnung der Fließgrenze von Mischkristallen auf Grund der Plastizitätsbedingung für Einkristalle . *ZAMM - Journal of Applied Mathematics and Mechanics / Zeitschrift für Angewandte Mathematik und Mechanik*, 9(1): 49–58, 1929. ISSN 1521-4001. doi: 10.1002/zamm.19290090104.

[103] S. Plimpton. Fast Parallel Algorithms for Short-Range Molecular Dynamics. *Journal of Computational Physics*, 117(1):1–19, March 1995. ISSN 0021-9991. doi: 10.1006/jcph.1995.1039.

[104] J. B. Wachtman, W. E. Tefft, D. G. Lam, and C. S. Apstein. Exponential Temperature Dependence of Young's Modulus for Several Oxides. *Physical Review*, 122(6):1754–1759, June 1961. doi: 10.1103/PhysRev.122.1754.

[105] R. M. Spriggs, J. B. Mitchell, and T. Vasilos. Mechanical Properties of Pure, Dense Aluminum Oxide as a Function of Temperature and Grain Size. *Journal of the American Ceramic Society*, 47(7):323–327, 1964. ISSN 1551-2916. doi: 10.1111/j.1151-2916.1964.tb12994.x.

[106] Huntsman Corporation. Datasheet. Araldite® LY 556 / Aradur® 917 / Accelerator DY 070, February 1998.

[107] N. M. O'Boyle, M. Banck, C. A. James, C. Morley, T. Vandermeersch, and G. R. Hutchison. Open Babel: An open chemical toolbox. *Journal of Cheminformatics*, 3(1):33, October 2011. ISSN 1758-2946. doi: 10.1186/1758-2946-3-33.

[108] L. Martínez, R. Andrade, E. G. Birgin, and J. M. Martínez. PACKMOL: A package for building initial configurations for molecular dynamics simulations. *Journal of Computational Chemistry*, 30(13):2157–2164, October 2009. ISSN 1096-987X. doi: 10.1002/jcc.21224.

[109] B. Finke. Institute for Particle Technology. TU Braunschweig (private communication).

[110] I. J. Bruno, J. C. Cole, P. R. Edgington, M. Kessler, C. F. Macrae, P. McCabe, J. Pearson, and R. Taylor. New software for searching the Cambridge Structural Database and visualizing crystal structures. *Acta Crystallographica Section B: Structural Science*, 58(3):389–397, June 2002. ISSN 0108-7681. doi: 10.1107/S0108768102003324.

[111] O. Torno. Dispergierbare Böhmite aus Alkoxidprozess, 2008.

[112] S. L. Mayo, B. D. Olafson, and W. A. Goddard. DREIDING: A generic force field for molecular simulations. *The Journal of Physical Chemistry*, 94(26): 8897–8909, December 1990. ISSN 0022-3654. doi: 10.1021/j100389a010.

[113] S. Melchionna, G. Ciccotti, and B. L. Holian. Hoover NPT dynamics for systems varying in shape and size. *Molecular Physics*, 78(3):533–544, February 1993. ISSN 0026-8976. doi: 10.1080/00268979300100371.

[114] T. Schneider and E. Stoll. Molecular-dynamics study of a three-dimensional one-component model for distortive phase transitions. *Physical Review B*, 17 (3):1302–1322, February 1978. doi: 10.1103/PhysRevB.17.1302.

[115] T. Okabe, Y. Oya, K. Tanabe, G. Kikugawa, and K. Yoshioka. Molecular dynamics simulation of crosslinked epoxy resins: Curing and mechanical properties. *European Polymer Journal*, 80:78–88, July 2016. ISSN 0014-3057. doi: 10.1016/j.eurpolymj.2016.04.019.

[116] A. Bandyopadhyay, P. K. Valavala, T. C. Clancy, K. E. Wise, and G. M. Odegard. Molecular modeling of crosslinked epoxy polymers: The effect of crosslink density on thermomechanical properties. *Polymer*, 52(11):2445–2452, May 2011. ISSN 00323861. doi: 10.1016/j.polymer.2011.03.052.

[117] T. C. Clancy, S. J. V. Frankland, J. A. Hinkley, and T. S. Gates. Molecular modeling for calculation of mechanical properties of epoxies with moisture ingress. *Polymer*, 50(12):2736–2742, June 2009. ISSN 0032-3861. doi: 10.1016/j.polymer.2009.04.021.

[118] G. M. Odegard, B. D. Jensen, S. Gowtham, J. Wu, J. He, and Z. Zhang. Predicting mechanical response of crosslinked epoxy using ReaxFF. *Chemical Physics Letters*, 591:175–178, January 2014. ISSN 0009-2614. doi: 10.1016/j.cplett.2013.11.036.

[119] M. S. Radue, B. D. Jensen, S. Gowtham, D. Klimek-McDonald, J. A. King, and G. M. Odegard. Comparing the mechanical response of di-, tri-, and tetrafunctional resin epoxies with reactive molecular dynamics. *Journal of Polymer Science Part B: Polymer Physics*, 56(3):255–264, 2018. ISSN 1099-0488. doi: 10.1002/polb.24539.

[120] J. D. Littell, C. R. Ruggeri, R. K. Goldberg, G. D. Roberts, W. A. Arnold, and W. A. Binienda. Measurement of Epoxy Resin Tension, Compression, and Shear Stress–Strain Curves over a Wide Range of Strain Rates Using Small Test Specimens. *Journal of Aerospace Engineering*, 21(3):162–173, July 2008. doi: 10.1061/(ASCE)0893-1321(2008)21:3(162).

[121] N. K. Naik, P. J. Shankar, V. R. Kavala, G. Ravikumar, J. R. Pothnis, and H. Arya. High strain rate mechanical behavior of epoxy under compressive loading: Experimental and modeling studies. *Materials Science and Engineering: A*, 528(3):846–854, January 2011. ISSN 0921-5093. doi: 10.1016/j.msea.2010.10.099.

[122] A. Gilat, R. K. Goldberg, and G. D. Roberts. Strain Rate Sensitivity of Epoxy Resin in Tensile and Shear Loading. *Journal of Aerospace Engineering*, 20(2): 75–89, April 2007. ISSN 0893-1321, 1943-5525. doi: 10.1061/(ASCE)0893-1321(2007)20:2(75).

[123] M. Y. Fard, Y. Liu, and A. Chattopadhyay. Characterization of Epoxy Resin Including Strain Rate Effects Using Digital Image Correlation System. *Journal of Aerospace Engineering*, 25(2):308–319, April 2012. doi: 10.1061/(ASCE)AS.1943-5525.0000127.

[124] H. Sturm. Bundesanstalt für Materialfroschung und -prüfung (private communication).

[125] R. Unger, U. Braun, J. Fankhänel, B. Daum, B. Arash, and R. Rolfes. Molecular modelling of epoxy resin crosslinking experimentally validated by near-infrared spectroscopy. *Computational Materials Science*, 161:223–235, April 2019. ISSN 0927-0256. doi: 10.1016/j.commatsci.2019.01.054.

[126] C. M. Stafford, B. D. Vogt, C. Harrison, D. Julthongpiput, and R. Huang. Elastic Moduli of Ultrathin Amorphous Polymer Films. *Macromolecules*, 39 (15):5095–5099, July 2006. ISSN 0024-9297. doi: 10.1021/ma060790i.

[127] J. M. Torres, C. M. Stafford, and B. D. Vogt. Elastic Modulus of Amorphous Polymer Thin Films: Relationship to the Glass Transition Temperature. *ACS Nano*, 3(9):2677–2685, September 2009. ISSN 1936-0851. doi: 10.1021/nn9006847.

[128] D. Ciprari, K. Jacob, and R. Tannenbaum. Characterization of Polymer Nanocomposite Interphase and Its Impact on Mechanical Properties. *Macromolecules*, 39(19):6565–6573, September 2006. ISSN 0024-9297. doi: 10.1021/ma0602270.

[129] M. Ghasem Zadeh Khorasani, D. Silbernagl, D. Platz, and H. Sturm. Insights into Nano-Scale Physical and Mechanical Properties of Epoxy/Boehmite Nanocomposite Using Different AFM Modes. *Polymers*, 11(2), February 2019. ISSN 2073-4360. doi: 10.3390/polym11020235.

[130] D. Silbernagl. Bundesanstalt für Materialfroschung und -prüfung (private communication).

[131] M. Jux, B. Finke, T. Mahrholz, M. Sinapius, A. Kwade, and C. Schilde. Effects of Al(OH)O nanoparticle agglomerate size in epoxy resin on tension, bending, and fracture properties. *Journal of Nanoparticle Research*, 19(4):139, April 2017. ISSN 1572-896X. doi: 10.1007/s11051-017-3831-9.

[132] C. Geuzaine and J.-F. Remacle. Gmsh: A 3-D finite element mesh generator with built-in pre- and post-processing facilities. *International Journal for Numerical Methods in Engineering*, 79(11):1309–1331, 2009. ISSN 1097-0207. doi: 10.1002/nme.2579.

[133] Ashkan Almasi, Mohammad Silani, Hossein Talebi, and Timon Rabczuk. Stochastic analysis of the interphase effects on the mechanical properties of clay/epoxy nanocomposites. *Composite Structures*, 133:1302–1312, December 2015. ISSN 0263-8223. doi: 10.1016/j.compstruct.2015.07.061.

[134] A. Wongsto and S. Li. Micromechanical FE analysis of UD fibre-reinforced composites with fibres distributed at random over the transverse cross-section. *Composites Part A: Applied Science and Manufacturing*, 36(9):1246–1266, September 2005. ISSN 1359-835X. doi: 10.1016/j.compositesa.2005.01.010.

[135] A. R. Melro, P. P. Camanho, and S. T. Pinho. Generation of random distribution of fibres in long-fibre reinforced composites. *Composites Science and Technology*, 68(9):2092–2102, July 2008. ISSN 0266-3538. doi: 10.1016/j.compscitech.2008.03.013.

[136] A. K. Soper. Empirical potential Monte Carlo simulation of fluid structure. *Chemical Physics*, 202(2):295–306, January 1996. ISSN 0301-0104. doi: 10.1016/0301-0104(95)00357-6.

[137] W. Tschöp, K. Kremer, J. Batoulis, T. Bürger, and O. Hahn. Simulation of polymer melts. I. Coarse-graining procedure for polycarbonates. *Acta Polymerica*, 49(2-3):61–74, 1998. ISSN 1521-4044. doi: 10.1002/(SICI)1521-4044(199802)49:2/3<61::AID-APOL61>3.0.CO;2-V.

[138] A. Prasad, T. Grover, and S. Basu. Coarse – grained molecular dynamics simulation of cross – linking of DGEBA epoxy resin and estimation of the adhesive strength. *International Journal of Engineering, Science and Technology*, 2(4): 17–30–30, January 2010. ISSN 2141-2839.